

Adaptive and model-based control in laminar boundary-layer flows

by

Nicolò Fabbiane

October 2014
Technical Reports
Royal Institute of Technology
Department of Mechanics
SE-100 44 Stockholm, Sweden

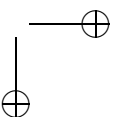
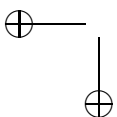
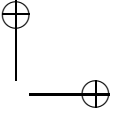
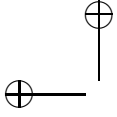
Akademisk avhandling som med tillstånd av Kungliga Tekniska Högskolan i Stockholm framlägges till offentlig granskning för avläggande av teknologie licentiatexamen torsdagen den 27 Oktober 2014 kl 10.30 i sal D3, Kungliga Tekniska Högskolan, Lindstedtsvägen 5, Stockholm.

©Nicolò Fabbiane 2014

Universitetsservice US-AB, Stockholm 2014

“Reality is frequently inaccurate.”

Douglas Adams, *The Restaurant at the End of the Universe*



Adaptive and model-based control in laminar boundary-layer flows

Nicolò Fabbiane

Linné FLOW Centre, KTH Mechanics, Royal Institute of Technology
SE-100 44 Stockholm, Sweden

Abstract

In boundary-layer flows it is possible to reduce the friction drag by breaking the path from laminar to turbulent state. In low turbulence environments, the laminar-to-turbulent transition is dominated by local flow instabilities – Tollmien-Schlichting (TS) waves – that exponentially grows while being convected by the flow and, eventually, lead to transition. Hence, by attenuating these disturbances via localised forcing in the flow it is possible to delay farther downstream the onset of turbulence and reduce the friction drag.

Reactive control techniques are widely investigated to this end. The aim of this work is to compare model-based and adaptive control techniques and show how the adaptivity is crucial to control TS-waves in real applications. The control design consists in (i) choosing sensors and actuators and (ii) designing the system responsible to process on-line the measurement signals in order to compute an appropriate forcing by the actuators. This system, called compensator, can be static or adaptive, depending on the possibility of self-adjusting its response to unmodelled flow dynamics. A Linear Quadratic Gaussian (LQG) regulator is chosen as representative of static controllers. Direct numerical simulations of the flow are performed to provide a model for the compensator design and test its performance. An adaptive Filtered-X Least-Mean-Squares (FXLMS) compensator is also designed for the same flow case and its performance is compared to the model-based compensator via simulations and experiments. Although the LQG regulator behaves better at design conditions, it lacks robustness to small flow variations. On the other hand, the FXLMS compensator proved to be able to adapt its response to overcome the varied conditions and perform an adequate control action.

It is thus found that an adaptive control technique is more suitable to delay the laminar-to-turbulent transition in situations where an accurate model of the flow is not available.

Descriptors: flow control, adaptive control, model-based control, optimal control, flat-plate boundary layer, laminar-to-turbulent transition, plasma actuator.

Adaptiv och modellbaserad styrning i laminära gränsskiktsflöden

Nicolò Fabbiane

Linné FLOW Centre, KTH Mekanik, Kungliga Tekniska Högskolan
SE-100 44 Stockholm, Sverige

Sammanfattning

I det tunna gränsskikt som uppstår på en yta, kan friktionen minskas genom att förhindra omslag från ett laminärt till ett turbulent flöde. När turbulensnivån är låg i omgivningen, domineras till en början omslaget av lokala instabiliteter (Tollmien-Schlichting (TS) vågor) som växer i en exponentiell takt samtidigt som de propagerar nedströms. Därför, kan man förskjuta omslaget genom att dämpa TS vågors tillväxt i ett gränsskikt och därmed minska friktionen.

Med detta mål i sikte, tillämpas och jämförs två reglertekniska metoder, nämligen en adaptiv signalbaserad metod och en statistiskt modellbaserad metod. Vi visar att adaptivitet är av avgörande betydelse för att kunna dämpa TS vågor i en verklig miljö. Den reglertekniska konstruktionen består av val av givare och aktuatorer samt att bestämma det system som behandlar mätsignaler (online) för beräkning av en lämplig signal till aktuatorer. Detta system, som kallas för en kompensator, kan vara antingen statisk eller adaptiv, beroende på om det har möjlighet till att anpassa sig till omgivningen. En så kallad linjär regulator (LQG), som representerar den statiska kompensator, har tagits fram med hjälp av numeriska simuleringar of strömningsfältet. Denna kompensator jämförs med en adaptiv regulator som kallas för Filtered-X Least-Mean-Squares (FXLMS) både experimentellt och numeriskt. Det visar sig att LQG regulatorn har en bättre prestanda än FXLMS för de parametrar som den var framtagen för, men brister i robusthet. FXLMS å andra sidan, anpassar sig till icke-modellerade störningar och variationer, och kan därmed hålla en god och jämn prestanda.

Man kan därmed dra slutsatsen att adaptiva regulatorer är mer lämpliga för att förhålla omslaget från laminär till turbulent strömning i situationer då en exakt modell av fysiken saknas.

Descriptors: flödeskontroll, adaptiv styrning, modellbaserad styrning, optimal kontroll, platt-plattgränsskikt, laminärt till turbulent övergång, plasma ställdon.

Preface

This thesis deals with adaptive and model-based control techniques aimed to delay the TS-wave driven laminar-to-turbulent transition in boundary-layer flows. A brief introduction on the basic concepts and methods is presented in the first part. The second part contains three articles. The papers are adjusted to comply with the present thesis format for consistency, but their contents have not been altered as compared with their original counterparts.

Paper 1. N. FABBIANE, O. SEMERARO, S. BAGHERI & D. S. HENNINGSON, 2014. *Adaptive and Model-Based Control Theory Applied to Convectively Unstable Flows*. Appl. Mech. Rev. **66** (6): 060801

Paper 2. N. FABBIANE, B. SIMON, F. FISCHER, S. GRUNDMANN, S. BAGHERI & D. S. HENNINGSON, 2014. *On the role of adaptivity for robust laminar flow control*. To be submitted to J. Fluid Mech.

Paper 3. R. DADFAR, N. FABBIANE, S. BAGHERI & D. S. HENNINGSON, 2014. *Centralised versus Decentralised Active Control of Boundary Layer Instabilities*. Flow Turb. Comb. Published on-line.

October 2014, Stockholm

Nicolò Fabbiane

Division of work between authors

The main advisor for the project is Prof. Dan S. Henningson (DH). Dr. Shervin Bagheri (SB) acts as co-advisor.

Paper 1

The code has been developed by Nicolò Fabbiane (NF). The paper has been written by NF and Onofrio Semeraro with feedback from SB and DH.

Paper 2

The experimental set-up has been designed by Bernhard Simon (BS). The model-based control has been implemented by NF, while the adaptive control by Felix Fischer. The simulations have been performed by NF using the control-code developed by NF. The paper has been written by NF and BS with feedback from Sven Grundmann, SB and DH.

Paper 3

The simulations have been performed by Reza Dadfar (RD) using the control-code developed by NF. The paper has been written by RD with feedback from NF, SB and DH.

Contents

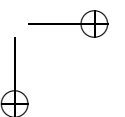
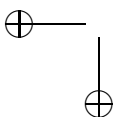
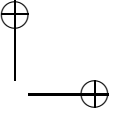
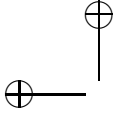
Abstract	v
Sammanfattning	vi
Preface	vii
Part I - Overview and summary	
Chapter 1. Introduction	3
1.1. The control problem	3
Chapter 2. The plant	5
2.1. A linear model of the flow	5
Chapter 3. The compensator	9
3.1. Model-based control	9
3.2. Adaptive control	11
Chapter 4. The closed-loop system	12
4.1. The importance of being adaptive	14
Chapter 5. The third dimension	15
5.1. A “three-dimensional” compensator	15
5.2. Preliminary results	17
Chapter 6. Summary of the papers	21
Chapter 7. Conclusions and outlook	23
Acknowledgements	24
Bibliography	25

Part II - Papers

Paper 1.	Adaptive and Model-Based Control Theory Applied to Convectively Unstable Flows	31
Paper 2.	On the Role of Adaptivity for Robust Laminar Flow Control	87
Paper 3.	Centralised versus Decentralised Active Control of Boundary Layer Instabilities	103

Part I

Overview and summary



CHAPTER 1

Introduction

The laminar boundary layer is characterised by lower friction than the turbulent one. Hence, extending the laminar regime in a boundary-layer flow leads to a friction drag reduction. This possibility is particularly attractive for the transport industry: as most vehicles move through a fluid, a friction-drag reduction would permit a more energy-efficient design and lead to greener/cheaper mobility.

In a low-turbulence environment, local instabilities of the boundary-layer flow – Tollmien-Schlichting (TS) waves – have a lead role in the transition scenario. These disturbances grow exponentially in the boundary-layer while convected downstream by the flow (Schmid & Henningson 2001). Once a critical amplitude is reached, non-linear phenomena are triggered that lead to the transition to turbulence (Saric *et al.* 2002). Hence the transition can be delayed by attenuating the growth of TS-waves. The three major strategies to achieve this goal are: (i) enhancing the stability of the flow via passive (Shahinfar *et al.* 2014) or active (Duchmann *et al.* 2013) manipulations of the mean-flow, (ii) applying an aimed forcing of the flow in order to directly cancel the disturbance (Bewley & Liu 1998; Lundell 2007; Goldin *et al.* 2013; Semeraro *et al.* 2013) or (iii) a combination of them (Kurz *et al.* 2013).

1.1. The control problem

In this work the cancellation technique is pursued: sensors are placed in the flow and used to detect the upcoming disturbances in order to design the cancellation forcing in the flow. The choice and positioning of these devices is the zero-step in the control design process, as it decides how the control algorithm will interact with the system and deeply influence the design of the control itself (Belson *et al.* 2013). In this work a reference sensor (y) is positioned upstream the actuator u , in order to detect the upcoming disturbance, generated by a disturbance source d . This information is then given to the compensator in order to prescribe a proper forcing to the actuator u . Hence, the interaction between the disturbance and the wave generated by the actuator lead to a attenuation of the disturbance amplitude, detected by the error sensor z .

The compensator is the core of the control action, as it is the system responsible to compute the control action based on the measurement signals. Two antithetical compensator-design strategies emerged in literature. The first consists in precomputing the compensator response based on an accurate model

4 1. INTRODUCTION

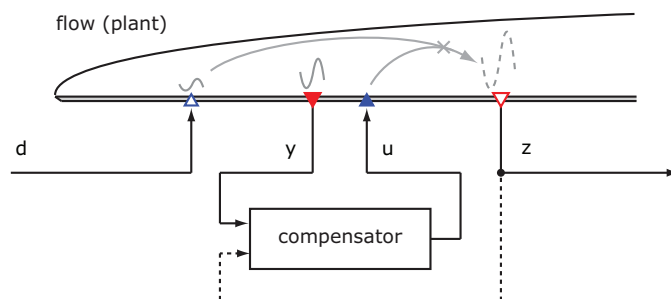


FIGURE 1.1. Control scheme. A 2D zero-pressure-gradient boundary layer flow is considered. The disturbance source d is responsible to generate a train of TS-wave that is downstream damped by the actuator u . The actuator action is based on on-line measurements by the reference sensor y and, possibly, the error sensor z .

of the flow: this procedure permits to use the traditional optimal control theory with all its known stability and robustness results (Bagheri & Henningson 2011). Moreover, the affinity with the canonical stability theory enabled these techniques to rapidly spread in the numerical community (e.g. Bewley & Liu 1998; Barbagallo *et al.* 2009; Bagheri & Henningson 2011; Semeraro *et al.* 2013) until reaching the experimental level with Juillet *et al.* (2014). The second strategy is based on an on-line identification of the compensator response (Sturzebecher & Nitsche 2003): the measurement error sensor z is used to evaluate on-line the magnitude of the TS-wave after the control action and to adjust the compensator response in order to reduce this amplitude measurement.

The aim of this work is to assess if the optimal performances guaranteed by the model-based approach can hold against the on-line tailored response of the adaptive techniques when it comes to real applications. In particular, we focus on the robustness of the compensator to model inaccuracies that can typically occur where the control problem is addressed in real flows.

This thesis is organised as follows. In §2 the equations that govern the time-evolution of the flow – also called *plant* – are introduced and a design-model for the compensator is derived. In §3 the compensator design is addressed via model-based and adaptive control techniques. The closed-loop system – i.e the interaction between plant and compensator – is investigated in §4: the performances of the two investigated compensators are compared on and off their design condition. Finally, the control of three-dimensional (3D) disturbances is addressed in §5 via an extension of the adaptive algorithm presented in §3.

CHAPTER 2

The plant

The plant is the system that we aim to control. In this work, we focus on a two-dimensional (2D) zero-pressure-gradient boundary layer flow. In the first instance, we will consider 2D disturbances only: this will allow us to reduce the number of sensors in the flow and introduce in a simpler way the control techniques that are discussed in this work. The three-dimensional (3D) disturbance case will be later discussed in §5.

A model that describes the plant is needed: the Navier-Stokes equations that govern this type of flow read

$$\frac{\partial \mathbf{u}}{\partial t} = -(\mathbf{u} \cdot \nabla) \mathbf{u} - \nabla p + \frac{1}{Re} \nabla^2 \mathbf{u} + \lambda \mathbf{u}, \quad (2.1)$$

$$0 = \nabla \cdot \mathbf{u}, \quad (2.2)$$

$$\mathbf{u}(\mathbf{x}, t)|_{\partial\Omega} = \mathbf{u}_b(\mathbf{x}), \quad (2.3)$$

$$\mathbf{u}(\mathbf{x}, 0) = \mathbf{u}_0(\mathbf{x}). \quad (2.4)$$

The velocity and pressure at position $\mathbf{x} = (X, Y)$ at time t are represented by $\mathbf{u}(\mathbf{x}, t)$ and $p(\mathbf{x}, t)$ respectively. The Reynolds number is defined as $Re = U_\infty \delta_0^* / \nu$, where U_∞ is the free-stream velocity, ν the viscosity and δ_0^* the displacement thickness in the beginning of the domain. On the boundaries $\partial\Omega$ of the computational domain Ω (see Figure 2.1), the conditions (2.3) are imposed: no-slip condition at the wall and asymptotic velocity in the upper boundary. A fringe technique is used to simulate inflow and outflow condition in the beginning and in the end of the domain (Nordström *et al.* 1999): the flow is considered periodic along the stream-wise direction and a volume forcing $\lambda(\mathbf{x})\mathbf{u}(\mathbf{x}, t)$ in the last part of the domain enforces periodicity along the stream-wise direction (grey region in Figure 2.1). More details on the numerical procedure can be found in Chevalier *et al.* (2007), where the pseudo-spectral DNS code used in this work is described.

2.1. A linear model of the flow

As we are interested in the dynamics of small disturbances, the following decomposition is introduced:

$$\mathbf{u}(\mathbf{x}, t) = \mathbf{U}(\mathbf{x}) + \epsilon \mathbf{u}'(\mathbf{x}, t), \quad (2.5)$$

$$p(\mathbf{x}, t) = P(\mathbf{x}) + \epsilon p'(\mathbf{x}, t). \quad (2.6)$$

6 2. THE PLANT

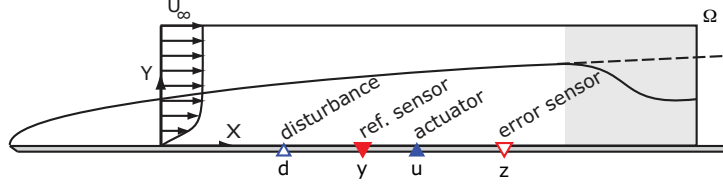


FIGURE 2.1. Computational domain Ω .

$\{\mathbf{U}(\mathbf{x}), P(\mathbf{x})\}$ is a steady solution of Navier-Stokes equation – i.e. the laminar boundary-layer solution – and $\{\mathbf{u}'(\mathbf{x}), p'(\mathbf{x})\}$ the perturbation. Applying this decomposition into (2.1-2.4) and neglecting the terms of order ϵ^2 , the linear set of equation is obtained:

$$\frac{\partial \mathbf{u}'}{\partial t} = -(\mathbf{U} \cdot \nabla) \mathbf{u}' - (\mathbf{u}' \cdot \nabla) \mathbf{U} - \nabla p' + \frac{1}{Re} \nabla^2 \mathbf{u}' + \lambda \mathbf{u}' + \mathbf{f}, \quad (2.7)$$

$$0 = \nabla \cdot \mathbf{u}', \quad (2.8)$$

$$\mathbf{u}'|_{\partial\Omega} = \mathbf{0}, \quad (2.9)$$

$$\mathbf{u}'(0) = \mathbf{0}. \quad (2.10)$$

The term $\mathbf{f}(\mathbf{x}, t)$ is used to model the forcing on the flow. Spatial and time dependency are decoupled as follows:

$$\mathbf{f}(\mathbf{x}, t) = \mathbf{b}_d(\mathbf{x}) d(t) + \mathbf{b}_u(\mathbf{x}) u(t), \quad (2.11)$$

where the disturbance and control signals $d(t)$ and $u(t)$ multiplies the respective spatial support $\mathbf{b}_d(\mathbf{x})$ and $\mathbf{b}_u(\mathbf{x})$. The measures $y(t)$ and $z(t)$ are defined by the integrals

$$y(t) = \int_{\Omega} \mathbf{c}_y(\mathbf{x}) \cdot \mathbf{u}'(\mathbf{x}, t) d\Omega + n(t), \quad (2.12)$$

$$z(t) = \int_{\Omega} \mathbf{c}_z(\mathbf{x}) \cdot \mathbf{u}'(\mathbf{x}, t) d\Omega, \quad (2.13)$$

where the kernels $\mathbf{c}_y(\mathbf{x})$ and $\mathbf{c}_z(\mathbf{x})$ define the sensors.

Let us introduce a general basis $\mathbf{T}(\mathbf{x}) \in \mathbb{C}^{1 \times N}$ on which the perturbation velocity $\mathbf{u}'(\mathbf{x}, t)$ can be expanded as

$$\mathbf{u}'(\mathbf{x}, t) \approx \mathbf{T}(\mathbf{x}) \mathbf{q}(t), \quad (2.14)$$

where $\mathbf{q}(t) \in \mathbb{C}^{N \times 1}$ is the vector of degrees of freedom. In this study, a Fourier-Chebyshev expansion over N_X - N_Y terms is considered, resulting in $N = N_X N_Y$ degrees of freedom. Via a Galerkin projection over $\mathbf{T}(\mathbf{x})$, it is possible to transform the partial differential equation (PDE) (2.7) in a ordinary differential equation (ODE) in time (Quarteroni 2009). The Linear Time-Invariant (LTI)

2.1. A LINEAR MODEL OF THE FLOW 7

system that results reads

$$\dot{\mathbf{q}}(t) = \mathbf{A} \mathbf{q}(t) + \mathbf{B}_d d(t) + \mathbf{B}_u u(t), \quad (2.15)$$

$$y(t) = \mathbf{C}_y \mathbf{q}(t) + n(t), \quad (2.16)$$

$$z(t) = \mathbf{C}_z \mathbf{q}(t), \quad (2.17)$$

where $\mathbf{A} \in \mathbb{C}^{N \times N}$ is the linearised Navier-Stokes operator. The matrices $\mathbf{B}_d, \mathbf{B}_u \in \mathbb{C}^{N \times 1}$ allows the two inputs $d(t)$ and $u(t)$ to force the system and the output matrices $\mathbf{C}_y, \mathbf{C}_z \in \mathbb{C}^{1 \times N}$ filter the state $\mathbf{q}(t)$ in order to provide the outputs signals $y(t)$ and $z(t)$. The stochastic signal $n(t)$ represents the measurement noise that affect the output and it is usually modelled by a white-noise signal.

2.1.1. *Reduced Order Model (ROM)*

Some control techniques require the direct knowledge of the system matrices \mathbf{A} , \mathbf{B} and \mathbf{C} . An example is the linear quadratic Gaussian (LQG) regulator that will be introduced in §3.1.1: this control technique requires the solution of a Riccati equation, which computational cost is proportional N^3 . Because of this, handling large system may lead to a very expensive design process and, eventually, to the impossibility of computing the control gains. Hence, system-reduction techniques applied to the Navier-Stokes linear operator are widely used to obtain smaller – and more handleable – systems that can reproduce the I/O behaviour of the flow (Rowley 2005; Ilak *et al.* 2010; Bagheri *et al.* 2009c).

In this study, the Eigensystem Realization Algorithm (ERA) is used to provide a reduced-order model (ROM) (Juang & Pappa 1985). This algorithm builds a realisation of an LTI system that mimics the original system defined by $\{\mathbf{A}, \mathbf{B}, \mathbf{C}\}$ starting from its impulse responses from each input to each output. The system obtained by the ERA reads

$$\frac{\partial \mathbf{q}_r(t)}{\partial t} = \mathbf{A}_r \mathbf{q}_r(t) + \mathbf{B}_{r,d} d(t) + \mathbf{B}_{r,u} u(t) \quad (2.18)$$

$$y(t) = \mathbf{C}_{r,y} \mathbf{q}_r(t) + n(t) \quad (2.19)$$

$$z(t) = \mathbf{C}_{r,z} \mathbf{q}_r(t) \quad (2.20)$$

where $\mathbf{A}_r \in \mathbb{R}^{N_r \times N_r}$ is the ROM state matrix, $\mathbf{q}_r(t) \in \mathbb{R}^{N_r \times 1}$ is the state vector, $\mathbf{B}_{r,d}, \mathbf{B}_{r,u}, \mathbf{C}_{r,y}^T, \mathbf{C}_{r,z}^T \in \mathbb{R}^{N_r \times 1}$ are the I/O matrices and $N_r \ll N$. This method is equivalent to a projection of the full system $\{\mathbf{A}, \mathbf{B}, \mathbf{C}\}$ on the set of its N_r most energetic Balanced Proper-Orthogonal-Decomposition (BPOD) modes (Moore 1981; Bagheri *et al.* 2009b).

The model-reduction procedure implies an information loss, that eventually leads to an error: this algorithm allows to have a direct estimation of this error as a function of the ROM size (Moore 1981). This estimation can be used to chose the ROM size in order to bound the error to a given tolerance.

8 2. THE PLANT

2.1.2. *Finite Impulse Response (FIR) representation*

In other control techniques the knowledge of the system is relaxed to its Input/Output (I/O) relations only. Consider the forced response of a LTI system to a generic input signal $u(t)$ can be written as

$$z(t) = \mathbf{C}_z e^{\mathbf{A}t} \mathbf{q}_0 + \int_0^t \mathbf{C}_z e^{\mathbf{A}\tau} \mathbf{B}_u u(t - \tau) d\tau. \quad (2.21)$$

If the system is stable, for t large enough the first term goes to zero and the system response is dependent only from the forcing $u(t)$:

$$z(t) = \int_0^t \mathbf{C}_z e^{\mathbf{A}\tau} \mathbf{B}_u u(t - \tau) d\tau = \int_0^t P_{zu}(\tau) u(t - \tau) d\tau \quad (2.22)$$

where P_{zu} is the convolution kernel. The kernel is able to describe completely the Input/Output relation between the input $u(t)$ and the output $z(t)$ but losing all the information about the state $\mathbf{q}(t)$.

The time-discrete counterpart of (2.22) is of particular interest when it comes to control techniques. The time-discrete output signal $z(n) = z(n\Delta t)$ is computed as a linear combination of the time-discrete history of the input signal $u(n) = u(n\Delta t)$:

$$z(n) = \sum_{j=0}^n P_{zu}(j) u(n - j). \quad (2.23)$$

Since the system is stable, the convolution kernel goes to zero as the shifting index i grows: this permits us to truncate the sum at an appropriate time $N_z u \Delta t$. Hence, the signal $z(n)$ can be obtained by the finite sum

$$z(n) \approx \sum_{j=0}^{N_z u} P_{zu}(j) u(n - j). \quad (2.24)$$

The expression (2.24) is called Finite Impulse Response (FIR) filter.

Being so, the Input/Output relation $u \rightarrow z$ can be described by a finite number of coefficients $P_{zu}(i)$. These coefficients can be both computed from a linear model of the flow as the one provided by (2.15–2.17) or identified from experiments by dedicated algorithms, e.g. Least Mean Square (LMS). For more information, we refer to Paper 1.

CHAPTER 3

The compensator

The compensator is the system that interacts with the plant via its control inputs and outputs in order to pilot it at the desired state. In this brief review, we will focus on linear compensators, i.e. compensators that are ascribable to a linear dynamical system (Figure 3.1). If the system that describe the compensator is time-invariant, the compensator is called static: the control law is pre-computed, usually based on a model of the system and then the compensator is connected to the plant. If the response of the compensator, instead, can be modified on-line, the compensator is called adaptive

In the following sections, we will introduce two types of compensator, examples of these two families. For a more detailed review we refer to Paper 1.

3.1. Model-based control

This family groups all those static compensators that are based on a model of the plant that can be either numerical (Bewley & Liu 1998; Bagheri & Henningson 2011; Semeraro *et al.* 2013, e.g.) or experimentally identified Juillet *et al.* (2014). The model is then used to compute the response of the actuator: typical examples are Model Predictive Control (MPC) and the linear Quadratic Gaussian (LQG) regulator, discussed herein.

3.1.1. Linear Quadratic Gaussian (LQG) regulator

The LQG regulator design is bases on a complete model of the plant: it results in a LTI system that mimics the plant in order to compute a proper control signal $u(t)$, given the measurement signal $y(t)$ as an input. The compensator reads

$$\frac{\partial \hat{\mathbf{q}}_r(t)}{\partial t} = (\mathbf{A}_r + \mathbf{L}\mathbf{C}_{r,y}) \hat{\mathbf{q}}_r(t) + \mathbf{B}_{r,u} u(t) - \mathbf{L}y(t) \quad (3.1)$$

$$u(t) = \mathbf{K} \hat{\mathbf{q}}_r(t) \quad (3.2)$$

where $\hat{\mathbf{q}}_r(t) \in \mathbb{R}^{N_r \times 1}$ is the compensator state vector. The subscript r refers to the Reduced Order Model (ROM) of the flow discussed in §2.1.1. The compensator is composed by two parts: the observer (84) and the controller (3.2). The former filters the measurement signal $y(t)$ by the estimation gain matrix $\mathbf{L} \in \mathbb{R}^{N_r \times 1}$ and reconstructs an estimation $\hat{\mathbf{q}}_r(t)$ of the state of the

10 3. THE COMPENSATOR

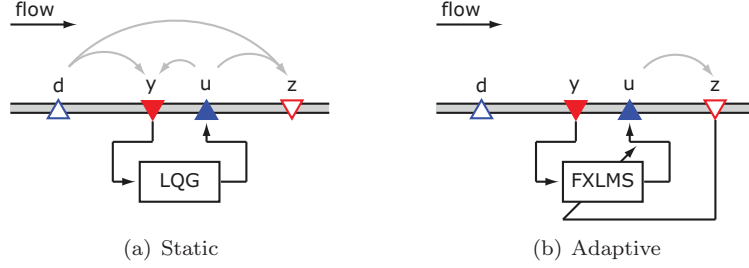


FIGURE 3.1. Compensator schemes for static (LQG) and adaptive (FXLMS) strategies. An adaptive scheme may also use the error signal $z(t)$ to adapt to the current flow conditions. The grey lines indicate the I/O relations required to be modelled by each strategy.

controlled system $\mathbf{q}_r(t)$. The latter computes the control signal filtering the estimated state $\hat{\mathbf{q}}_r(t)$ and the control gain matrix $\mathbf{K} \in \mathbb{R}^{1 \times N_r}$.

3.1.1.1. *Observer: Kalman filter*

The observer is designed to minimise the the covariance of the difference between the plant state \mathbf{q}_r and the estimated state $\hat{\mathbf{q}}$ when the system is excited by an unknown white-noise signal $d(t)$. To do this, the observer uses the measurement $y(t)$ affected by an error $n(t)$, also modelled as white noise, and the control signal $u(t)$. The minimization procedure leads to

$$\mathbf{L} = -\mathbf{Y}\mathbf{C}_{r,y}^H R_n^{-1} \quad (3.3)$$

where $\mathbf{Y} \in \mathbb{R}^{N_r \times N_r}$ is the solution to the Riccati equation:

$$\mathbf{A}_r \mathbf{Y} + \mathbf{Y} \mathbf{A}_r^H - \mathbf{Y} \mathbf{C}_{r,y}^H R_n^{-1} \mathbf{C}_{r,y} \mathbf{Y} + \mathbf{B}_{r,d} R_d \mathbf{B}_{r,d}^H = \mathbf{0} \quad (3.4)$$

The parameters R_d and R_n are the expected variances of the disturbance signal $d(t)$ and measurement noise signal $n(t)$.

3.1.1.2. *Controller: Linear Quadratic Regulator (LQR)*

LQR design relies on the knowledge of the state \mathbf{q}_r , or its estimation $\hat{\mathbf{q}}_r$. The procedure is based on the minimization of a quadratic cost-function based on the error-sensor measurements $z(t)$ and on the control signal $u(t)$

$$\mathcal{N} = \int_0^\infty z(t) w_z z(t) + u(t) w_u u(t) dt. \quad (3.5)$$

The ratio between the control-strength parameter w_u and the performance parameter w_z allows to design a controller capable to attenuate the disturbances in the system, while limiting the control effort. The minimisation procedure leads to the control law in (3.2) where the control-gains matrix reads

$$\mathbf{K} = -w_u^{-1} \mathbf{B}_{r,u}^H \mathbf{X}. \quad (3.6)$$

The matrix $\mathbf{X} \in \mathbb{R}^{N_r \times N_r}$ is the solution of the Riccati equation

$$\mathbf{A}_r^H \mathbf{X} + \mathbf{X} \mathbf{A}_r - \mathbf{X} \mathbf{B}_{r,u} w_u^{-1} \mathbf{B}_{r,u}^H \mathbf{X} + \mathbf{C}_{r,z}^H w_z \mathbf{C}_{r,z} = \mathbf{0} \quad (3.7)$$

Note that the controller design is completely independent from the observer design and vice-versa. This is commonly known as *separation principle* (Glad & Ljung 2000).

3.2. Adaptive control

In an adaptive control method the compensator adjusts on-line its response in order to optimise its performances: usually this is achieved by monitoring its own performances and, based on those, compute the magnitude of the adjustments. A typical example of this kind of compensator is the Filtered-X Least-Mean-Square (FXLMS) algorithm, investigated by Sturzebecher & Nitsche (2003) and Kurz *et al.* (2013) to attenuate 2D disturbances in a boundary-layer flow.

3.2.1. Filtered-X Least-Mean-Square (FXLMS) algorithm

The FXLMS algorithm, like the LQG regulator, relies on a minimisation procedure that is however performed on-line. This allows the algorithm to use the actual measurements from the flow, giving this method the adaptive qualities that characterise it.

The compensator is again a linear system. As seen in §2.1.2 for the plant, a linear system can be represented both in state-space form (like the LQG regulator in the previous section) or by a Finite Impulse Response (FIR) filter. This control technique uses the latter representation: hence, the control signal is given by

$$u(n) = \sum_{i=1}^{N_K} K(i) y(n-i) \quad (3.8)$$

where $u(n) = u(n \Delta t)$ and $y(n) = y(n \Delta t)$ are the time-discrete representations of the time-continuous signals $u(t)$ and $y(t)$ and Δt is the sampling time step. The N_K coefficients $K(i)$ are the kernel of the filter and they are related to the impulse response of the compensator. Those coefficients are updated at each time step in order to satisfy the minimisation problem

$$\min_{K(i)} z^2(n) \quad (3.9)$$

via a steepest-descend algorithm is used. The updating law that results is

$$K(i|n+1) = K(i|n) + \mu z(n) \sum_{j=1}^{N_{zu}} P_{zu}(j) y(n-i-j). \quad (3.10)$$

Note that the knowledge of the plant is limited to the time-discrete kernel $P_{zu}(i)$ that describes the I/O relation $u \rightarrow z$.

CHAPTER 4

The closed-loop system

In the previous two chapters the plant and the compensator are introduced separately. In this chapter the interaction between them is investigated: the compensator is paired to the plant and its performance evaluated via DNS simulations.

The simulated environment replicates the experimental conditions in Paper 2. The sensors y and z are modelled as surface mounted hot-wires – i.e. measurements of the local friction fluctuations – and the actuator u is modelled as a plasma actuator, using the experimental results by Kriegseis *et al.* (2013). The computational domain Ω extends $700\delta_0^*$ in the stream-wise direction and $30\delta_0^*$ in the wall-normal direction. The fringe region extends for $150\delta_0^*$ in the last part of the domain. Fourier expansion over $N_X = 768$ modes is used to approximate the solution along the stream-wise direction, while Chebyshev expansion is used in the wall-normal direction on $N_Y = 101$ Gauss-Lobatto collocation points. The Reynolds number Re at the inlet is set to 656. A second Reynolds number based on the X coordinate is also defined as

$$Re_X = \frac{U_\infty (X - X_{LE})}{\nu}, \quad (4.1)$$

where X_{LE} is the leading-edge position.

The instantaneous stream-wise component of the velocity fluctuation is reported in Figure 4.1. The disturbance source is excited by a white-noise signal $d(t)$ with variance $R_d = 1/9$, generating a train of random TS-wave in the flow that is damped by the actuator u governed by the compensator. A white noise signals with variance $R_n = 1/9 \cdot 10^{-2}$ is added to the measurement signals $y(t)$ and $z(t)$ in order to model the experimental measurement noise. The color maps show the controlled case when LQG (upper plot) and FXLMS (lower plot) are used while the contours report the uncontrolled simulations data. Both the compensator are able to reduce the amplitude of the disturbances in the flow: however, the model-based control shows better performance than the adaptive controller.

In order to better quantify the performance gap between the two control strategies, a time-averaged measurement of the TS-wave amplitude based on the perturbation energy at each stream-wise location is introduced

$$A_e^2(X) = \frac{1}{L_Y T} \int_0^{L_Y} \int_0^T |\mathbf{u}'(\mathbf{x}, t)|^2 dt dY \quad (4.2)$$

4. THE CLOSED-LOOP SYSTEM 13

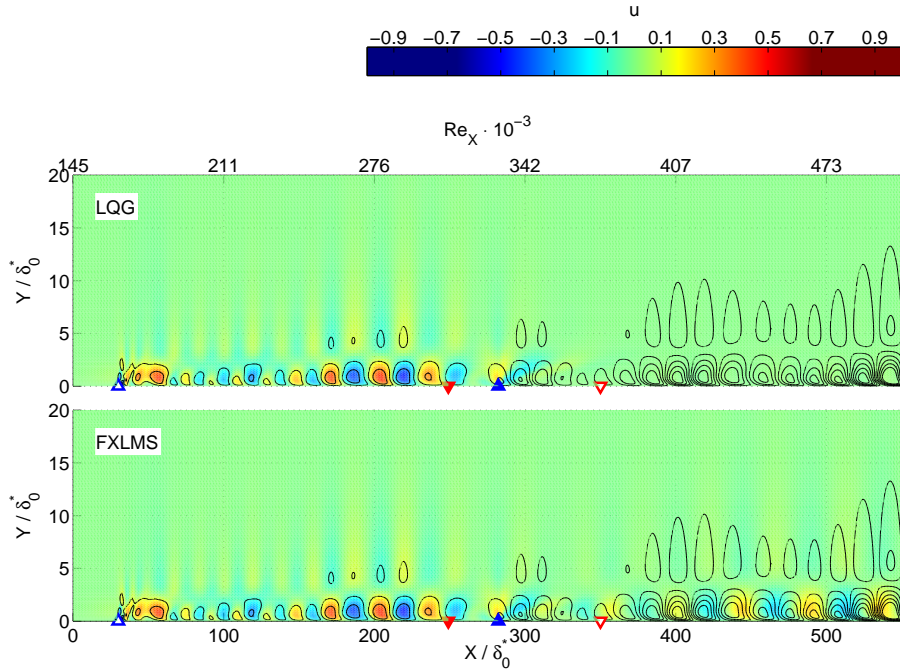


FIGURE 4.1. Color maps report the instantaneous stream-wise component of the velocity when LQG (upper) and FXLMS (lower) compensators are employed. The contours report the corresponding uncontrolled case.

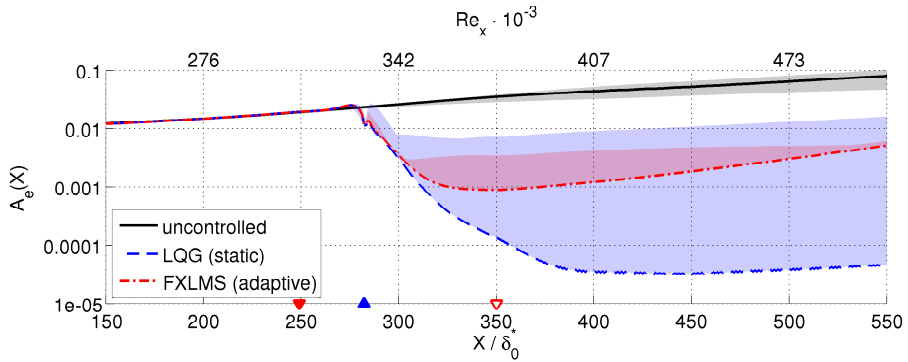


FIGURE 4.2. TS amplitude $A_e(X)$. The lines report the performances of the two compensators at the design condition. The shaded regions indicate the performance variation when the asymptotic velocity is changed in a $\pm 10\%$ range with respect to the design condition.

14 4. THE CLOSED-LOOP SYSTEM

The solid lines in Figure 4.2 show A_e at the design condition for an averaging time $T = 7000 \frac{\delta^*}{U_\infty}$. The performance difference between the two control strategies is clear: the model-based compensator cancels almost completely the disturbance downstream the actuator. The adaptive algorithm, instead, is able only to attenuate the upcoming TS-wave that starts growing again downstream the error sensor.

4.1. The importance of being adaptive

The pure performance at the design condition is not the only parameter that should be taken into account when evaluating a control technique: the reliability of the controller is also crucial. Unfortunately, the outstanding performance of the LQG compensator degrades as the flow departs from the design condition. This event is typical of real flow experiments where a perfect match between model and reality can be easily a difficult issue, as shown in Paper 2.

In fact, the perfect match between real flow and design model is conditional to the guaranteed optimal performance of the LQG regulator (Doyle 1978). The shaded areas in Figure 4.2 represent the performance variation of the two algorithms when the free stream velocity is varied in a 10% range respect to the design condition: LQG performance drastically decreases until being overtaken by the FXLMS compensator. The adaptive algorithm, in fact, is able to adjust its response to overcome the modelling errors and ensure an effective wave cancellation (Paper 1,2). This result suggests that an adaptive controller is to be preferred in those application where an accurate model of the flow is not available.

CHAPTER 5

The third dimension

In the previous chapters the hypothesis of a purely $2D$ flow has been made to facilitate the study. This permitted to easily highlight advantages and drawbacks of the investigated control techniques. However, in real environments this hypothesis is far from reasonable. Hence, it is necessary to address the control problem allowing a disturbance to develop in three dimensions.

The numerical and experimental work by Li & Gaster (2006) falls into this framework: the control of three-dimensional (3D) disturbances via the superposition of counter-phase waves is addressed by using a simple algebraic model of the flow. Also the LQG approach has been tested in 3D disturbance environment: we recall the pioneering work by Semeraro *et al.* (2013), where the control of single wave-packets is addressed by localised sensors and actuators. All the sensors and actuators were connected by each other by the compensator: this would lead to a prohibitive increasing of the compensator complexity if a large spanwise portion of the flow is meant to be controlled. In the more recent work in Paper 3, the possibility to limit the number of interconnections between sensor and actuators is investigated by dividing them in equal sets along the span-wise direction, each commanded by one compensator. This structure, called *control units*, is thus replicated along the span-wise direction in order to fill the entire domain.

The study presented in this chapter is a further development of this idea. However, the modularity of the control action is not based on an a-priori division in control units but rather on considerations about the control kernel. A similar set-up to Paper 3 is considered: a distributed 3D disturbance field is generated using a span-wise row of independent random forcings d (Figure 1), generating a complex 3D random pattern of disturbances. The control action is performed by a row of localised, equispaced actuators forcing the flow in the proximity of the wall. Similarly to the 2D case, their action $u_i(t)$ is computed based on the measurements $y_m(t)$ by a row of sensors upstream the actuators: for this set-up, the number of sensors is equal to the number of actuators and they are positioned aligned with the flow direction (Figure 5.2).

5.1. A “three-dimensional” compensator

A linear control law is assumed

$$u_l(n) = \sum_m \sum_i K_{ml}(i) y_m(n-i) \quad \forall l \quad (5.1)$$

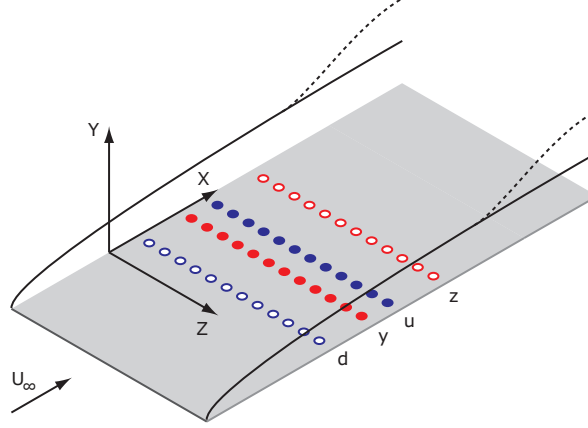


FIGURE 5.1. 3D control set-up. Random 3D disturbances are generated by a row of localised independent forcings d . The measurements from the sensors y and z are used to compute the actuation signal for the actuators u in order to reduce the amplitude of the detected disturbances.

where $K_{ml}(i) \in \mathbb{R}^{M \times M}$ is the convolution kernel of the compensator. As a consequence, the number of transfer functions between the M sensors y_m and the M actuators u_l is M^2 . This imposes a computational constraint when M is large, which is the case when covering a large spanwise width with the controller. However, since the flow is spanwise homogeneous, the same transfer function K_m from all the sensors y_{m+l} to one arbitrary actuator u_l is replicated for each actuator u_m , as shown in Figure 5.2. This assumption reduces the number of transfer functions to be designed from M^2 to M . Hence, the Finite Impulse Response (FIR) filter representation of the control law reads

$$u_l(n) = \sum_m \sum_i K_m(i) y_{m+l}(n-i) \quad \forall l \quad (5.2)$$

where one kernel dimension is suppressed and, as a consequence, $K_m(i) \in \mathbb{R}^{M \times 1}$.

5.1.1. Multi-Input Multi-Output (MIMO) FXLMS

A Multi-Input Multi-Output (MIMO) version of the FXLMS algorithm introduced in §3.2.1 is used to dynamically design the compensator. The algorithm minimise the sum of the squared measurement signals $z_l(n)$:

$$\min_{K_m} \left(\sum_l z_l^2(n) \right). \quad (5.3)$$

Hence the kernel is updated via a steepest descent algorithm at each time step:

$$K_m(i|n+1) = K_m(i|n) - \mu \lambda_m(i|n). \quad (5.4)$$

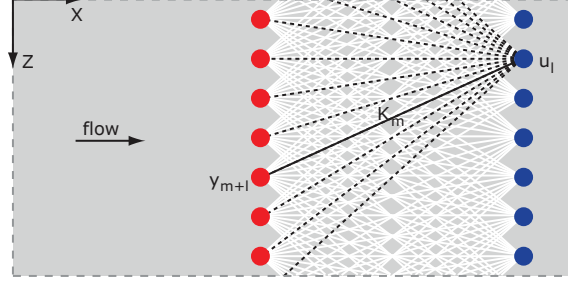


FIGURE 5.2. Compensator structure. The action of each actuator u_l is computed by filtering the signals from all the sensor y_{m+l} via a linear filter K_m .

where the descend direction $\lambda_m(j|n)$ is given by

$$\lambda_m(i|n) = \frac{\partial (\sum_l z_l^2(n))}{\partial K_m(i)} = 2 \sum_l z_l(n) \frac{\partial z_l(n)}{\partial K_m(i)}. \quad (5.5)$$

In order to compute the derivative in the previous equation, it is necessary to explicit $z(n)$ dependencies:

$$\begin{aligned} z_l(n) &= \sum_r \sum_j P_{zd,r}(j) d_{r+l}(n-j) + \sum_r \sum_j P_{zu,r}(j) u_{r+l}(n-j) = \\ &= [\dots] + \sum_r \sum_j P_{zu,r}(j) \sum_m \sum_i K_m(i) y_{m+r+l}(n-j-i) = \\ &= [\dots] + \sum_m \sum_i K_m(i) \sum_r \sum_j P_{zu,r}(j) y_{r+m+l}(n-j-i) = \\ &= [\dots] + \sum_m \sum_i K_m(i) f_{m+l}(n-i), \end{aligned} \quad (5.6)$$

where the same span-wise homogeneity assumption has been made for the plant kernels $P_{zd,r}(j)$ and $P_{zu,r}(j)$ that represent the transfer functions $d_r \rightarrow z_l$ and $u_r \rightarrow z_l$ respectively. Hence the descend direction reads

$$\lambda_m(i|n) = 2 \sum_l z_l(n) \frac{\partial z_l(n)}{\partial K_m(i)} = 2 \sum_l z_l(n) f_{m+l}(n-i). \quad (5.7)$$

This expression – but the sum – is similar to the expression of $\lambda(i|n)$ in the 2D case in (3.10).

5.2. Preliminary results

In order to analyse the control algorithm, LES simulations are performed. The flow is expanded over 1536×384 Fourier modes in the XZ plane and 101 Chebyshev’s polynomials in the wall-normal direction. The computational domain Ω extends for $[0, 2000\delta_0^*] \times [0, 30\delta_0^*] \times [-125\delta_0^*, 125\delta_0^*]$ in the X , Y and Z direction. The simulation Reynolds number is $Re = \frac{U_\infty \delta_0}{\nu} = 1000$.

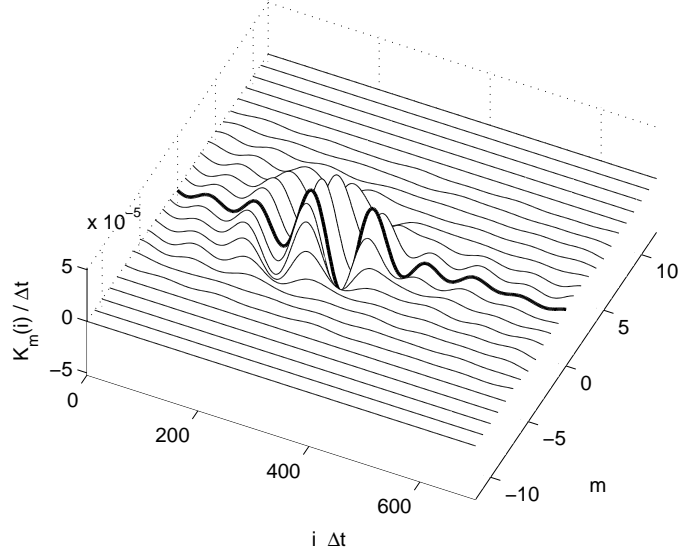


FIGURE 5.3. Convolution kernel $K_m(i)$ computed by FXLMS algorithm. The thickened line indicates the kernel $K_0(i)$ connecting the actuator u_l and the sensor y_l at the same stream-wise location.

Sensor and actuator shapes are modelled according to Semeraro *et al.* (2013): 25 equispaced objects are considered for each row of sensors/actuators/disturbances, resulting in a span-wise separation $\Delta Z = 10$. The disturbance inputs are fed by 25 independent white noise signals $d_m(t)$ with variance $1/3 \cdot 10^{-3}$ each.

The control kernel $K_m(i)$ computed by the FXLMS algorithm is shown in Figure 5.3. Each line indicates the transfer function $K_m(i)$ between a generic actuator u_l and the sensor y_{m+l} that is positioned at $m \Delta Z$ with respect to the actuator itself (Figure 5.2). The thick line in Figure 5.3 shows the transfer function $K_0(i)$, i.e. the connection between the sensor and the actuator positioned at the same Z location. The time-delay that characterise this type of flows can be detected also in the compensator response: if we consider $K_0(i)$ – i.e. the connection between the sensor and the actuator positioned at the same Z location – the maximum of the transfer function occurs at $j \Delta t \approx 250$, which corresponds to the time that takes a TS-wavepacket to travel from sensor to actuator location (Schmid & Henningson 2001). Moreover, As the index m increases the magnitude of the transfer functions decays and it becomes zero for $m = \pm 5$: this means that the action of one actuator depends only on a limited number of sensors, in this case the ones between $Z = -50\delta_0^*$ and $Z = 50\delta_0^*$ with respect to the actuator position. This will permit to reduce the number

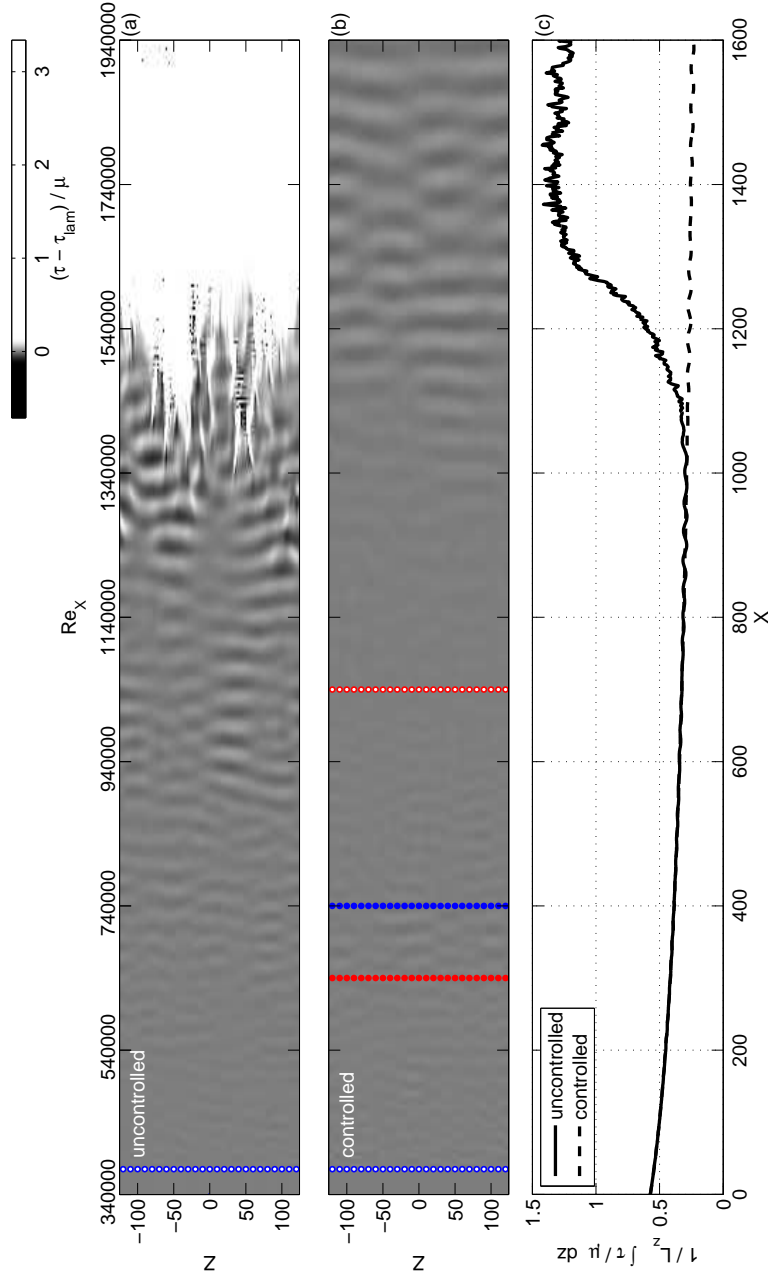


FIGURE 5.4. Transition delay. In (a) and (b) the skin friction fluctuations respect to the laminar solution are shown at $t = 4000 \frac{\rho_0}{U}$. (c) reports the span-wise averaged friction along the stream-wise direction. The top axis reports $Re_x = \frac{U_\infty (X - X_{LE})}{\nu}$, where X_{LE} is the leading-edge position.

20 5. THE THIRD DIMENSION

of transfer functions that have to be calculated and, as a consequence, reduce the compensator computational cost.

The transition delay performed by the compensator is shown in Figure 5.4. The friction-traces of the TS-waves are visible in Figure 5.4(a-b), where the instantaneous skin-friction fluctuations with respect to the laminar solution are reported. The disturbances grow exponentially while travelling downstream and lead to transition in the uncontrolled case. In Figure 5.4(b) it can be seen that the compensator is able to attenuate the TS-waves and move the transition point out of the computational domain. In the controlled case the disturbances reach a minimum amplitude where the error sensors z_l are positioned and again without triggering the transition within the computational box. This can be seen also in Figure 5.4(c) where the span-wise average of the stream-wise stress is shown: the area between the controlled and uncontrolled friction curves gives directly the drag-save per unit of span-wise length that is obtained by applying the control.

CHAPTER 6

Summary of the papers

Paper 1

Adaptive and Model-Based Control Theory Applied to Convectively Unstable Flows

A review of the control methodologies aimed to delay the laminar-to-turbulent transition in convectively unstable flows is presented. A simple one-dimensional system – the Kuramoto-Sivashinsky (KS) equation – able to replicate the stability of this type of flows is introduced to illustrate the different techniques via applied-control examples.

The compensator design is investigated as a coupling of a controller and an estimator. The former is responsible to compute the control signal assuming a complete knowledge of the system state. Optimal control techniques are reviewed: Linear Quadratic Regulator (LQR) and Model Predictive Control (MPC) are examined, in particular when saturation constraints are applied to the actuator. The estimator, instead, provides to the controller an estimation of the system state based on limited measurements in the flow. The conventional Kalman filter is introduced as system identification techniques borrowed from signal-processing theory.

In the end, the complete compensator is analysed. The difference between static (LQG) and adaptive (FXLMS) compensators is investigated, highlighting a strong sensitivity of the static controller to inaccuracies of the model used in the design process.

Scripts to generate all the presented data and figures are available in MATLAB format at <http://www.mech.kth.se/~nicolo/ks/>.

Paper 2

On the role of adaptivity for robust laminar flow control

The control problem is addressed in an experimental set-up in order to investigate the necessity of adaptivity in real flow applications. A FXLMS adaptive compensator is compared with a model-based LQG regulator in attenuating 2D TS-wave in a zero-pressure-gradient boundary layer flow.

22 6. SUMMARY OF THE PAPERS

The experiments are conducted in the open-circuit wind tunnel at TU Darmstadt, Germany. A 2D disturbance is generated TS-wave by a disturbance source and downstream detected by a surface-mounted hot-wire sensor. Based on these measurements, the compensator prescribe a suitable forcing to a dielectric-barrier-discharge (DBD) plasma actuator to cancel the upcoming wave. A second hot-wire sensor is placed farther downstream to monitor the compensator performance. DNS simulations of the experimental set-up are designed and, based on these, the LQG regulator is designed.

The model-based regulator is found to be less effective than the FXLMS compensator because of unavoidable modelling inaccuracies. Moreover, the performance of the LQG regulator degrades as the flow response depart from the design model. In particular, free-stream velocity variation are investigated: the static compensator shows not to be able to prescribe the correct phase information to the actuator. Otherwise, the adaptive compensator is able to autonomously adjust to the modified flow conditions and effectively perform the control action for a broader interval of velocity variations.

Paper 3

Centralised versus Decentralised Active Control of Boundary Layer Instabilities

The control of 3D disturbances in a zero-pressure-gradient boundary-layer flow is addressed via model-based optimal control. In particular, this work focuses on the possibility to divide and replicate the control law along the homogeneous span-wise direction in order to reduce the complexity of the controller.

DNS simulations are performed to investigate the control performance. Evenly localised objects are distributed in the spanwise direction in the wall region (18 disturbances sources, 18 actuators, 18 estimation sensors and 18 objective sensors) and span-wise subsets of these objects are identified by signal-energy based techniques. LQG compensators are designed on these subset and replicated along the span-wise direction to fill the computational domain. Hence, the performance loss due to the missing connections are evaluated in order to identify a “minimal” control unit, i.e. a minimal subset of sensors and actuators able to perform an effective control action.

CHAPTER 7

Conclusions and outlook

Adaptive vs. model-based control

The model-based approach reveals very sensitive to model inaccuracies: even if the LQG regulator is capable of optimal performance at the design condition, its performance quickly degrades as the actual plant departs from the design model. On the other hand, the adaptive FXLMS compensator shows to be able to maintain its performances even if unexpected changes occur in the flow conditions. In particular, it is found that in the tested conditions the FXLMS compensator is capable of a larger disturbance attenuation than the LQG regulator when the free-stream velocity varies by $\pm 10\%$ with respect to the design condition.

We can claim that the model-based approach is not suitable for those applications where an accurate model of the plant is not available. This is supported also by the experimental results reported in Paper 2: it is shown that in a practical test a model-based control is unlikely able to perform better than an adaptive controller, because of modelling errors that may easily occur in the design process.

Control of three-dimensional disturbances

The control of 3D disturbances is addressed via a MIMO extension of the FXLMS presented for the 2D case: the preliminary results show a real capability of the algorithm to effectively delay transition in a simulated environment.

Moreover, it is found that a reference sensor commands only a limited number of actuators. This phenomenon – that is physically ascribable to the limited span-wise spreading of the detected wave-packet – may lead to a reduction of the computational cost of the algorithm and will be the subject of further investigations.

These results take us a step forward towards the final aim of this project, i.e. performing the control of 3D disturbances in a wing boundary-layer in real-flight experiments. However, the hypothesis of an equal number of sensors and actuators is unlike in real applications, if plasma actuators are considered. This is due to the experimental unfeasibility of driving a large number of independent plasma actuators (Simon 2014). That being said so, the next step that has to be taken is to investigate the control problem when an uneven number of sensors and actuators is considered.

Acknowledgements

I would like to thank Prof. Dan S. Henningson for his guidance and for giving me this opportunity and Dr. Shervin Bagheri for constructively discussing my ideas and leading them to more rigorous (and elegant) formulations. I am also grateful to Dr. Reza Dadfar for the fruitful collaboration during this second year of my PhD. My deepest gratitude goes to Dr. Onofrio Semeraro for his invaluable help and the endless discussions about life, research and everything.

I would also like to thank Dr.-Ing. Sven Grundmann and Bernhard Simon for the productive month spent in Darmstadt and for showing me that a flow is not only a simulation result.

Thanks to all the people that I had the opportunity to meet here in Sweden, in particular to Cristina that I met by chance and became my sister-in-Sweden. Thanks to Cecilia¹, Nima, Armin, Taras, Ellinor, Jacopo and all the other colleagues of mine for making the office not only a nice place to work but also a nice place to be. Thanks to all my fencing team-mates for being nice friends before and combative rivals after each “*in guardia*”. Thanks to Martà, Michele, Karin, Luca and Beatrice for enjoying with me Stockholm and its beauty. Thanks to Francesca for stealing my toothpaste and giving me an always-good reason to wear sunglasses for breakfast.

A special thanks goes to all the people I left in Italy when I moved to Sweden: you always make me happy to come back and sad to leave you again. Above all, I would like to thank my best friend Alberto and his wife Agnese for being such wonderful friends to me.

Finally, I thank my mother for supporting me in every moment of my life and my father for making me fall in love with science. I would not be here without the two of you.

¹Thanks also for patiently proofreading the introduction of this thesis.

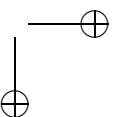
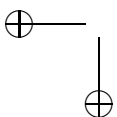
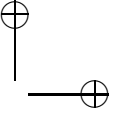
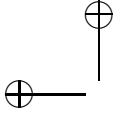
Bibliography

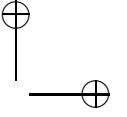
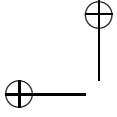
- BAGHERI, S., BRANDT, L. & HENNINGSON, D. S. 2009a Input–output analysis, model reduction and control of the flat-plate boundary layer. *J. Fluid Mech.* **620** (1), 263–298.
- BAGHERI, S. & HENNINGSON, D. S. 2011 Transition delay using control theory. *Philos. Trans. R. Soc.* **369**, 1365–1381.
- BAGHERI, S., HEPFFNER, J., SCHMID, P. J. & HENNINGSON, D. S. 2009b Input-Output Analysis and Control Design Applied to a Linear Model of Spatially Developing Flows. *Appl. Mech. Rev.* **62**.
- BARBAGALLO, A., SIPP, D. & SCHMID, P. J. 2009 Closed-loop control of an open cavity flow using reduced order models. *J. Fluid Mech.* **641**, 1–50.
- BELSON, B. A., SEMERARO, O., ROWLEY, C. W. & HENNINGSON, D. S. 2013 Feedback control of instabilities in the two-dimensional Blasius boundary layer: The role of sensors and actuators. *Phys. Fluids* **25**.
- BEWLEY, T. R. & LIU, S. 1998 Optimal and Robust Control and Estimation of Linear Paths to Transition. *J. Fluid Mech.* **365**, 305–349.
- CHEVALIER, M., SCHLATTER, P., LUNDBLADH, A. & HENNINGSON, D. S. 2007 A pseudo-spectral solver for incompressible boundary layer flows. *Tech. Rep. TRITA-MEK 2007:07*. KTH Mechanics, Stockholm, Sweden.
- DOYLE, J. C. 1978 Guaranteed Margins for LQG Regulators. *IEEE Trans. Autom. Control* **AC-23** (4), 756–757.
- DUCHMANN, A., GRUNDMANN, S. & TROPEA, C. D. 2013 Delay of Natural Transition with Dielectric Barrier Discharges. *Exp. Fluids* **54** (3), 1–12.
- GLAD, T. & LJUNG, L. 2000 *Control Theory*. London: Taylor & Francis.
- GOLDIN, N., KING, R., PÄTZOLD, A., NITSCHKE, W., HALLER, D. & WOIAS, P. 2013 Laminar Flow Control With Distributed Surface Actuation: Damping Tollmien-Schlichting Waves with Active Surface Displacement. *Exp. Fluids* **54** (3), 1–11.
- ILAK, M., BAGHERI, S., BRANDT, L., ROWLEY, C. W. & HENNINGSON, D. S. 2010 Model Reduction of the Nonlinear Complex Ginzburg-Landau Equation. *SIAM J. Appl. Dyn. Sys.* **9** (4), 1284–1302.
- JUANG, J.-N. & PAPPA, R. S. 1985 An eigensystem realization algorithm for modal parameter identification and model reduction. *J. Guid., Con. Dyn.* **8** (5), 620–627.
- JUILLET, F., MCKEON, B. J. & SCHMID, P. J. 2014 Experimental Control of Natural Perturbations in Channel Flow. *J. Fluid Mech.* **752**, 296–309.

- KRIEGSEIS, J., SCHWARZ, C., TROPEA, C. & GRUNDMANN, S. 2013 Velocity-Information-Based Force-Term Estimation of Dielectric-Barrier Discharge Plasma Actuators. *J. Phys. D* **46** (5), 055202.
- KURZ, A., GOLDIN, N., KING, R., TROPEA, C. D. & GRUNDMANN, S. 2013 Hybrid Transition Control Approach for Plasma Actuators. *Exp. Fluids* **54** (11), 1–4.
- LI, Y. & GASTER, M. 2006 Active Control of Boundary-Layer Instabilities. *J. Fluid Mech.* **550**, 185–205.
- LUNDELL, F. 2007 Reactive control of transition induced by free-stream turbulence: an experimental demonstration. *J. Fluid Mech.* **585**, 41–71.
- MOORE, B. 1981 Principal Component Analysis in Linear Systems: Controllability, Observability, and Model reduction. *IEEE Trans. Autom. Control* **26** (1), 17–32.
- NORDSTRÖM, J., NORDIN, N. & HENNINGSON, D. 1999 The fringe region technique and the Fourier method used in the direct numerical simulation of spatially evolving viscous flows. *SIAM J. Sci. Comp.* **20** (4), 1365–1393.
- QUARTERONI, A. 2009 *Numerical Models for Differential Problems*. Springer.
- ROWLEY, C. W. 2005 Model reduction for fluids, using balanced proper orthogonal decomposition. *Intl J. of Bifurcation and Chaos* **15** (03), 997–1013.
- SARIC, W. S., REED, H. L. & KERSCHEN, E. J. 2002 Boundary-layer Receptivity to Freestream Disturbances. *Ann. Rev. Fluid Mech.* **34** (1), 291–319.
- SCHMID, P. J. & HENNINGSON, D. S. 2001 *Stability and Transition in Shear Flows. Applied Mathematical Sciences* v. 142. Springer-Verlag.
- SEMERARO, O., BAGHERI, S., BRANDT, L. & HENNINGSON, D. S. 2013a Transition delay in a boundary layer flow using active control. *J. Fluid Mech.* **731** (9), 288–311.
- SEMERARO, O., PRALITS, J. O., ROWLEY, C. W. & HENNINGSON, D. S. 2013b Riccati-less approach for optimal control and estimation: an application to two-dimensional boundary layers. *J. Fluid Mech.* **731**, 394–417.
- SHAHINFAR, S., SATTARZADEH, S. S. & FRANSSON, J. H. M. 2014 Passive Boundary Layer Control of Oblique Disturbances by Finite-Amplitude Streaks. *J. Fluid Mech.* **749**, 1–36.
- SIMON, B. 2014 Private communication. TU Darmstadt.
- STURZEBECHER, D. & NITSCHKE, W. 2003 Active cancellation of Tollmien–Schlichting instabilities on a wing using multi-channel sensor actuator systems. *Intl J. Heat and Fluid Flow* **24**, 572–583.

Part II

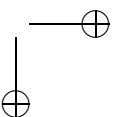
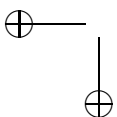
Papers

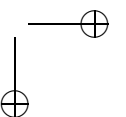
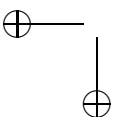
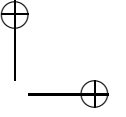
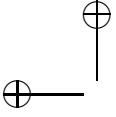




1

Paper 1





Adaptive and Model-Based Control Theory Applied to Convectively Unstable Flows

By **Nicolò Fabbiane**¹, **Onofrio Semeraro**², **Shervin Bagheri**¹
& **Dan S. Henningson**¹

¹ Linné FLOW Centre, KTH Mechanics, S-100 44 Stockholm, Sweden

² LadHyX, CNRS-École Polytechnique, 91128 Palaiseau, France

Applied Mechanics Reviews **66** (6): 060801

Research on active control for the delay of laminar-turbulent transition in boundary layers has made a significant progress in the last two decades, but the employed strategies have been many and dispersed. Using one framework, we review model-based techniques, such as linear-quadratic regulators, and model-free adaptive methods, such as least-mean square filters. The former are supported by a elegant and powerful theoretical basis, whereas the latter may provide a more practical approach in the presence of complex disturbance environments, that are difficult to model. We compare the methods with a particular focus on efficiency, practicability and robustness to uncertainties. Each step is exemplified on the one-dimensional linearized Kuramoto-Sivashinsky equation, that shows many similarities with the initial linear stages of the transition process of the flow over a flat plate. Also, the source code for the examples are provided.

1. Introduction

The key motivation in research on drag reduction is to develop new technology that will result in the design of vehicles with a significantly lower fuel consumption. The field is broad, ranging from passive methods, such as coating surfaces with materials that are super-hydrophobic or non-smooth (Bushnell & Moore 1991), to active methods, such as applying wall suction or using measurement-based closed-loop control (Kim & Bewley 2007). This work positions itself in the field of active control methods for skin-friction drag. In general, the mean skin friction of a turbulent boundary layer on a flat plate is an order of magnitude larger compared to a laminar boundary layer. One strategy to reduce skin-friction drag is thus to push the laminar-turbulent transition on a flat plate downstream (Schlichting & Gersten 2000). Different transition scenarios may occur in a boundary layer flows, depending on the intensity of the external disturbances acting on the flow, (Saric *et al.* 2002). Under low levels of free-stream turbulence and sufficiently far downstream, the transition process is initiated by the linear growth of small perturbations called Tollmien-Schlichting (TS) waves

(Schlichting & Gersten 2000). Eventually, these perturbations reach finite amplitudes and breakdown to smaller scales via nonlinear mechanisms (Schmid & Henningson 2001). However, in presence of stronger free-stream disturbances, the exponential growth of TS waves are bypassed and transition may be directly triggered by the algebraic growth of stream-wise elongated structures, called streaks (Saric *et al.* 2002). One may delay transition by damping the growth of TS waves and/or streaks, and thus postpone their nonlinear breakdown. This strategy enables the use of linear theory for control design.

Fluid dynamists noticed in the early 90’s, that many of the emerging concepts in hydrodynamic stability theory already existed in linear systems theory (Jovanovic & Bamieh 2005; Schmid 2007). For example, the analysis of a system forced by harmonic excitations is referred to as signalling problem by fluid dynamicists, while control theorists analyze the problem by constructing a Bode diagram, (Glad & Ljung 2000); similarly, a large transient growth of a fluid system corresponds to large norm of a transfer function and matrix with stable eigenvalues can be called either globally stable or Hurwitz, (Schmid & Henningson 2001; Huerre & Monkewitz 1990).

However, the systems theoretical approach had taken one step further, by “closing the loop”, i.e providing rigorous conditions and tools to modify the linear system at hand. It was realized by fluid dynamists that the extension of hydrodynamic stability theory to include tools and concepts from linear control theory was natural (Joshi *et al.* 1997; Bewley & Liu 1998; Cortelezzi *et al.* 1998). A long series of numerical investigations addressing the various aspects of closed-loop control of transitional (Högberg *et al.* 2003a; Chevalier *et al.* 2007a; Monokrousos *et al.* 2008) and turbulent flows (Lee *et al.* 2001; Högberg *et al.* 2003; Chevalier *et al.* 2006) followed in the wake of these initial contributions.

At the same time, research on active control for transition delay has been advanced from a more practical approach using system identification methods (Ljung 1999) and active wave-cancellation techniques (Elliott & Nelson 1993). Most work (but not all) is experimental, which due to feasibility constraints, has favoured an engineering and occasionally *ad hoc* methods. One of the first examples of this approach is the control of TS waves in the experiments by Milling (1981) using a wave-cancellation control; the propagating waves are cancelled by generating perturbations with opposite phase. This work was followed by number of successful experimental investigations (Jacobson & Reynolds 1998; Sturzebecher & Nitsche 2003; Rathnasingham & Breuer 2003; Lundell 2007) of transition delay using more sophisticated system identification techniques.

On the other hand, both numerical and experimental approaches have pushed forward flow control research, they have in a large extent evolved disconnected from each other; the systems control theoretical approach has provided very important insights into physical mechanisms and constraints that has to be addressed in order to design active control that is optimal and robust, but most work has stayed at a proof-of-concept level and have not yet been fully

implemented in practical applications. Although, there are exceptions (McKeon *et al.* 2013; Goldin *et al.* 2013), the majority of experimental active control has essentially suffered from the opposite; most controllers are developed directly in the experimental setting on a trial-and-error basis, with many tuning parameters, that have to be chosen for each particular set-up.

This review aims at presenting model-based and model-free techniques that are appropriate for the control of TS waves in a flat-plate boundary layer. We compare and link the two approaches using a linear model, that similar to the linearized Navier-Stokes equations, exhibits a large transient amplification behaviour and time delays. This presentation is unavoidably influenced by the authors background and previous work; complementary reviews on flow control can be found in Kim & Bewley (2007), Sipp *et al.* (2010) and Bagheri & Henningson (2011), where the linear approach is analyzed, and in the reviews by Bagheri *et al.* (2009c) and Sipp & Schmid (2013), focussed on the identification of reduced-order models for the linear control design. Finally, we refer to el Hak (1996), Bewley (2001) and Collis *et al.* (2004) for a broader prospective.

1.1. *The control problem*

Consider a steady uniform flow U_∞ over a thin flat plate of length L and infinite width. Inside the two-dimensional (2D) (Blasius) boundary layer that develops over the plate, we place a small localized disturbance (denoted by d in Figure 1) of simple Gaussian shape; the set-up is the same as in Bagheri *et al.* (2009b) and the simulation is performed using a spectral code (Chevalier *et al.* 2007). Figure 2 summarizes the spatio-temporal evolution of the disturbance. It shows a contour plot of the stream-wise component of the perturbation velocity at a wall normal position $Y = \delta^*(0)$, where $\delta^*(X)$ is the displacement thickness of the boundary layer. The temporal growth of this disturbance is determined by classical linear stability theory (i.e. eigenvalue analysis of the linearized Navier-Stokes equations). Such an analysis reveals that asymptotically a compact wave-packet emerges – a TS wave-packet – that grows in time at an exponential rate while travelling downstream at group velocity of approximately $U_\infty/3$. This disturbance behaviour is observed as long as the amplitude is below a critical value (usually a few percent of U_∞) (Schmid & Henningson 2001). Above the critical value, nonlinear effects have to be taken into account; they eventually result in a break down of the disturbance to smaller scales and finally to transition from a laminar to a turbulent flow (Schmid & Henningson 2001). However, the key point – that enables the use of linear theory for transition control – is that the disturbance may grow several orders of magnitude before it breaks down.

Using a spatially localized forcing (denoted by u in Figure 1) downstream of the disturbance, one may modify the conditions in order to reduce the amplitude of the wave-packet and thus delay the transition to turbulence. Physically this forcing is provided by devices called *actuators*. An example of an actuator is a loudspeaker that generates short pulses through a small orifice in the plate.

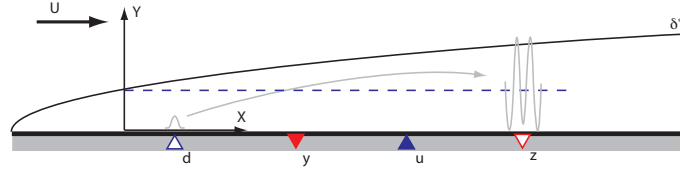


FIGURE 1. Scheme of a Blasius boundary-layer flow developing over a flat plate. A disturbance modelled by d grows exponentially while convected downstream. The actuator u is used to attenuate the disturbance before it triggers transition to turbulence; the actuation signal is computed based on the measurements provided by the sensor y . The output z , located downstream of the actuator, estimates the efficiency of the control action.

The volume of the loudspeaker and the shape of the orifice determines the type of actuation. Another example is plasma actuators, where a plasma arch is used to induce a forcing on the flow (Grundmann & Tropea 2008).

In closed-loop control, a sensor (denoted by y in Figure 1) is used to measure the disturbance that is meant to be cancelled by the actuator (u): based on these measurements one computes the actuator action in order to effectively reduce the amplitude of the perturbation. Examples of sensors include pressure measurements using a small microphone membrane mounted flush to the wall, velocity measurements using hot-wire anemometry near the wall or shear-stress measurements using thermal sensors (wall wires). Finally, we place a second sensor (denoted by z in Figure 1) downstream of the actuator to measure the amplitude of the perturbation after the actuator action. The minimization of this output signal may serve as an objective of our control design, but the measurements also provide a means to assess the performance of the controller.

Having introduced the inputs and outputs, the control problem can be formulated as the following: given the measurement $y(t)$, compute the modulation signal $u(t)$ in order to minimize a cost function based on $z(t)$. The system that when given the measurement $y(t)$, provides the control signal $u(t)$ is referred to as the *compensator*. The design of the compensator has to take into account competing aspects such as robustness, performance and practical feasibility.

The objective of this review is to guide the reader through the steps of compensator design process. We will exemplify the theory and the associated methods on a one-dimensional (1D) model based on the linearized Kuramoto-Sivashinsky (KS) equation (presented in §2). The model reproduces the most important stability properties of the flat-plate boundary layer, but it avoids the problem of high-dimensionality and thus the high numerical costs. In §3 full-information control problem is addressed via optimal control theory; linear

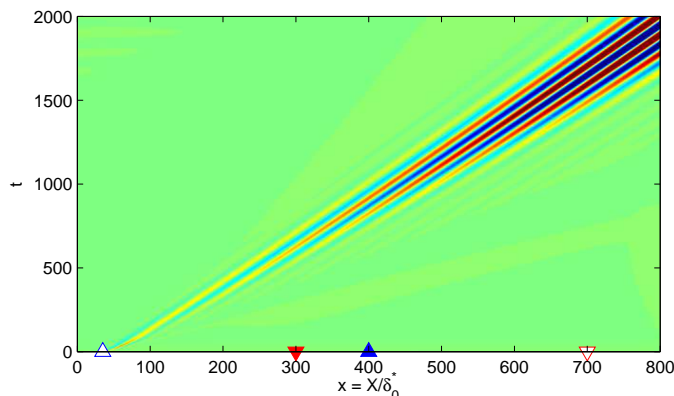


FIGURE 2. Response to a small, localized initial condition in a Blasius boundary-layer flow. A Tollmien-Schlichting wavepacket emerges and grows exponentially while propagating downstream. Contours of the streamwise component of the velocity are shown as a function of the streamwise direction (x) and time (t). The location along the normal-direction y is chosen in the vicinity of the wall.

quadratic regulator (LQR) and model-predictive controller (MPC) strategies are derived and compared. The disturbance estimation problem is addressed in §4, where classical Kalman estimation theory and least-mean-square techniques will be introduced and compared. The techniques of sections §3 and §4, will be combined in order to design the compensator in §3. This section also contains adaptive algorithms that enhance the robustness of the compensator. The review finalizes with a discussion §6 about some important features characterizing the control problem when applied to three-dimensional (3D) fluid flows and conclusions §7.

2. Framework

We first introduce our choice of model KS equation, inputs (actuators/disturbances) and sensors. This is followed by a presentation of concepts pertinent to our work, namely the state-space formulation (§2.4), transfer functions and finite-impulse response (§2.5), controllability and observability (§2.6), closed-loop system (§2.7) and robustness (§5). This chapter contains the mathematical ingredients that will be used in the following sections.

2.1. Kuramoto-Sivashinsky model

In this paper, we focus our attention on flows dominated by convection/advection, where disturbances have negligible upstream influence and are quickly swept downstream with the flow. We make use of a particular variant

36 *N. Fabbiane, O. Semeraro, S. Bagheri & D. S. Henningson*

of the KS equation to model a linear and convection-dominated flow. Originally, the KS equation was developed to describe the flame front flutter in laminar flames (Kuramoto & Tsuzuki 1976; Sivashinsky 1977). This model exhibits in its space-periodic form a spatio-temporal chaotic behaviour, with some similarities to turbulence (Manneville 1995). The standard KS equation reads

$$\frac{\partial \tilde{v}}{\partial \tilde{t}} + \tilde{v} \frac{\partial \tilde{v}}{\partial \tilde{x}} = -\eta \frac{\partial^2 \tilde{v}}{\partial \tilde{x}^2} - \mu \frac{\partial^4 \tilde{v}}{\partial \tilde{x}^4}, \quad (1)$$

where \tilde{t} is the time, $\tilde{x} \in [0, \tilde{L})$ the spatial coordinate and $\tilde{v} = \tilde{v}(\tilde{x}, \tilde{t})$ the velocity. The boundary conditions accompanying (1) are periodic in \tilde{x} . The second term on the left side in (1) is the nonlinear convection term, while on the right side two viscosity terms appear. The two latter terms may be associated to the production and dissipation of energy at different spatial scales. In particular, the second-order derivative term is related to the production of the energy via the variable η , called *anti-viscosity*, while the dissipation of the energy is connected to the fourth-order derivative term, multiplied by the *hyper-viscosity* μ (Cvitanović *et al.* 2012).

Equation (1) can be rewritten such that it is parametrized by a Reynolds-number-like coefficient. Introducing a reference length \tilde{l} and a reference velocity \tilde{V} , define the non-dimensional position x , velocity v and time t by

$$x = \frac{\tilde{x}}{\tilde{l}}, \quad v = \frac{\tilde{v}}{\tilde{V}}, \quad t = \frac{\tilde{V}}{\tilde{l}} \tilde{t}. \quad (2)$$

Applying the transformation to (1), the KS equation in dimensionless form becomes

$$\frac{\partial v}{\partial t} + v \frac{\partial v}{\partial x} = -\frac{1}{\mathcal{R}} \left(\mathcal{P} \frac{\partial^2 v}{\partial x^2} + \frac{\partial^4 v}{\partial x^4} \right), \quad (3)$$

where $x \in [0, L)$. The parameters \mathcal{R} and \mathcal{P} are defined as

$$\mathcal{R} = \frac{\tilde{V} \tilde{l}^3}{\mu}, \quad \mathcal{P} = \frac{\eta \tilde{l}^2}{\mu}, \quad (4)$$

where \mathcal{R} takes the role of the Reynolds number Re_{δ^*} , and \mathcal{P} regulates the balance between energy production and dissipation.

We assume that the system is sufficiently close to a steady solution $V(x) = V$. Then, it is possible to describe the dynamics of perturbations using the linearized KS equation. For the chosen parameters, the steady solution is stable, but an external perturbation may be amplified by an order-of-magnitude before it dies out (this requires non-periodic boundary conditions in the streamwise direction as we impose below). Introduce the perturbation $v'(x, t)$

$$v(x, t) = V + \epsilon v'(x, t), \quad (5)$$

where $\epsilon \ll 1$. By inserting this decomposition into (3) and neglecting the terms of order ϵ^2 and higher, the linearized KS equation is obtained

$$\frac{\partial v'}{\partial t} = -V \frac{\partial v'}{\partial x} - \frac{1}{\mathcal{R}} \left(\mathcal{P} \frac{\partial^2 v'}{\partial x^2} + \frac{\partial^4 v'}{\partial x^4} \right). \quad (6)$$

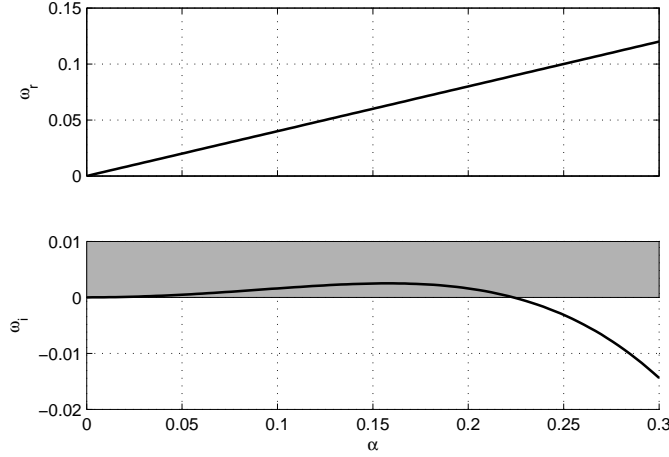


FIGURE 3. The real frequency ω_r and its imaginary part ω_i are shown as a function of the spatial frequency α , in (a) and (b), respectively. The relation among the spatial and temporal frequencies is given by the dispersion relation (8). Positive values of ω_i characterize unstable waves (grey region).

It is the convective and amplifying properties of this non-normal system that makes it a good model of the 2D Blasius boundary layer flow. Following Charru (2011), we analyze the stability properties of (6), by assuming travelling wave-like solutions:

$$v' = \hat{v} e^{i(\alpha x - \omega t)}, \quad (7)$$

where $\alpha \in \mathbb{R}$ and $\omega = \omega_r + i\omega_i \in \mathbb{C}$. Substituting (7) in (6), a dispersion relation between the spatial wave-number α and the temporal frequency ω is obtained

$$\omega = V\alpha + i \left(\frac{\mathcal{P}}{\mathcal{R}} \alpha^2 - \frac{1}{\mathcal{R}} \alpha^4 \right). \quad (8)$$

This relation is shown in Figure 3 for $\mathcal{R} = 0.25$, $\mathcal{P} = 0.05$ and $V = 0.4$. The parameters are chosen to closely model the Blasius boundary layer at $Re_{\delta^*} = 1000$. The imaginary part of the frequency ω_i is the exponential temporal growth rate of a wave with wave-number α . In (8) it can be observed that the term in α^2 (associated to the production parameter \mathcal{P}), is providing a positive contribution to ω_i , while the α^4 term (related to the dissipation parameter \mathcal{R}), has a stabilizing effect. The competition between these two terms determines stability of the considered wave. From Figure 3, it can be observed that for an interval of wave-numbers α , $\omega_i > 0$, i.e. the wave is unstable. The real part ω_r determines the phase speed of the wave in the x direction,

$$c \triangleq \frac{\omega_r}{\alpha} = V. \quad (9)$$

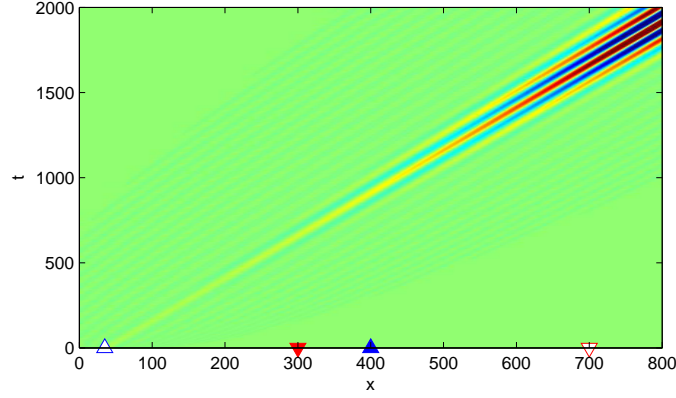


FIGURE 4. Response to a small, localized initial condition in a 1D KS flow (6) with $\mathcal{R} = 0.25$, $\mathcal{P} = 0.05$ and $V = 0.4$. The contours are shown as a function of the streamwise direction (x) and the time (t). The initial condition triggers a growing and travelling wave-packet, similar to the 2D boundary-layer flow shown in Figure 2. [`script00.m`].

Note that the phase speed c is independent of α , in contrast to the boundary-layer flow, which is dispersive (Schmid & Henningson 2001).

2.2. Outflow boundary condition

So far in our analysis we have assumed periodic boundary conditions for the KS equation. As we are interested in modelling the amplification of a propagating wave-packet near a stable steady solution (as observed in the case of boundary-layer flow), it is appropriate to change the boundary conditions to an outflow condition on the right side of the domain

$$\left. \frac{\partial^3 v'}{\partial x^3} \right|_{x=L} = 0, \quad \left. \frac{\partial v'}{\partial x} \right|_{x=L} = 0, \quad (10)$$

while on the left side of the domain, at the inlet, an unperturbed boundary condition is considered

$$v'|_{x=0} = 0, \quad \left. \frac{\partial v'}{\partial x} \right|_{x=0} = 0. \quad (11)$$

With an outflow boundary condition, a localized initial perturbation in the upstream region of the domain travels in the downstream direction while growing exponentially in amplitude until it leaves the domain. This is the signature of a convectively unstable flow. Note that this choice of boundary conditions is the main variant with respect to the original KS equation, characterized by periodic boundaries. Figure 4 shows the spatio-temporal response to a localized initial condition of KS equation with outflow boundary condition. The set of parameters \mathcal{R} , \mathcal{P} and V has been chosen to mimic the response of the 2D

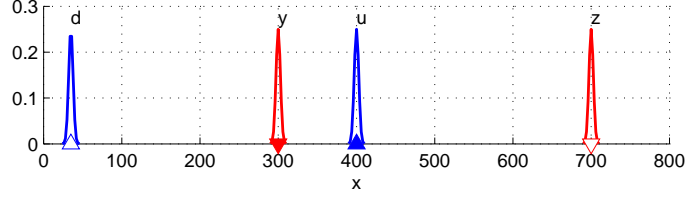


FIGURE 5. Spatial support of the inputs and outputs along the streamwise direction. All the elements are modelled as a Gaussian function in (14), with $\sigma_d = \sigma_u = \sigma_y = \sigma_z = 4$.

boundary-layer flow, shown in Figure 2. However, note that in the KS model the wave crests travel parallel to each other with the same speed of the wave-packet, whereas in the boundary layer, they travel faster than the wave-packet which they form. Indeed the system is not dispersive, i.e. the phase speed c equals the group speed c_g as shown by (9); conversely, as already noticed, the 2D BL is dispersive.

2.3. Introducing inputs and outputs

Having presented the dynamics of the linear system, we now proceed with a more systematic analysis of the inputs (actuators/disturbances) and sensor outputs described in §1.1. Consider the linearized KS equation in (6)

$$\frac{\partial v'}{\partial t} = -V \frac{\partial v'}{\partial x} - \frac{1}{\mathcal{R}} \left(\mathcal{P} \frac{\partial^2 v'}{\partial x^2} + \frac{\partial^4 v'}{\partial x^4} \right) + f'(x, t), \quad (12)$$

where the forcing term $f'(x, t)$ now appears on the right-hand side. This term is decomposed into two parts,

$$f'(x, t) = b_d(x) d(t) + b_u(x) u(t). \quad (13)$$

The temporal signal of the incoming external disturbance and of the actuator are denoted by $d(t)$ and $u(t)$, respectively, while the corresponding spatial distribution is described by b_d and b_u . In this work, the time-independent spatial distribution of the inputs is described by the Gaussian function,

$$g(x; \hat{x}, \sigma) = \frac{1}{\sigma} \exp \left[- \left(\frac{x - \hat{x}}{\sigma} \right)^2 \right]. \quad (14)$$

The scalar parameter σ determines the width of the Gaussian distribution, whereas \hat{x} determines the centre of the Gaussian. The two forcing distributions in (13) are

$$b_d(x) = g(x; \hat{x}_d, \sigma_d), \quad b_u(x) = g(x; \hat{x}_u, \sigma_u). \quad (15)$$

The disturbance d is positioned in the beginning of the domain at $\hat{x}_d = 35$, while the actuator u in the middle of the domain at $\hat{x}_u = 400$ (see Figure 5). In the presentation above, the particular shape $b_d(x)$ of the disturbance d is part of the modelling process. However, note that the introduction of the upstream

disturbance using a localized and well defined shape $b_d(x)$ is a model. In practice, due to the receptivity processes, the distribution and the appearance of the incoming disturbance is not known *a-priori*, and thus difficult to predict using – for instance – a low-order model.

A similar issue may arise for the model of the actuator $b_u(x)$, where the forcing distribution can even be time varying. For example the spatial force that a plasma actuator induces in the flow depends on the supplied voltage, e.g. modulated by the amplitude $u(t)$ (Grundmann & Tropea 2008). As we will discuss in the following sections, one may design a controller without knowing $b_d(x)$ and $b_u(x)$, but for the sake of presentation we may assume in this section, that such models exist.

By using (14) as integration weights, we define two outputs of the system as

$$y(t) = \int_0^L c_y(x) v'(x, t) dx + n(t), \quad (16)$$

$$z(t) = \int_0^L c_z(x) v'(x, t) dx, \quad (17)$$

where L is the length of the domain defined earlier and

$$c_y(x) = g(x; \hat{x}_y, \sigma_y), \quad c_z(x) = g(x; \hat{x}_z, \sigma_z).$$

The output y provides a measurement of an observable physical quantity – for example shear-stress, a velocity component or pressure near the wall – averaged with the Gaussian weight. In realistic conditions, this measured quantity is subject to some form of noise, that may arise from calibration drifting, truncation errors and/or incomplete cable shielding, etc. This is taken into account by the forcing term $n(t)$. It is often modelled as random noise with Gaussian distribution of zero-mean and variance α , and can be regarded as an input of the system. The second output $z(t)$, located far downstream, represents the *objective* of the controller: assuming that the flow has been already modified due to the action of the controller, this *controlled* output is the quantity that we aim to keep as small as possible.

In Figure 6, we show the response of our system to a Gaussian white noise in $d(t)$ with a unit variance, where all temporal frequencies are excited. Via the dispersion relation (8), each temporal frequency ω_r is related to a spatial frequency $\alpha = V \omega_r$. The input signal $d(t)$ is thus filtered by the system, where after a short transient, only the unstable spatial wavelengths are present in the state $\mathbf{v}(t)$, Figure 6(a), and the two output signals $y(t)$ and $z(t)$, Figure 6(c-d). The variance of the output $z(t)$ is higher than the variance of $y(t)$ by a factor 10, independently by the realization; this is because the wave-packets generated by d is growing in amplitude while convected downstream. We note that each realization will generate a different time evolution of the system but with the same statistical properties (black and grey lines in Figure 6(b-d)).

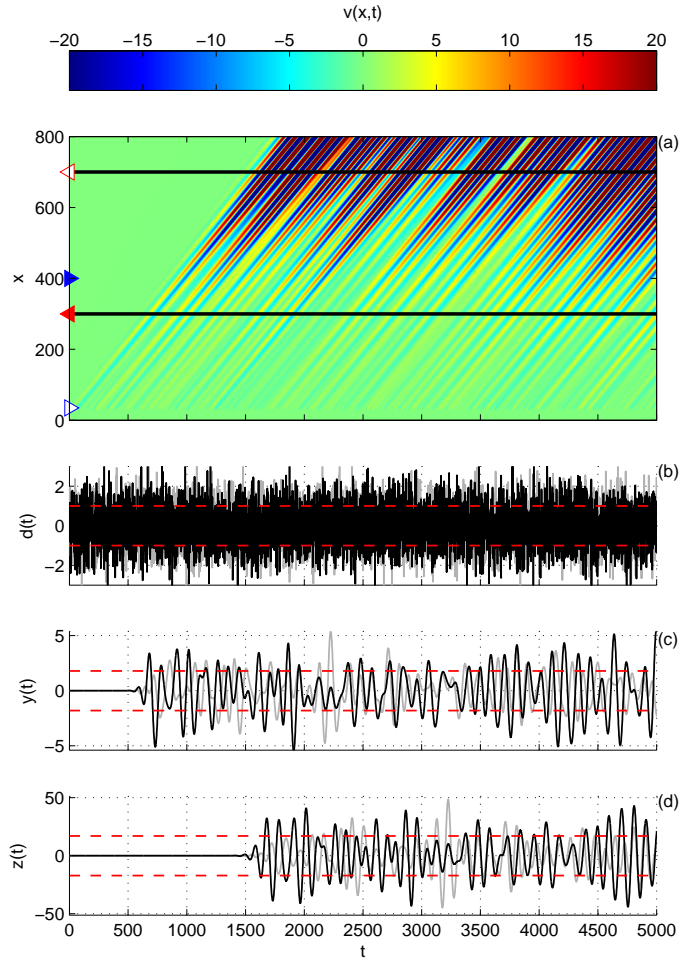


FIGURE 6. Top frame (a) shows the spatio-temporal response to white noise $d(t)$, (b). The velocity contours are shown as a function of the streamwise direction (x) and time (t). The signals $y(t)$ and $z(t)$ are shown for two different realizations (black and grey lines) in (c) and (d), respectively. Red dashed lines indicate the standard deviation of the signals. [script01.m]

2.4. State-space formulation

We discretize the spatial part of (12) by a finite-difference scheme. As further detailed in §7, the solution is approximated by

$$v'_i(t) = v'(x_i, t) \quad i = 1, 2, \dots, n_v$$

defined on the equispaced nodes $x_i = iL/n_v$, where $n_v = 400$. The spatial derivatives are approximated by a finite difference scheme based on five-points stencils. Boundary conditions in (11–10) are imposed using four ghost nodes $i = -1, 0$ and $i = n_v + 1, n_v + 2$. The resulting finite-dimensional state-space system (called *plant*) is

$$\dot{\mathbf{v}}(t) = \mathbf{A} \mathbf{v}(t) + \mathbf{B}_d d(t) + \mathbf{B}_u u(t), \quad (18)$$

$$y(t) = \mathbf{C}_y \mathbf{v}(t) + n(t), \quad (19)$$

$$z(t) = \mathbf{C}_z \mathbf{v}(t), \quad (20)$$

where $\mathbf{v} \in \mathbb{R}^{n_v}$ represents the nodal values v_i' . The output matrices \mathbf{C}_y and \mathbf{C}_z approximate the integrals in (16–17) via the trapezoidal rule, while the input matrices \mathbf{B}_d and \mathbf{B}_u are given by the evaluation of (15) at the nodes.

Some of the control algorithms that we will describe are preferably formulated in a time-discrete setting. The time-discrete variable corresponding to $a(t)$ is

$$a(k) = a(k\Delta t), \quad k = 1, 2, \dots \quad (21)$$

where Δt is the sampling time. Accordingly, the time-discrete state-space system is defined as:

$$\mathbf{v}(k+1) = \tilde{\mathbf{A}} \mathbf{v}(k) + \tilde{\mathbf{B}}_d d(k) + \tilde{\mathbf{B}}_u u(k), \quad (22)$$

$$y(k) = \tilde{\mathbf{C}}_y \mathbf{v}(k) + n(k), \quad (23)$$

$$z(k) = \tilde{\mathbf{C}}_z \mathbf{v}(k), \quad (24)$$

where $\tilde{\mathbf{A}} = \exp(\mathbf{A} \Delta t)$, $\tilde{\mathbf{B}} = \Delta t \mathbf{B}$ and $\tilde{\mathbf{C}} = \mathbf{C}$. For more details, the interested reader can refer to any control book, see e.g. (Glad & Ljung 2000).

2.5. Transfer functions and Finite-impulse responses

Given a measurement signal $y(t)$, our aim is to design an actuator signal $u(t)$. The relation between input and output signals is of primary importance. Since we are interested in the effect of the control signal $u(t)$ on the system, we assume the disturbance signal $d(t)$ to be zero. Thus, given an input signal $u(t)$ and a zero initial condition of the state, the output $z(t)$ of (18–20) may formally be written as

$$z(t) = \int_0^t \mathcal{P}_{zu}(t) u(t - \tau) d\tau, \quad (25)$$

where the kernel is defined by

$$\mathcal{P}_{zu}(t) \triangleq \mathbf{C}_z e^{\mathbf{A}t} \mathbf{B}_u, \quad t \geq 0. \quad (26)$$

Note that the description of the input-output (I/O) behaviour between $u(t)$ and $z(t)$ does not require the knowledge of the full dynamics of the state but only a representation of the impulse response between the input u and the output z , here represented by (26). A Laplace transform results in a transfer function

$$\hat{z}(s) = \hat{\mathcal{P}}_{zu}(s) \hat{u}(s) = (\mathbf{C}_z (s\mathbf{I} - \mathbf{A})^{-1} \mathbf{B}_u) \hat{u}(s)$$

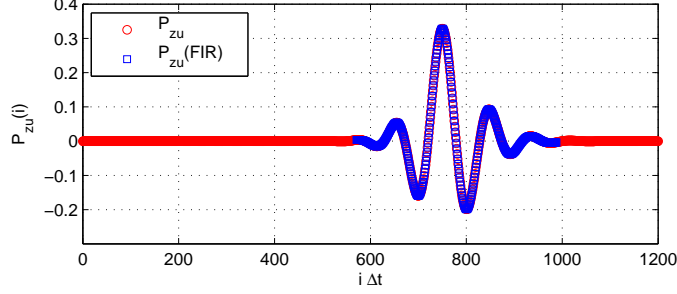


FIGURE 7. Time discrete impulse response (◦) between the input u to the output z ; due to the presence of strong time-delays in the system, a lag of $t \approx 550$ is observed. The relevant part of the kernel is reconstructed via a FIR filter (◻). [script02.m]

with $s \in \mathbb{C}$. Henceforth the *hat* on the transformed quantities is omitted since related by a linear transformation to the corresponding quantities in time-domain. One may formulate a similar expression for the other input-output relations, which for our case with three inputs and two outputs, induces 6 transfer functions, i.e.

$$\begin{bmatrix} z(s) \\ y(s) \end{bmatrix} = \begin{bmatrix} \mathcal{P}_{zd}(s) & \mathcal{P}_{zu}(s) & \mathcal{P}_{zn}(s) \\ \mathcal{P}_{yd}(s) & \mathcal{P}_{yu}(s) & \mathcal{P}_{yn}(s) \end{bmatrix} \begin{bmatrix} d(s) \\ u(s) \\ n(s) \end{bmatrix}. \quad (27)$$

I/O relations similar to (25) can be found for the time-discrete system. The response $z(k)$ of the system (with $\mathbf{v}_0 = 0$) to an input $u(k)$ is

$$z(k) = \sum_{i=1}^k \tilde{\mathcal{P}}_{zu}(i) u(k-i), \quad (28)$$

where

$$\tilde{\mathcal{P}}_{zu}(k) \triangleq \tilde{\mathbf{C}}_z \tilde{\mathbf{A}}^{k-1} \tilde{\mathbf{B}}_u, \quad k = 1, 2, \dots \quad (29)$$

This procedure is usually referred to as *z-transform*; for more details, we refer to Glad & Ljung (2000) and Skogestad & Postlethwaite (2005). In the limit of $k \rightarrow \infty$, it is possible to truncate (28), since the propagating wave-packet that is generated by an impulse in u will be detected by the output z after a time-delay (this can be observed in Figure 7, where the impulse response is depicted). Thus, $\tilde{\mathcal{P}}_{zu}(i)$ is non-zero only in a short time interval and one may truncate the sum to a finite number of time steps, $N_{zu,f}$. Due to the strong time-delay, the initial part of the sum is also zero and the lower limit of the sum can start from $N_{zu,i}$. This results in a sum

$$z(k) \approx \sum_{i=N_{zu,i}}^{N_{zu,f}} \tilde{\mathcal{P}}_{zu}(i) u(k-i), \quad (30)$$

which is called the Finite Impulse Response (FIR), Aström & Wittenmark (1995). Note that the presence of time delays in the system is a limiting factor of the control performance. In general, a disturbance with a time scale smaller than the time delay that affects the system is difficult to control (Glad & Ljung 2000). In particular, while the compensator could still be able to damp those disturbances, it may lack robustness, §5.

2.6. Controllability and observability

The choice of sensors and actuators is particular relevant for the control design; indeed, the measurement of the sensor y enables to compute the control signal $u(t)$, that feeds the actuator. Thus, it is important to know: (i) if the system can be affected by the actuator u ; (ii) if the system can be detected by the sensor y . In other words, we aim at identify the states of the system that are *controllable* and/or *observable*. These two properties of the I/O system are referred to as *observability* and *controllability* (Glad & Ljung 2000; Bagheri *et al.* 2009c) and can be analyzed introducing the corresponding Gramians \mathbf{G}_o and \mathbf{G}_c

$$\mathbf{G}_o \triangleq \int_0^\infty e^{\mathbf{A}^H t} \mathbf{C}^H \mathbf{C} e^{\mathbf{A} t} dt, \quad (31)$$

$$\mathbf{G}_c \triangleq \int_0^\infty e^{\mathbf{A} t} \mathbf{B} \mathbf{B}^H e^{\mathbf{A}^H t} dt. \quad (32)$$

By construction, the Gramians ($\mathbf{G}_o, \mathbf{G}_c$) are positive semi-definite matrices in $\mathbb{R}^{n_v \times n_v}$ and can be computed for each or all the outputs/inputs. It can be proved that the two Gramians are solutions of the Lyapunov equations (Glad & Ljung 2000)

$$\mathbf{A}^H \mathbf{G}_o + \mathbf{G}_o \mathbf{A} + \mathbf{C}^H \mathbf{C} = \mathbf{0}, \quad (33)$$

$$\mathbf{A} \mathbf{G}_c + \mathbf{G}_c \mathbf{A}^H + \mathbf{B} \mathbf{B}^H = \mathbf{0}. \quad (34)$$

The spatial information related to the Gramians can be analyzed by diagonalizing them; the corresponding decompositions allow to identify and rank the most controllable/observable structures (Bagheri *et al.* 2009c). On the other hand, for systems characterized by a small number of degrees of freedom, it is possible to directly identify the regions where the flow is observable and/or controllable. Figure 8 shows the controllability Gramian related to the actuator u ($\mathbf{G}_{c,u}$) and the observability Gramian related to the sensor y ($\mathbf{G}_{o,y}$) for our system. The region downstream of the actuator is influenced by its action, due to the strong convection of the flow. The observability Gramian $\mathbf{G}_{o,y}$ indicates the region where a propagating perturbation can be observed by the sensor y . Note that the two regions do not overlap, thus wave-packets generated at the location u are not detected by a sensor y , when is placed upstream of the actuator. This feature has important consequences on the closed-loop analysis, as introduced in the next section.

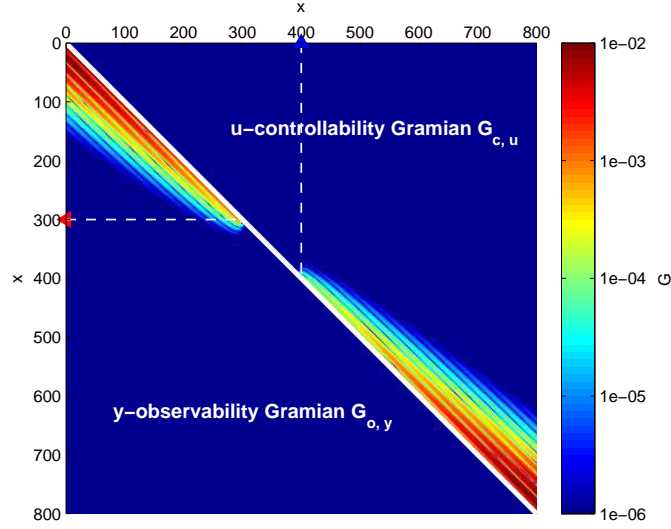


FIGURE 8. Controllability ($\mathbf{G}_{c,u}$) and observability ($\mathbf{G}_{o,y}$) Gramians, normalized by their trace; the absolute values are reported in logarithmic scale as a function of the streamwise direction (x). Due to the symmetry, only the upper/lower triangular part of each Gramian is shown. [script03.m]

2.7. Closed-loop system

The aim of the control design is to identify a second linear system \mathcal{K}_{uy} , called *compensator*, that provides a mapping between the measurements $y(t)$ and the control-input $u(t)$, i.e.

$$u(t) = \int_0^\infty \mathcal{K}_{uy}(\tau) y(t - \tau) d\tau$$

The chosen compensator is also called *output feedback controller* (Doyle *et al.* 1989; Zhou *et al.* 2002). This definition underlines the dependency of the control input $u(t)$ from the measurements $y(t)$. By considering the relation in frequency domain and inserting it into the plant (27), the *closed-loop* system between $d(s)$ and $z(s)$ is obtained in the form,

$$z(s) = \left[\mathcal{P}_{zd}(s) + \frac{\mathcal{P}_{zu}(s) \mathcal{K}_{uy}(s) \mathcal{P}_{yd}(s)}{1 - \mathcal{P}_{yu}(s) \mathcal{K}_{uy}(s)} \right] d(s). \quad (35)$$

By choosing an appropriate $\mathcal{K}_{uy}(s)$, we may modify the system dynamics. The graphical representation of the closed-loop system is shown in Figure 9. The transfer function $\mathcal{P}_{yu}(s)$ describes the signal dynamics from the actuator u to the sensor y . By definition, a feedback configuration is obtained when $\mathcal{P}_{yu}(s) \neq 0$, i.e. when the sensor can measure the effect of the actuation.

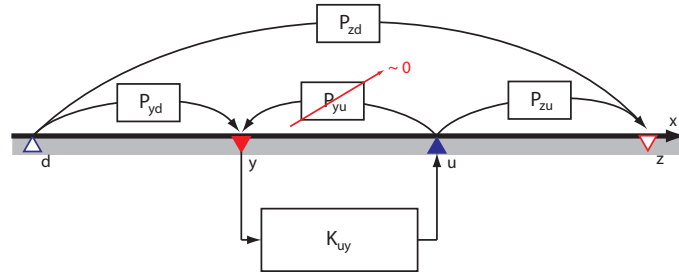


FIGURE 9. Schematic figure showing the 5 transfer functions defining the closed-loop system (35). The transfer functions \mathcal{P}_{yd} , \mathcal{P}_{zd} describe the input/output behaviour between the disturbance d and the outputs y and z , respectively; \mathcal{P}_{yu} and \mathcal{P}_{zu} relate the actuator u to the two outputs y and z , respectively, while \mathcal{K}_{uy} is the compensator transfer-function. Because of the convectively unstable nature of the flow, \mathcal{P}_{yu} is negligible for the chosen sensor/actuator locations; thus it does not allow any feedback.

On the other hand, if $\mathcal{P}_{yu}(s)$ is zero (or very small), the closed-loop system reduces to a disturbance feedforward configuration (Doyle *et al.* 1989; Zhou *et al.* 2002). In this special case, from the dynamical point of view such a system behaves as an open-loop system despite the closed-loop design (Skogestad & Postlethwaite 2005). Due to this inherent ambivalence within the framework of the output feedback control, sometimes the definition of *reactive control* is used for indicating all the cases where the control signal is computed based on measurements of the system; thus, the definition of closed-loop system more properly applies to a system where the reactive controller is characterized by feedback (el Hak 2007).

In a convection-dominated system, the sensor should be placed upstream of the actuator, in order to detect the upcoming wave-packet before it reaches the actuator (see also Figure 8); if it is placed downstream, the actuator has no possibility to influence the propagating disturbance once it has reached the sensor. Figure 10 shows the state and signal responses of the KS system to impulse in u , where it is clear that the actuator’s action is not detected by the sensor y , in practice $\mathcal{P}_{yu}(s) \approx 0$. Note that no assumptions about the compensator has been made; the feedback or feedforward setting is determined by the choice of sensor and actuator placement.

2.8. Robustness

In practice, model uncertainties are unavoidable and it is important to estimate how much the error arising from the mismatch between the physical system and the model affects the stability and performance of the closed-loop system. In

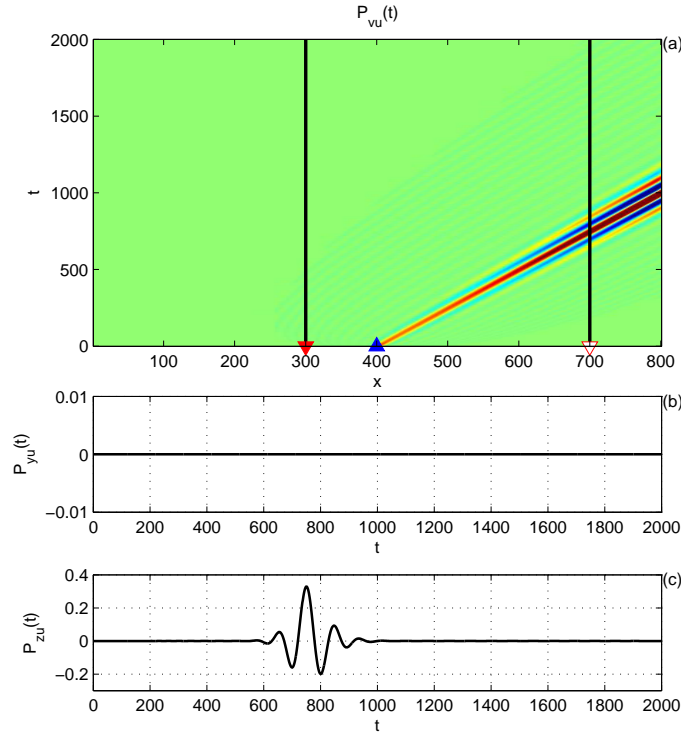


FIGURE 10. The disturbance generated by the impulse response of the system at the actuator location u in (a) is shown as a function of the streamwise direction (x) and time (t). The wave-packet is detected only by the output z (c); due to the convective nature of the flow, the sensor placed upstream of the actuator can not detect the propagating disturbance, and the resulting signal is practically null (b). [script02.m]

general, one wishes to have a controller that does not amplify un-modelled errors over a range of off-design conditions: a robustness analysis aims at identify this range. A useful quantity in this context, is the sensitivity transfer function, which is defined as the denominator in the second term on the right-hand side of (35), i.e.

$$\mathcal{S}(s) = \frac{1}{1 - \mathcal{P}_{yu}(s)\mathcal{K}_{uy}(s)}. \quad (36)$$

Robustness can be quantified as the infinity norm of $\mathcal{S}(s)$. Good stability margins are guaranteed when this norm is bounded, typically $\|\mathcal{S}\|_\infty < 2.0$, see Skogestad & Postlethwaite (2005). A second measure is the phase margin, that represents the maximum amount of allowable phase error before the instability of the closed-loop occurs. Indeed, the gain margin and the phase margin are

the upper limit of amplification and phase error, respectively, that guarantee marginal stability of the closed-loop system.

Note that the internal stability functions are characterized by a proper dynamics. In the *loop-shaping* approach, the controller is designed by shaping the behaviour of the internal transfer function (Skogestad & Postlethwaite 2005). Unfortunately, this methodology is difficult to be applied in complex system. A systematic approach for the robust design is represented by the optimal, robust \mathcal{H}_∞ (see (Zhou *et al.* 2002)), where the sensitivity margins can be optimized. A more computationally demanding alternative is represented by the controllers based on numerical optimization running on-line, such as the model-predictive control (MPC) (§3.2) or adaptive controllers (§5.4).

Thus, feedback controllers may be designed to have small sensitivity. In that regard robustness is a non-issue in a pure feedforward configuration; indeed, $\mathcal{P}_{yu}(s) \approx 0$ and $\|\mathcal{S}\|_\infty \approx 1$. However, a feedforward controller is highly affected by unknown disturbances and model uncertainty, that drastically reduce the overall performance of the device. Moreover, a feedforward controller is not capable in modifying the dynamics of an unstable plant; thus, feedback controllers are required for globally unstable flows (Sipp & Schmid 2013).

The studies performed by Julliet *et al.* (2013) and Belson *et al.* (2013) show that in convectively unstable flows a feedback configuration allows the possibility of robust-control design but it does not guarantee *optimal* performances in terms of amplitude reduction. In this review, we adopt a feedforward configuration in order to achieve optimal performances. As we will show in §5.4, robustness may be addressed to some extent using adaptive control techniques.

3. Model-based control

In this section, we assume the full knowledge of the state $\mathbf{v}(t)$ for the computation of the control signal $u(t)$. This signal is fed back into the system in order to minimize the energy of the output $z(t)$. For linear systems, it is possible to identify a *feedback gain* $\mathbf{K}(t)$, relating the control signal to the state, i.e.

$$u(t) = \mathbf{K}(t)\mathbf{v}(t). \tag{37}$$

The aim of the section is to compare and link the classical LQR problem (Lewis & Syrmos 1995) to the more general MPC approach (Bewley *et al.* 2001; Kim & Bewley 2007). In the former approach, one assumes an infinite time horizon ($t \rightarrow \infty$), allowing the computation of the feedback gain by solving a Riccati equation (see §3.1.1). In the latter approach, the optimization is performed with a final time T that is receding, i.e. it slides forward in time as the system evolves. In §3.2.1, we introduce this technique for the control of a linear system with constraints on the actuator signal, while in §3.2.3 the close connection between the unconstrained MPC and the LQR is shown. Finally, note that the framework introduced in this section makes use of a system’s model. Model-free methods based on adaptive strategies are introduced in §3.

3.1. Optimal control

The aim of the controller is to compute a control signal $u(t)$ in order to minimize the norm of the fictitious output

$$\mathbf{z}'(t) = \begin{bmatrix} z(t) \\ u(t) \end{bmatrix} = \begin{bmatrix} \mathbf{C}_z \\ \mathbf{0} \end{bmatrix} \mathbf{v}(t) + \begin{bmatrix} 0 \\ 1 \end{bmatrix} u(t), \quad (38)$$

where now the control signal is also included. We define a *cost function* of the system

$$\mathcal{L}(\mathbf{v}(u), u) = \frac{1}{2} \int_0^T \begin{bmatrix} z \\ u \end{bmatrix}^H \begin{bmatrix} w_z & 0 \\ 0 & w_u \end{bmatrix} \begin{bmatrix} z \\ u \end{bmatrix} dt. \quad (39)$$

This cost function is quadratic and includes the constant matrices $w_z \geq 0$ and $w_u > 0$. The matrix w_z is used to normalize the cost output, specially when multiple $z(t)$ are used, while the weight w_u determines the amount of penalty on control effort (Lewis & Syrmos 1995). Using (38), (39) is rewritten as

$$\begin{aligned} \mathcal{L}(\mathbf{v}(u), u) &= \frac{1}{2} \int_0^T (\mathbf{v}^H (\mathbf{C}_z^H w_z \mathbf{C}_z) \mathbf{v} + u^H w_u u) dt = \\ &= \frac{1}{2} \int_0^T (\mathbf{v}^H \mathbf{W}_v \mathbf{v} + u^H w_u u) dt \end{aligned} \quad (40)$$

where $\mathbf{W}_v = \mathbf{C}_z^H w_z \mathbf{C}_z$. We recall from §2.3 that the sensor \mathbf{C}_z is placed far downstream in the domain, so we are minimizing the energy in localized region. We seek a control signal $u(t)$ that minimizes the cost function $\mathcal{L}(\mathbf{v}(u), u)$ in some time interval $t \in [0, T]$ subject to the dynamic constraint

$$\dot{\mathbf{v}}(t) = \mathbf{A} \mathbf{v}(t) + \mathbf{B}_u u(t). \quad (41)$$

Note that we do not consider the disturbance $d(t)$ for the solution of the optimal control problem. In a variational approach, one defines a Lagrangian

$$\begin{aligned} \tilde{\mathcal{L}}(\mathbf{v}(u), u) &= \frac{1}{2} \int_0^T (\mathbf{v}^H \mathbf{W}_v \mathbf{v} + u^H w_u u) dt + \\ &+ \int_0^T \mathbf{p}^H (\dot{\mathbf{v}} - \mathbf{A} \mathbf{v} - \mathbf{B}_u u) dt, \end{aligned} \quad (42)$$

where the term $\mathbf{p}(t)$ acts as a Lagrangian multiplier (Gunzburger 2003), also called the adjoint state. The expression in the last term is obtained via integration by parts. Instead of minimizing \mathcal{L} with a constraint (41) one may minimize $\tilde{\mathcal{L}}$ without any constraints.

The dynamics of the adjoint state $\mathbf{p}(t)$ is obtained by requiring $\partial \tilde{\mathcal{L}} / \partial \mathbf{v} = \mathbf{0}$, which leads to

$$\begin{aligned} -\dot{\mathbf{p}}(t) &= \mathbf{A}^H \mathbf{p}(t) + \mathbf{W}_v \mathbf{v}(t), \\ \mathbf{0} &= \mathbf{p}(T). \end{aligned} \quad (43)$$

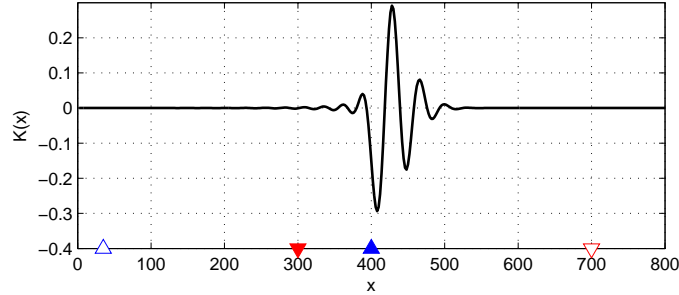


FIGURE 11. Control gain \mathbf{K} computed using the LQR technique for $w_z = 1$ and $w_u = 1$, (see §3.1.1). [script04.m]

The adjoint field $\mathbf{p}(t)$ is computed by marching backwards in time this equation, from $t = T$ to $t = 0$. The optimality condition is obtained by the gradient

$$\frac{\partial \tilde{\mathcal{L}}}{\partial u} = \mathbf{B}_u^H \mathbf{p} + w_u u. \quad (44)$$

The resulting equations' system can be solved iteratively as follows:

1. The state $\mathbf{v}(t)$ is computed by marching forward in time (41) in $t \in [0, T]$. At the first iteration step, $k = 1$, an initial guess is taken for the control signal $u(t)$.
2. The adjoint state $\mathbf{p}(t)$ is evaluated marching (43) backward in time, from $t = T$ to $t = 0$. The initial condition $\mathbf{p}(T)$ is taken to be zero.
3. Once the adjoint state $\mathbf{p}(t)$ is available, it is possible to compute the gradient via (44) and apply it for the update of the control signal using a gradient-based method; one may for example apply directly the negative gradient $\Delta u_k = -\frac{\partial \tilde{\mathcal{L}}_k}{\partial u}$, such that the update of the control signal at each iteration is given by

$$u_{k+1} = u_k + \mu_k \Delta u_k.$$

The scalar-valued parameter μ_k is the step-length for the optimization, properly chosen by applying backtracking or exact line search (Boyd & Vandenberghe 2004). An alternative choice to the steepest descent algorithm is a conjugate gradient method (Press *et al.* 2007).

The iteration stops when the difference of the cost function \mathcal{L} estimated at two successive iteration steps is below a certain tolerance or the gradient value $\partial \tilde{\mathcal{L}} / \partial u \rightarrow 0$. We refer to Gunzburger (2003) for more details and to Corbett & Bottaro (2001) for an application in flow optimization.

3.1.1. Linear-quadratic regulator (LQR)

The framework outlined in the previous section is rather general and it can be applied for the computation of the control signal $u(t)$ also when nonlinear systems or receding finite-time horizons are considered. However, a drawback

of the procedure is the necessity of running an optimization on-line, next to the main flow simulation/experiment. When a linear time-invariant system is considered, a classic way to proceed is to directly use the optimal condition (44) in order to identify the optimal control signal $u(t)$

$$u(t) = -w_u^{-1} \mathbf{B}_u^H \mathbf{p}(t). \quad (45)$$

The computed control signal $u(t)$ is *optimal* as it minimizes the cost function $\mathcal{L}(\mathbf{v}(u), u)$ previously defined. Assuming a linear relation between the adjoint state and the direct state, $\mathbf{p}(t) = \mathbf{X}(t)\mathbf{v}(t)$, the feedback gain is given by

$$\mathbf{K}(t) = -w_u^{-1} \mathbf{B}_u^H \mathbf{X}(t). \quad (46)$$

It can be shown that the matrix $\mathbf{X}(t)$ is the solution of a differential Riccati equation (Lewis & Syrmos 1995). When \mathbf{A} is stable, $\mathbf{X}(t)$ reaches a steady state as $T \rightarrow \infty$, which is a solution of the algebraic Riccati equation

$$\mathbf{0} = \mathbf{A}^H \mathbf{X} + \mathbf{X} \mathbf{A} - \mathbf{X} \mathbf{B}_u w_u^{-1} \mathbf{B}_u^H \mathbf{X} + \mathbf{W}_v. \quad (47)$$

The advantage of this procedure is that \mathbf{K} is a constant and needs to be computed only once. The spatial distribution of the control gain \mathbf{K} is shown in Figure 11 for the KS system analysed in §2, where the actuator is located at $x = 400$ and the objective output at $x = 700$. From Figure 11 one can see that the gain is a compact structure between the elements \mathbf{B}_u and \mathbf{C}_z . The control gain is independent on the shape of external disturbance \mathbf{B}_d .

For low-dimensional systems ($n_v < 10^3$), solvers for the Riccati equations (47) are available in standard software packages (Arnold & Laub 1984). For larger systems $n_v > 10^3$, as the ones investigated in flow control, direct methods are not computationally feasible. Indeed, the solution of (47) is a full matrix, whose storage requirement is at least of order $O(n_v^2)$. The computational complexity is of order $O(n_v^3)$ regardless the structure of the system matrix \mathbf{A} (Benner *et al.* 2008). Alternative techniques include the Chandrasekhar method (Banks & Ito 1991), Krylov subspace methods (Benner 2004), decentralized techniques based on Fourier transforms for spatially invariant system (Bamieh *et al.* 2002; Högberg & Bewley 2000; Högberg *et al.* 2003a) and finally iterative algorithms (Akhtar *et al.* 2010; Martensson & Rantzer 2011; Pralits & Luchini 2010; Semeraro *et al.* 2013). Yet, a different approach consists of reducing n_v before the control techniques are applied. In practice, we seek a low-order surrogate system, typically of $O(n_{v,r}) \approx 10 - 10^2$, whose dynamics reproduces the main features of the original, full-order system. Once the low-order model is identified, the controller is designed and fed into the full-order system; such an approach enables the application of a controller next to real experiments, using small (and fast) real-time computations. The *model-reduction* problem is an important aspect of control design for flow control; we refer to §6 for a brief overview.

52 *N. Fabbiane, O. Semeraro, S. Bagheri & D. S. Henningson*

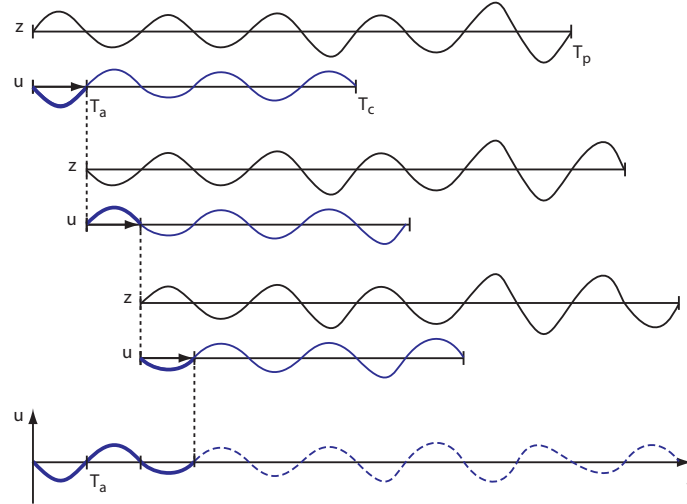


FIGURE 12. MPC strategy: the controller is computed over a finite time-horizon T_c , based on the a predicted time-horizon T_p . Once the solution is available, the control signal is applied on a shorter time windows T_a . In the successive step, the time-window slides forward in time and the optimization is performed again, starting from a new initial condition at $t = T_a$. The procedures is iterated while proceeding forward in time.

3.2. Model-predictive control (MPC)

MPC controllers make use of an identified model to predict the behaviour of the system over a finite-time horizon (see Garcia *et al.* (1989), Qin & Badgwell (2003) and Noack *et al.* (2011) for an overview on the technique). In contrast with the optimal controllers presented in the previous section, the iterative procedure is characterized by a receding finite horizon of optimization. This strategy is illustrated in Figure 12; at time t_0 , a control signal is computed for a short window in time $[t_0, t_0 + T_c]$ by minimising a cost function (not necessarily quadratic); T_c is the final time of optimization for the control problem. The minimization is performed on-line, based on the prediction of the future trajectories emanating from the current state at t_0 over a window of time $[t_0, t_0 + T_p]$, such that $T_p \geq T_c$. In other words, the control signal is computed over an horizon T_c in order to minimize the predicted deviations from the reference trajectory evaluated on a (generally) longer time of prediction T_p . Once the calculation is performed, only the first step T_a is actually used for controlling the system. After this step, the plant is sampled again and the procedure is repeated at time $t = t_0 + T_a$, starting from the new initial state.

The MPC approach is applicable to nonlinear models as well as all nonlinear constraints (for example an upper maximum amplitude for the actuator signals). We present an example of the latter case in the following section.

3.2.1. MPC for linear systems with constraints

Although it is possible to define MPC in continuous-time formulation (see for instance (Garcia *et al.* 1989), (Bewley *et al.* 2001)), we make use of the more convenient discrete-time formulation. Let $M = T_p/\Delta t$ and $N = T_c/\Delta t$, where the parameter Δt is the sampling time. Since $T_p \geq T_c$, we have $M \geq N$. Augmenting the expression (28) with a term representing an initial state $\mathbf{v}(k)$ at time k , we get

$$\begin{aligned} z(k+j|k) &= \tilde{\mathbf{C}}_z \tilde{\mathbf{A}}^j \mathbf{v}(k) + \sum_{i=1}^{\min(j,N)} \tilde{\mathbf{C}}_z \tilde{\mathbf{A}}^{i-1} \tilde{\mathbf{B}}_u u(k+j-i) = \\ &= \tilde{\mathcal{P}}_{z\mathbf{v}}(j) \mathbf{v}(k) + \sum_{i=1}^{\min(j,N)} \tilde{\mathcal{P}}_{zu}(i) u(k+j-i), \end{aligned} \quad (48)$$

where $j = 1, 2, \dots, M$. The state equation can be written in matrix form by recursive iteration, resulting in the matrix-relation

$$\mathbf{z}_p(k) = \mathbf{P}_{z\mathbf{v}} \mathbf{v}(k) + \mathbf{P}_{z\mathbf{u}} \mathbf{u}_p(k). \quad (49)$$

The matrix $\mathbf{P}_{z\mathbf{v}}$ appearing in (49) is the observability matrix of the discrete-time system

$$\mathbf{P}_{z\mathbf{v}} = \begin{bmatrix} \tilde{\mathcal{P}}_{z\mathbf{v}}(1) \\ \tilde{\mathcal{P}}_{z\mathbf{v}}(2) \\ \vdots \\ \tilde{\mathcal{P}}_{z\mathbf{v}}(M) \end{bmatrix} = \begin{bmatrix} \tilde{\mathbf{C}}_z \tilde{\mathbf{A}} \\ \tilde{\mathbf{C}}_z \tilde{\mathbf{A}}^2 \\ \vdots \\ \tilde{\mathbf{C}}_z \tilde{\mathbf{A}}^M \end{bmatrix}, \quad (50)$$

while the matrix $\mathbf{P}_{z\mathbf{u}}$, related to the convolution operator, reads

$$\mathbf{P}_{z\mathbf{u}} = \begin{bmatrix} \tilde{\mathcal{P}}_{zu}(1) \\ \tilde{\mathcal{P}}_{zu}(2) & \tilde{\mathcal{P}}_{zu}(1) \\ \vdots & \vdots & \ddots \\ \tilde{\mathcal{P}}_{zu}(N) & \tilde{\mathcal{P}}_{zu}(N-1) & \cdots & \tilde{\mathcal{P}}_{zu}(1) \\ \vdots & \vdots & & \vdots \\ \tilde{\mathcal{P}}_{zu}(M) & \tilde{\mathcal{P}}_{zu}(M-1) & \cdots & \tilde{\mathcal{P}}_{zu}(M-N+1) \end{bmatrix} = \begin{bmatrix} \tilde{\mathbf{C}}_z \tilde{\mathbf{B}}_u & & & \\ \tilde{\mathbf{C}}_z \tilde{\mathbf{A}} \tilde{\mathbf{B}}_u & \tilde{\mathbf{C}}_z \tilde{\mathbf{B}}_u & & \\ \vdots & \vdots & \ddots & \\ \tilde{\mathbf{C}}_z \tilde{\mathbf{A}}^{N-1} \tilde{\mathbf{B}}_u & \tilde{\mathbf{C}}_z \tilde{\mathbf{A}}^{N-2} \tilde{\mathbf{B}}_u & \cdots & \tilde{\mathbf{C}}_z \tilde{\mathbf{B}}_u \\ \vdots & \vdots & & \vdots \\ \tilde{\mathbf{C}}_z \tilde{\mathbf{A}}^{M-1} \tilde{\mathbf{B}}_u & \tilde{\mathbf{C}}_z \tilde{\mathbf{A}}^{M-2} \tilde{\mathbf{B}}_u & \cdots & \tilde{\mathbf{C}}_z \tilde{\mathbf{A}}^{M-N} \tilde{\mathbf{B}}_u \end{bmatrix}. \quad (51)$$

In literature, the matrix $\mathbf{P}_{\mathbf{z}\mathbf{u}}$ is also referred to as dynamic matrix, because it takes into account the current and future input changes of the system. Note that the entries of the observability matrix (50) are directly obtained from the model realization, while the entries of the dynamic matrix (51) are represented by the time-discrete impulse response between the actuator u and the sensor z . The input vector $\mathbf{z}_{\mathbf{p}}(k)$ and output vector $\mathbf{u}_{\mathbf{p}}(k)$ are defined collecting the corresponding time-signals at each discrete step

$$\mathbf{z}_{\mathbf{p}}(k) = \begin{bmatrix} z(k+1|k) \\ z(k+2|k) \\ \vdots \\ z(k+M|k) \end{bmatrix}, \quad \mathbf{u}_{\mathbf{p}}(k) = \begin{bmatrix} u(k|k) \\ u(k+1|k) \\ \vdots \\ u(k+N-1|k) \end{bmatrix}. \quad (52)$$

Thus, the matrix relation (49) provides a linear relation between the state $\mathbf{v}(k)$ and the output $\mathbf{z}_{\mathbf{p}}(k)$ when the system is forced by the control input $\mathbf{u}_{\mathbf{p}}(k)$. The evaluation of the future output vector $\mathbf{z}_{\mathbf{p}}(k)$ represents the *prediction* step of the procedure; indeed, assuming that the control signal contained in the vector $\mathbf{u}_{\mathbf{p}}(k)$ is known, we aim at computing the future output $\mathbf{z}_{\mathbf{p}}(k)$, related to the trajectory emanating from the initial condition $\mathbf{v}(k)$.

By following the same rationale already adopted in the optimal control problem, a cost function $\mathcal{L}(k)$ that minimizes the output $z(t)$ while limiting the control expense is defined,

$$\begin{aligned} \mathcal{L}(k) &= \sum_{i=1}^M z^H(k+i|k) w_z z(k+i|k) \\ &\quad + \sum_{i=0}^{N-1} u^H(k+i|k) w_u u(k+i|k) = \\ &= \mathbf{z}_{\mathbf{p}}(k)^H \mathbf{W}_{\mathbf{z}} \mathbf{z}_{\mathbf{p}}(k) + \mathbf{u}_{\mathbf{p}}(k)^H \mathbf{W}_{\mathbf{u}} \mathbf{u}_{\mathbf{p}}(k). \end{aligned} \quad (53)$$

The parameters $\mathbf{W}_{\mathbf{z}}$ and $\mathbf{W}_{\mathbf{u}}$ are represented by block diagonal matrices containing the weights w_z and w_u . One may also have non-quadratic costs functions in MPC; examples are given by Bewley *et al.* (2001) for the control of a turbulent channel. In our case, we choose a quadratic cost function in order to compare performance with the LQR controller. By combining the cost function (53) and the state equation (49), we get

$$\begin{aligned} \mathcal{L}(k) &= \mathbf{z}_{\mathbf{p}}(k)^H \mathbf{W}_{\mathbf{z}} \mathbf{z}_{\mathbf{p}}(k) + \mathbf{u}_{\mathbf{p}}(k)^H \mathbf{W}_{\mathbf{u}} \mathbf{u}_{\mathbf{p}}(k) = \\ &= [\mathbf{P}_{\mathbf{z}\mathbf{v}}\mathbf{v}(k) + \mathbf{P}_{\mathbf{z}\mathbf{u}}\mathbf{u}_{\mathbf{p}}(k)]^H \mathbf{W}_{\mathbf{z}} [\mathbf{P}_{\mathbf{z}\mathbf{v}}\mathbf{v}(k) + \mathbf{P}_{\mathbf{z}\mathbf{u}}\mathbf{u}_{\mathbf{p}}(k)] + \\ &\quad + \mathbf{u}_{\mathbf{p}}(k)^H \mathbf{W}_{\mathbf{u}} \mathbf{u}_{\mathbf{p}}(k). \end{aligned} \quad (54)$$

Note that this manipulation is analogous to the definition of Lagrangian already shown for the LQR problem (42). The minimization of $\mathcal{L}(k)$ with respect of $\mathbf{u}_{\mathbf{p}}(k)$ reads

$$\min_{\mathbf{u}_{\mathbf{p}}(k)} \left\{ \frac{1}{2} \mathbf{u}_{\mathbf{p}}^H(k) \mathbf{H} \mathbf{u}_{\mathbf{p}}(k) + \mathbf{c}(k) \mathbf{u}_{\mathbf{p}}(k) : C \mathbf{u}_{\mathbf{p}}(k) \leq D \right\} \quad (55)$$

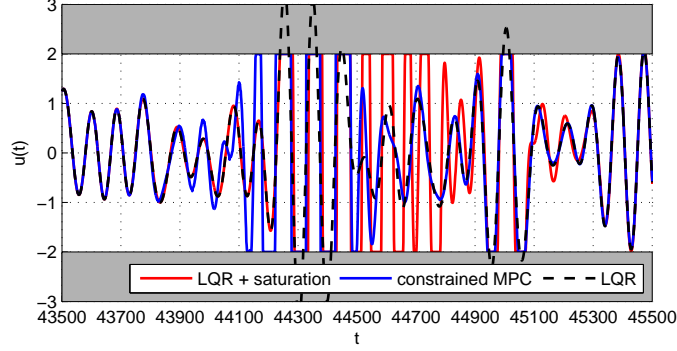


FIGURE 13. Control design in presence of constraints: the grey regions indicate the limits imposed to the amplitude of the control signal $u(t)$. The control $u(t)$ is designed following two different strategies: LQR with a saturation function (—) and constrained MPC (—), see §3.2.2. The LQR solution (---) is introduced as reference. The performances of the controllers are shown in terms of *rms*-velocity reduction in Figure 14.

where

$$\begin{aligned} \mathbf{H} &= 2 (\mathbf{P}_{\mathbf{z}\mathbf{u}}^H \mathbf{W}_{\mathbf{z}} \mathbf{P}_{\mathbf{z}\mathbf{u}} + \mathbf{W}_{\mathbf{u}}) \\ \mathbf{c}(k) &= 2 \mathbf{v}^H(k) \mathbf{P}_{\mathbf{z}\mathbf{v}}^H \mathbf{W}_{\mathbf{z}} \mathbf{P}_{\mathbf{z}\mathbf{u}} \end{aligned} \quad (56)$$

and $C\mathbf{u}_{\mathbf{p}}(k) \leq D$ is a constraint (Bryd *et al.* 1999), which we have not specified yet. Once this minimization problem is solved, the control signal is applied for one time step, corresponding to $\Delta T = T_a$, followed by a new iteration at step $k + 1$.

3.2.2. Actuator saturation as constraint

The need of introducing constraints in the optimization process usually arises when we consider real actuators characterized by nonlinear behaviour, due for instance to saturation effects. For example, the body force generated by plasma actuators (Grundmann & Tropea 2008; Corke *et al.* 2010) – usually approximated by considering the macroscopic effects on a flow – is often modelled as a nonlinear function of the voltage (Suzen *et al.* 2005; Kriegseis 2011).

Consider now a control signal, whose amplitude is required to be bounded in the interval $-u_{\max} \leq u \leq u_{\max}$. We thus minimize

$$\min_{\mathbf{u}_{\mathbf{p}}(k)} \left\{ \frac{1}{2} \mathbf{u}_{\mathbf{p}}^H(k) \mathbf{H} \mathbf{u}_{\mathbf{p}}(k) + \mathbf{c}(k) \mathbf{u}_{\mathbf{p}}(k) : \bar{\mathbf{u}}_{\min} \leq \mathbf{u}_{\mathbf{p}}(k) \leq \bar{\mathbf{u}}_{\max} \right\}, \quad (57)$$

where \mathbf{H} and \mathbf{c} are given by (56). One may solve this constrained MPC using nonlinear programming (Boyd & Vandenberghe 2004). Since the function to be minimized is a quadratic function, we have used a reflective Newton

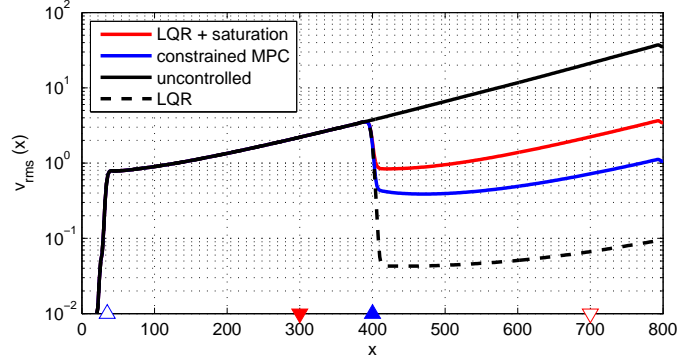


FIGURE 14. Control of the KS equation. The *rms* velocity as a function of the x direction is analyzed; the uncontrolled configuration (—) is compared to three different control strategies already considered in Figure 13 (same legend).

method suggested by Coleman & Li (1996); this method is implemented in the MATLAB® routine `quadprog.m`.

We proceed by comparing the performance of the MPC controller with the LQR solution discussed in §3.1.1. For a direct comparison, we apply an *ad hoc* saturation function to the LQR control signal, i.e.

$$u_{LQR} = \begin{cases} u_{LQR} & \text{if } \bar{u}_{min} < u_{LQR} < \bar{u}_{max} \\ \bar{u}_{min} & \text{if } \bar{u}_{min} \geq u_{LQR} \\ \bar{u}_{max} & \text{if } \bar{u}_{max} \leq u_{LQR} \end{cases} . \quad (58)$$

As shown in Figure 13, the control signal computed by the MPC (blue solid line) closely follows the LQR solution (dashed black line), except in the intervals where the value is larger or smaller than the imposed constraint. By simply applying the saturation function in (58) to the LQR signal, the controller becomes suboptimal; the resulting solution deviates from the optimal one and settles back on it after $t \approx 300$ time units. Simply cutting off the actuator signal of LQR results in a significant reduction of performance, which in terms of root-mean-square (*rms*) is almost one order of magnitude (shown in Figure 14). The main drawback of the constrained MPC is the computational time required by the on-line optimization, that can be prohibitive in experimental settings.

3.2.3. MPC for linear systems without constraints

For a linear system with the quadratic cost function (40) but without constraints, a prediction/actuation time sufficiently long allows to approximate the solution of the LQR. This is not obvious from the mere comparison of the continuous-time LQR-objective function, (40) and (42), and the discrete-time MPC-objective function, (53) and (54). For a detailed discussion, we refer to

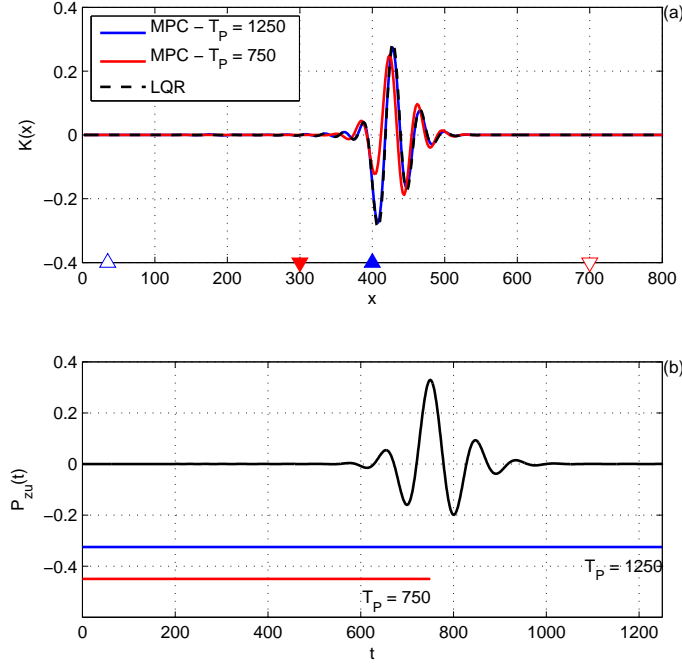


FIGURE 15. In (a) the LQR solution (§3.1.1) is compared to the MPC gains computed for two different times of optimization T_p without constraints, see §3.2.3. The optimization times are compared to the impulse response $\mathcal{P}_{zu}(t)$ (b). Note that for longer time T_p , covering the main dynamics of the impulse response $\mathcal{P}_{zu}(t)$, the MPC and LQR solutions are equivalent.

Anderson & Moore (1990), where the equivalence is demonstrated analytically. In the following, the equivalence is exemplified using the KS equation.

When there are not imposed constraints, the optimization problem in (55) corresponds to a Quadratic Program (Boyd & Vandenberghe 2004); by taking the derivative of $\mathcal{L}(k)$ with respect of $\mathbf{u}_p(k)$, we may obtain $\mathbf{u}_p(k)$ as solution of the following least-square problem

$$\begin{aligned}
 \mathbf{u}_p(k) &= -\mathbf{H}^\dagger \mathbf{c}^H = \\
 &= -(\mathbf{P}_{zu}^H \mathbf{W}_z \mathbf{P}_{zu} + \mathbf{W}_u)^\dagger \mathbf{P}_{zu}^H \mathbf{W}_z \mathbf{P}_{zv} \mathbf{v}(k) = \\
 &= \begin{bmatrix} \mathbf{K}_0 \\ \mathbf{K}_1 \\ \vdots \\ \mathbf{K}_{N-1} \end{bmatrix} \mathbf{v}(k), \tag{59}
 \end{aligned}$$

where $(\cdot)^\dagger$ indicates the Moore-Penrose generalized inverse matrix, (Penrose 1955). Note that this is a least square problem (in general, $M \geq N$). If we assume an actuation time-horizon $T_a = \Delta t$, at each time step the control signal $u(k)$ reads

$$u(k) = \mathbf{K}_0 \mathbf{v}(k). \quad (60)$$

In Figure 15(a), the solid dashed line corresponds to the LQR gain obtained by solving a Riccati equation, while the coloured lines correspond to the unconstrained MPC solution for different final time of prediction T_p . For a shorter time of optimization ($T_p = 750$, red solid line) only a portion of the dynamics of $\tilde{\mathcal{P}}_{zu}(i)$ (see Figure 15(b)) is contained in the MPC gain. For longer times ($T_p = 1250$, blue solid line) the MPC converges to the infinite-time horizon LQR solution.

4. Estimation

In this section, we assume that the only information we can extract from the system is the measurement $y(t)$. This signal is used to provide an estimation $\hat{\mathbf{v}}(t)$ of the state such that the error given by

$$\mathbf{e}(t) = \mathbf{v}(t) - \hat{\mathbf{v}}(t), \quad (61)$$

is kept as small as possible. We first derive the classical Kalman Filter, where in addition to $y(t)$, one requires a state-space model of the physical system. Then we discuss the least-mean square (LMS) technique, which only relies on the measurement $y(t)$.

4.1. Luenberger observer and Kalman filter

The observer is a system in the following form

$$\dot{\hat{\mathbf{v}}}(t) = \mathbf{A} \hat{\mathbf{v}}(t) + \mathbf{B}_u u(t) - \mathbf{L} (y(t) - \hat{y}(t)), \quad (62)$$

$$\hat{y}(t) = \mathbf{C}_y \hat{\mathbf{v}}(t), \quad (63)$$

$$\hat{z}(t) = \mathbf{C}_z \hat{\mathbf{v}}(t). \quad (64)$$

This formulation was proposed for the first time by Luenberger in Luenberger (1979), from whom it takes the name. Comparing this system with (18), it can be noticed that it takes into account the actuator signal $u(t)$ but it ignores the unmeasurable inputs – the disturbance $d(t)$ and the measurement error $n(t)$. In order to compensate this lack of information, a correction term based on the estimation $\hat{y}(t)$ of the measurement $y(t)$ is introduced, filtered by the gain matrix \mathbf{L} .

The aim is to design \mathbf{L} in order to minimize the magnitude of the error between the real and the estimated state, i.e. expression defined in (61). Taking the difference term by term between (18) and (62), an evolution equation for the $\mathbf{e}(t)$ is obtained,

$$\dot{\mathbf{e}}(t) = (\mathbf{A} + \mathbf{LC}) \mathbf{e}(t) + \mathbf{B}_d d(t) - \mathbf{L} n(t). \quad (65)$$

It can be seen that the error is forced by the disturbance $d(t)$ and the measurement error $n(t)$, i.e. precisely the unknown inputs of the system.

4.1.1. Kalman filter

In the Kalman filter approach both the disturbance $d(t)$ and the measurement error $n(t)$ are modelled by white noise, requiring a statistical description of the signals. The auto-correlation of the disturbance signal is given by

$$\mathcal{R}_d(\tau) \triangleq \int_{-\infty}^{+\infty} d(t) d^H(t - \tau) dt. \quad (66)$$

This function tells us how much a signal is correlated to itself after a shift τ in time. For a white noise signal this function is non-zero only when a zero shifting ($\tau = 0$) in time is considered and its value is the variance of the signal. Hence, the correlation functions for the considered inputs signal $d(t)$ and $n(t)$ are

$$\mathcal{R}_d(\tau) = R_d \delta(\tau) \quad \text{and} \quad \mathcal{R}_n(\tau) = R_n \delta(\tau), \quad (67)$$

where R_d and R_n are the variances of the two signals and $\delta(\tau)$ is the continuous Dirac delta function. When a system is forced by random signals, also the state becomes a random process and it has to be described via its statistical properties. Generally the calculation of these statistics requires a long time history of the response of the system to the random inputs. But for the linear system (65), it is possible to calculate the variance of the state $\mathbf{R}_e \in \mathbb{R}^{n_v \times n_v}$ by solving the following Lyapunov equation (Bagheri *et al.* 2009c)

$$(\mathbf{A} + \mathbf{L}\mathbf{C}_y)^H \mathbf{R}_e + \mathbf{R}_e (\mathbf{A} + \mathbf{L}\mathbf{C}_y) + \mathbf{B}_d R_d \mathbf{B}_d^H + \mathbf{L} R_n \mathbf{L}^H = \mathbf{0}. \quad (68)$$

The trace of \mathbf{R}_e is a measure of how much the mean value of the error $\mathbf{e}(t)$ differs from zero during its time evolution. One may thus define the following cost function for the design of \mathbf{L}

$$\mathcal{N} = \text{Tr}(\mathbf{R}_e) = \lim_{T \rightarrow \infty} \frac{1}{2T} \int_{-T}^T \mathbf{e}^H(t) \mathbf{e}(t) dt, \quad (69)$$

where $\text{Tr}(\cdot)$ indicates the trace operator.

With a similar approach as in §3.1, we define a Lagrangian:

$$\begin{aligned} \tilde{\mathcal{N}} = \text{Tr} \left\{ \mathbf{R}_e + \lambda \left[(\mathbf{A} + \mathbf{L}\mathbf{C}_y)^H \mathbf{R}_e + \mathbf{R}_e (\mathbf{A} + \mathbf{L}\mathbf{C}_y) + \right. \right. \\ \left. \left. + \mathbf{B}_d R_d \mathbf{B}_d^H + \mathbf{L} R_n \mathbf{L}^H \right] \right\} \end{aligned} \quad (70)$$

where the Lagrangian multiplier λ enforce the constraint given by (68). The solution of the minimization is obtained by the imposing the solution to be stationary respect the three parameters \mathbf{L} , \mathbf{R}_e and λ . The zero-gradient condition for \mathbf{L} gives us the expression for the estimation gain,

$$\mathbf{L} = -R_n^{-1} \mathbf{C}_y \mathbf{R}_e. \quad (71)$$

The zero-gradient condition for the Lagrangian multiplier λ returns the Lyapunov equation in (68): combining this equation with (71), a Riccati equation

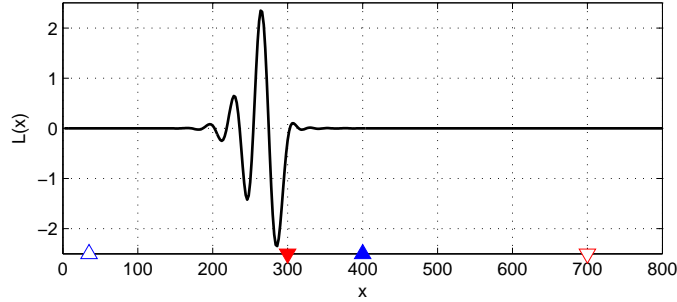


FIGURE 16. Kalman estimation gain \mathbf{L} computed for $R_d = 1$ and $R_n = 0.1$, (see §4.1.1). [script06.m]

is obtained for \mathbf{R}_e :

$$\mathbf{A}^H \mathbf{R}_e + \mathbf{R}_e \mathbf{A} - \mathbf{R}_e \mathbf{C}_y^H R_n^{-1} \mathbf{C}_y + \mathbf{B}_d R_d \mathbf{B}_d^H = \mathbf{0}. \quad (72)$$

In Figure 16 the estimation gain \mathbf{L} is shown, where it can be observed that the spatial support is localized in the region immediately upstream of the sensor y . In this region the amplitude of the forcing term in the estimator is the largest to suppress estimation error. In Figure 17 we compare the full state (a) to the estimated state (b) when the system is forced by a noise signal $d(t)$. As a result of strong convection, we observe that an estimation is possible only after the disturbance has reached the sensor at $x = 300$, since upstream of this point there are no measurements. For control design it is important that $\mathbf{v}(t)$ is well estimated in the region where the actuators are placed; hence, the actuators have to be placed downstream of the sensors (Belson *et al.* 2013; Juliet *et al.* 2013).

4.2. Estimation based on linear filters

A significant drawback of the Kalman filter, is that it requires a model of the disturbance \mathbf{B}_d for the solution of the Riccati equation (72). One may circumvent this issue by using FIR to formulate the estimation problem. In analogue to the formulations based LQR (model based) and on MPC (FIR based), we will compare and link the Kalman filter to a system identification technique called the Least-Square-Mean filter (LMS). Many other system identification technique exists, the most common being the AutoRegressive-Moving-Average with eXogenous inputs (ARMAX) employed in the work of Hervé *et al.* (2012).

From (62–64), we observe that the estimator-input is the measurement $y(k)$, while the output is given by the estimated values of $z(k)$. The associated FIR of this system is

$$\hat{z}(k) = \sum_{i=N_{i,zy}}^{N_{f,zy}} \left(-\mathbf{C}_z \hat{\mathbf{A}}^{i-1} \Delta t \mathbf{L} \right) y(k-i) = \sum_{i=N_{i,zy}}^{N_{f,zy}} \tilde{\mathbf{E}}_{zy}(i) y(k-i) \quad (73)$$

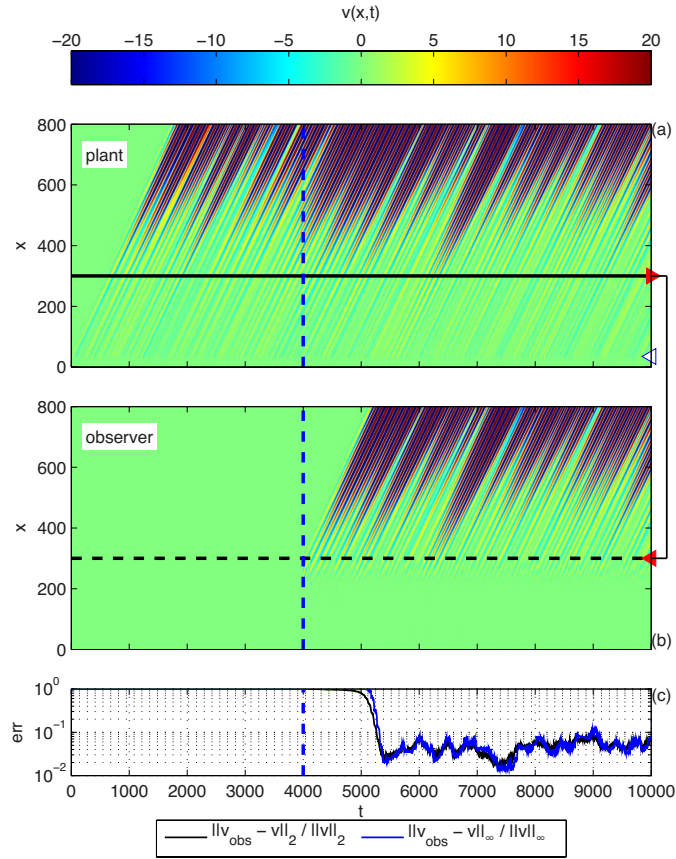


FIGURE 17. Spatio-temporal evolution of the response of the system to a disturbance $d(t)$ (a), compared to the estimated full-order state, using a Kalman filter (b); the contours are shown as a function of the streamwise direction (x) and time (t). The error-norm between the original state and the estimated state is shown in (c). The vertical blue, dashed line indicates when the estimator is turned on. [script06.m]

where $\hat{\mathbf{A}} = e^{(\mathbf{A} + \mathbf{L}\mathbf{C}_y)\Delta t}$ and $\tilde{\mathcal{E}}_{zy}(i)$ denotes the impulse response from the measurement $y(k)$ to the output $z(k)$. Note that, since we are considering a convectively unstable system, the sum in (73) is truncated using appropriate limits $N_{i,zy}$ and $N_{f,zy}$ (Aström & Wittenmark 1995). Next, we present a method where $\tilde{\mathcal{E}}_{zy}(i)$ is approximated directly from measurements, instead of its construction using the state-space model.

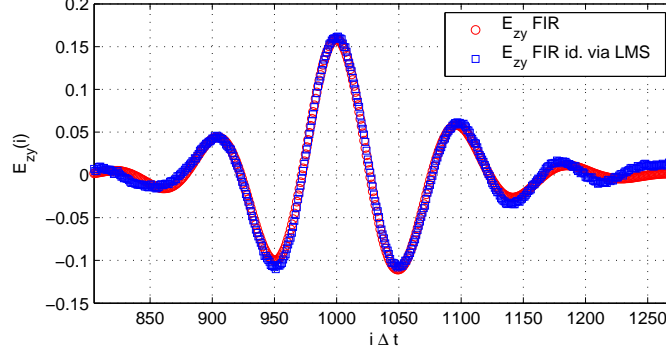


FIGURE 18. Impulse responses ($y \rightarrow z$) of the estimator as a function of the discrete-time. Red circles (\circ) correspond to the FIR time-discrete Kalman-filter-based kernel $\tilde{\mathcal{E}}_{zy}(i)$ and the blue squares (\square) to the one identified by the LMS algorithm. [script07.m]

4.2.1. Least-mean-square (LMS) filter

The main idea is to identify an estimated output $\hat{z}(k)$ for the system, by minimizing the error

$$e(k) = \hat{z}(k) - z(k) = \left(\sum_{i=N_{i,zy}}^{N_{f,zy}} \tilde{\mathcal{E}}_{zy}(i) y(k-i) \right) - z(k), \quad (74)$$

where $z(k)$ is the reference measurement. The unknown of the problem is the time-discrete kernel $\tilde{\mathcal{E}}_{zy}(i)$. Thus, we aim at adapt the kernel $\tilde{\mathcal{E}}_{zy}(i)$ such that at each time step the error $e(k)$ is minimized, i.e.

$$\min_{\tilde{\mathcal{E}}_{zy}} e^2(k). \quad (75)$$

The minimization can be performed using a steepest descent algorithm (Haykin 1986); thus, starting from an initial guess at $k = 0$ for $\hat{z}(k)$, $\tilde{\mathcal{E}}_{zy}$ is updated at each iteration as

$$\tilde{\mathcal{E}}_{zy}(i|k+1) = \tilde{\mathcal{E}}_{zy}(i|k) + \mu(k) \lambda(i|k), \quad (76)$$

where $\lambda(i|k)$ is the direction of the update and $\mu(k)$ is the step-length. Note that each iteration corresponds to one time step. The direction can be obtained from the local gradient, which is given by,

$$\lambda(i|k) = -\frac{\partial e^2(k)}{\partial \tilde{\mathcal{E}}_{zy}(i)} = -2 e(k) y(k-i). \quad (77)$$

This expression was obtained by forming the gradient of the error $e(k)$ with respect to $\tilde{\mathcal{E}}_{zy}(i)$ and making use of the estimated output $\hat{z}(k)$ (73).

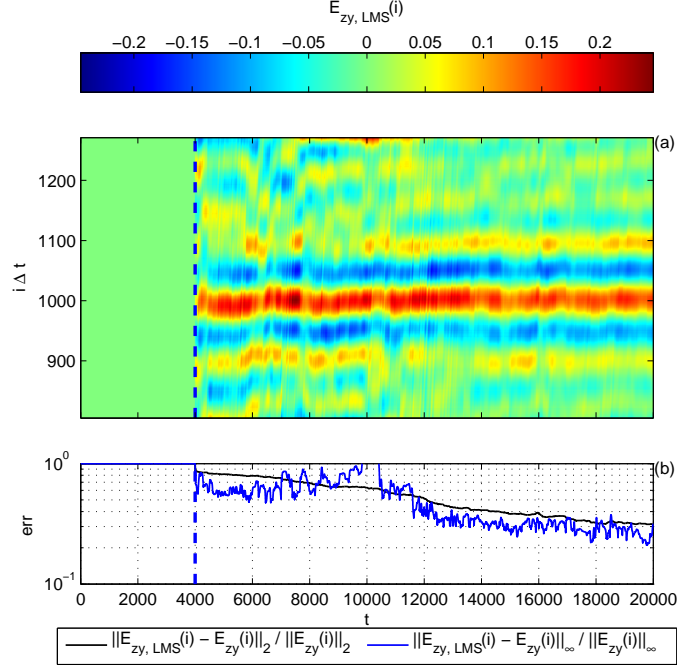


FIGURE 19. In (a) the evolution of $\tilde{\mathcal{E}}_{zy}(i)$ is calculated by an adaptive LMS filter and shown as a function of the discrete-time ($i\Delta t$). The estimation starts at $t = 4000$, as indicated by a blue dashed line (- -). As the iteration progresses, the error-norm constantly reduces (c). [script07.m]

The second variable that needs to be computed in (76) is the step-length $\mu(k)$. Consider the error at time-step k computed with the updated kernel $\tilde{\mathcal{E}}_{zy}(i|k+1)$

$$\begin{aligned} \tilde{e}(k) &= \left(\sum_{i=N_{i,zy}}^{N_{f,zy}} \tilde{\mathcal{E}}_{zy}(i|k+1) y(k-i) \right) - z(k) = \\ &= e(k) + \mu(k) \left(\sum_{i=N_{i,zy}}^{N_{f,zy}} \lambda(i|k) y(k-i) \right), \end{aligned} \quad (78)$$

where (75) and (76) have been used. The step-length $\mu(k)$ is calculated at each time step in order to fulfil

$$\min_{\mu(k)} \tilde{e}(k)^2 \quad (79)$$

by imposing a zero-derivative condition with respect to $\mu(k)$,

64 *N. Fabbiane, O. Semeraro, S. Bagheri & D. S. Henningson*

$$\frac{\partial \tilde{e}(k)^2}{\partial \mu(k)} = 2 \tilde{e}(k) \left(\sum_{i=N_{i,zy}}^{N_{f,zy}} \lambda(i|k) y(k-i) \right) = 0. \quad (80)$$

Assuming that

$$\sum_{i=N_{i,zy}}^{N_{f,zy}} \lambda(i|k) y(k-i) \neq 0 \quad (81)$$

and considering (78), the optimal step length becomes

$$\mu(k) = -\frac{e(k)}{\sum_i \lambda(i|k) y(k-i)}. \quad (82)$$

In Figure 19(a), the LMS-identified kernel $\tilde{\mathcal{E}}_{zy}(i)$ is shown as a function of time $t = k\Delta t$. When the LMS filter is turned on at $t = 4000$, the filter starts to compute the kernel, which progressively adapts. While the iteration proceeds, the error decreases as shown in Figure 19(b). In the limit of $T \rightarrow \infty$, when a steady solution can be assumed, the kernel computed by the LMS filter converges to the kernel $\tilde{\mathcal{E}}_{zy}$ obtained by the Kalman filter (see Figure 18).

The main drawback of the LMS approach is that the method is susceptible to a numerical stability (Haykin 1986). A usual way for improving the stability is to bound the the step-length $\mu(k)$ by introducing an upper limit. In particular, it can be proven that in order to ensure the convergence of the algorithm, the following condition has to be satisfied

$$0 < \mu(k) < \bar{\mu} = \frac{2}{R_y}, \quad (83)$$

where the upper-bound $\bar{\mu}$ is defined by the variance R_y of the measurement y , i.e. the input signal to LMS filter.

5. Compensator

Using the theory developed in §3 and §4, we are now ready to tackle the full control problem (Figure 20): given the measurement $y(t)$, compute the modulation signal $u(t)$ in order to minimize a cost function based on $z(t)$. In the first part of this section we will focus on the LQG regulator, that couples a Kalman filter to a LQR controller. Then we present a compensator based on adaptive algorithms using LMS techniques.

5.1. Linear-quadratic Gaussian (LQG) regulator

By solving the control and estimation Riccati equations and the associated gains (\mathbf{L} and \mathbf{K}), we build a system that has as an input the measurement $y(t)$ and as an output the control signal $u(t)$:

$$\dot{\hat{\mathbf{v}}}(t) = (\mathbf{A} + \mathbf{B}_u \mathbf{K} + \mathbf{L} \mathbf{C}_y) \hat{\mathbf{v}}(t) - \mathbf{L} y(t) \quad (84)$$

$$u(t) = \mathbf{K} \hat{\mathbf{v}}(t). \quad (85)$$

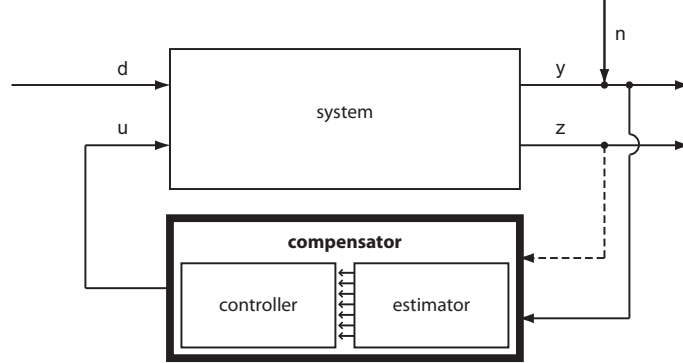


FIGURE 20. Block-diagram of the closed-loop system. The compensator, consisting of a controller coupled to an estimator, computes the control signal $u(t)$ given the measurement $y(t)$. The minimization of the measurement $z(t)$ is the target parameter of the controller. Note that in a feedforward controller, the output z can be used to add robustness to the compensator (for instance, in adaptive filters, §5.4).

This linear system is referred to as the LQG compensator. The estimation and control problem, discussed in the previous sections, are both optimal and guarantee stability as long as the system is observable and controllable (Glad & Ljung 2000). In particular, the disturbance d and the output z have to be placed respectively in the y -observable and u -controllable region (Figure 8). Under these conditions, a powerful theorem, known as the separation principle (Glad & Ljung 2000), states that optimality and stability transfer to the LQG compensator.

The closed-loop system obtained by connecting the compensator to the plant becomes

$$\begin{bmatrix} \dot{\hat{\mathbf{v}}}(t) \\ \dot{\hat{\mathbf{z}}}(t) \end{bmatrix} = \begin{bmatrix} \mathbf{A} & \mathbf{B}_u \mathbf{K} \\ -\mathbf{L} \mathbf{C}_y & \mathbf{A} + \mathbf{B}_u \mathbf{K} + \mathbf{L} \mathbf{C}_y \end{bmatrix} \begin{bmatrix} \mathbf{v}(t) \\ \hat{\mathbf{v}}(t) \end{bmatrix} + \begin{bmatrix} \mathbf{B}_d \\ \mathbf{0} \end{bmatrix} d(t). \quad (86)$$

Figure 21 shows the response of (86) when a white random noise is considered as an input in $d(t)$. The horizontal solid black line in the top frame depicts the location of y sensor: this signal is used to force the compensator at the location depicted in the lower frame with a black dashed line. The compensator then provides a signal to the actuator (dashed black line in the upper frame) to cancel the propagating wave-packet. We let the two systems start to interact at $t = 4000$, as depicted by the dashed blue line. As soon as the first wave-packet, that is reconstructed by the compensator, reaches the actuation area, the compensator starts to provide a non-zero actuation signal back to the plant. Recall that the state $\hat{\mathbf{v}}(t)$ of the LQG compensator is an estimation of the state of the real plant $\mathbf{v}(t)$. This can be seen by comparing Figure 21(a) and

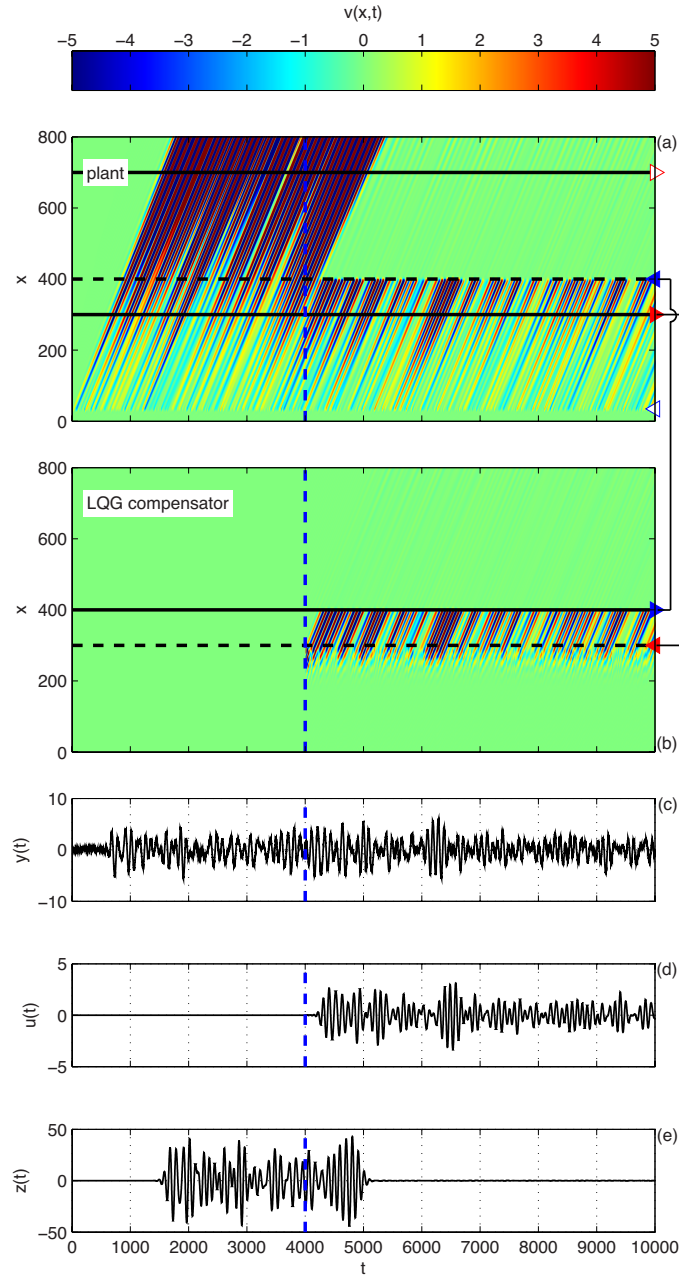


FIGURE 21. Spatio-temporal response in presence of a white noise input $d(t)$ for the closed-loop system (a) and the compensator (b); the disturbance is shown as a function of the streamwise direction (x) and time (t). The measurement $y(t)$, feeding the compensator, is shown in (c). At $t = 4000$ (---), the compensator starts its action and after a short lag the actuator is fed with the computed control signal $u(t)$. The perturbation is cancelled, as shown in the contours reported in (a) and the output $z(t)$ minimized ($t > 5000$). [script08.m]

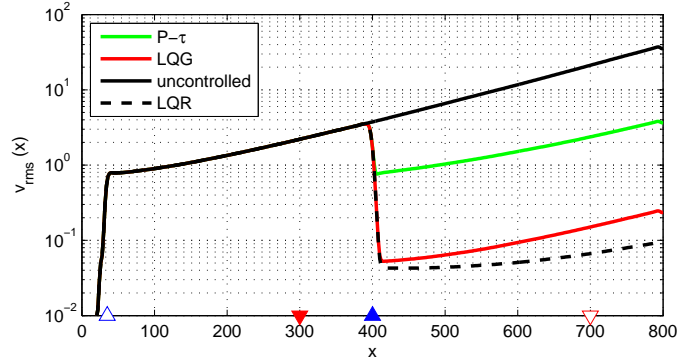


FIGURE 22. The *rms* velocity as a function of the streamwise location x is shown for the uncontrolled case (—), the LQG (—), the LQR (— —) and the opposition controller $P - \tau$ (—). [script08.m, script09.m]

Figure 21(b); downstream of the sensor y the state of the compensator matches the controlled plant.

Optimal controllers were applied to a large variety of flows, including oscillator flows, such as cavity and cylinder-wake flow, where the dynamic is characterized by self-sustained oscillations at well-defined frequencies, see Sipp *et al.* (2010). Note that $\mathbf{v}(t)$ and $\hat{\mathbf{v}}(t)$ have the same size: if complex systems are considered, a full-order compensator can be computationally demanding (Semeraro *et al.* 2013); model reduction and compensator reduction enable to tackle these limitations and design low-order compensators, see §6.

5.2. Proportional controller with a time delay

One may ask how a simple proportional controller compares to the LQG for our configuration. In a proportional compensator, the control signal $u(t)$ is simply obtained by multiplying the measurement signal $y(t)$ by a constant P . Because of the strong time delays in our system, one needs to introduce also a time-delay τ between the measurement $y(t)$ and the control signal $u(t)$. The simplest control law for our system is

$$u(t) = P y(t - \tau), \quad (87)$$

where the “best” gain P and the time-delay τ can be found via a trial-and-error basis (in our case, $\tau = 250$ and $P = -0.5432$). This technique is also similar to opposition control (Choi *et al.* 1994), where blowing and suction is applied at the wall in opposition to the wall-normal fluid velocity, measured a small distance from the wall.

In Figure 22, we compare the velocity *rms* obtained with LQG compensator (red) and P - τ compensator (green). It can be observed that although both techniques reduce the perturbation amplitude downstream of the actuator

position ($x = 400$), the performance of the LQG regulator is nearly an order of magnitude better than the proportional controller. This can be mainly attributed to the additional degrees of freedom given by the $n_v \times n_v$ LQG feedback gains, as opposed to the two-degree freedom $P - \tau$ controller. Indeed, the LQG gains are computed assuming an accurate knowledge of the state-space model. Also shown (dashed-solid line) is the full-information LQR control whose performance is comparable the partial-information LQG controller: the difference between the two is due to the difference between the estimated state $\hat{\mathbf{v}}(t)$ and the real state $\mathbf{v}(t)$, i.e. the estimation error \mathbf{e} .

5.3. Model uncertainties

The LQG compensator is based on coupling an LQR controller and a Luenberger observer. Both of them are based on a model of the system and, as a consequence, their effectiveness is highly dependent on the quality of the model itself. Any difference between the model and the real plant can cause an abrupt reduction of the performances of the compensator (Doyle 1978; Belson *et al.* 2013). Model error can be attributed to, for example, nonlinearities due to the violation of the small perturbation hypothesis, nonlinearities of the actuator or sensors/actuators shape and positioning.

The robustness problem can be illustrated using a simple example. Suppose that one wants to cancel a travelling wave with a localized actuator; what one should do is to generate a wave that is exactly counter-phase with respect to the original one. Suppose that exact location of the actuation action is difficult to model. Shifting the actuator position slightly is equivalent to adding an error in the estimation of the phase of the original signal. This will in turn cause a mismatch between the wave that is meant to be cancelled and the wave created by the actuator, thus resulting in an ineffective wave cancellation – in the worst case, it may result in an amplification of the original wave.

As shown in Figure 23, when we displace the actuator further downstream by 5 spatial units and apply the compensator designed for the nominal condition to this modified system, the performance of the LQG regulator deteriorates. Since, the compensator provides a control signal that is meant to be applied in the nominal position of the actuator the control signal is not able to cancel the upcoming disturbance. Essentially, we are suffering from the lack of robustness of the feedforward configuration, since the sensor cannot measure the consequence of the defective actuator signal. There are different means to address this issue.

One can combine the feedforward configuration with a feedback action, in order to increase robustness. This can be accomplished using the second sensor z – downstream of the actuator – in combination with the estimation sensor y – placed upstream of the actuator. The combination of feedback and feedforward is the underlying idea of the MPC controller applied to our configuration (Goldin *et al.* 2013). However, there are some drawbacks due to the computational costs of the algorithm; indeed, the entries of the dynamic matrix (51)

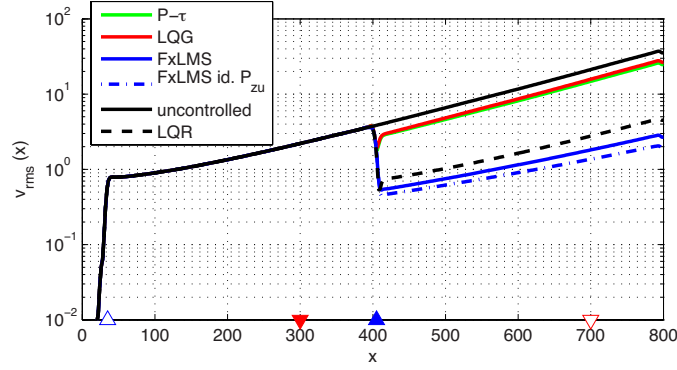


FIGURE 23. Robustness to uncertainties of the system: the actuator is displaced of 5 length units from its nominal position. The performance of the adaptive filter FXLMS (— and ·—) are compared to the LQR (— —), LQG (—) and P - τ (—) compensators; as a reference, the uncontrolled case is shown (—). The *rms*-velocity is shown as a function of the stream-wise direction (x). The adaptive filter performs reasonably well in presence of un-modelled dynamics; the performances are enhanced by the use of a on-line identified \hat{P}_{zu} (— —). The performances of the LQG (—) and P - τ (—) compensators are significantly reduced (compare with Figure 22).[script10.m]

are computed during the prediction-step using time integration, whose domain increases with the time-delays of the system. Thus, the integration and the dimensions of the resulting matrices can represent a bottleneck for the on-line optimization. An alternative is the use of an adaptive algorithm, which adapts the compensator response according to the information given by $z(t)$, as shown in the next section.

5.4. Filtered- X least-mean square (FXLMS)

The objective of FXLMS algorithm is to adapt the response of the compensator based on the information given by the downstream output z . The first step of the design is to describe the compensator in a suitable way in order to modify its response. The FXLMS algorithm is based on a FIR description of the compensator. Recall again that the compensator is a linear system (input is the measurement $y(t)$ and output is the control signal $u(t)$), which in time-discrete form can be represented by,

$$u(k) = \sum_{j=1}^{\infty} \tilde{K}_{uy}(j) y(k-j) \approx \sum_{j=1}^{N_{uy}} \tilde{K}_{uy}(j) y(k-j), \quad (88)$$

70 *N. Fabbiane, O. Semeraro, S. Bagheri & D. S. Henningson*

where $\tilde{\mathcal{K}}_{uy}(j)$ is a time-discrete kernel. Due to the stability of the system, we have $\tilde{\mathcal{K}}_{uy}(j) \rightarrow 0$ as $t \rightarrow \infty$, so that the sum can be truncated after N_{uy} steps. In the case of LQG compensator $\tilde{\mathcal{K}}_{uy}$ has the form

$$\tilde{\mathcal{K}}_{uy}(j) \triangleq \mathbf{K} \exp [(\mathbf{A} + \mathbf{L}\mathbf{C}_y + \mathbf{B}_u\mathbf{K}) \Delta t (j - 1)] \mathbf{L}$$

for $i = 1, 2, \dots$. The kernel $\tilde{\mathcal{K}}_{uy}(j)$ of the LQG controller is shown with red circles in Figure 24. In this case $N_{uy} = 533$, which gives $|\tilde{\mathcal{K}}_{uy}(j)| < 10^{-2}$ for $j > N_{uy}$.

The FXLMS technique modifies on-line the kernel $\tilde{\mathcal{K}}_{uy}(j)$ in order to minimize the square of measurement $z(t)$ at each time step (Sturzebecher & Nitsche 2003), i.e

$$\min_{\tilde{\mathcal{K}}_{uy}(j)} z^2(k). \quad (89)$$

The procedure is closely connected to the LMS filter discussed in §4.2.1 for the estimation problem. The kernel $\tilde{\mathcal{K}}_{uy}(j)$ is updated at each time step by a steepest-descend method:

$$\tilde{\mathcal{K}}_{uy}(j|k+1) = \tilde{\mathcal{K}}_{uy}(j|k) + \mu(k) \lambda(j|k) \quad (90)$$

where $\mu(k)$ is calculated from (82) and $\lambda(j|k)$ is the gradient of the cost function $z(k)$ with respect of the control gains $\tilde{\mathcal{K}}_{uy}(j)$. In order to obtain the update direction, consider the time-discrete convolution for $z(k)$,

$$\begin{aligned} z(k) &= \sum_{i=0}^{\infty} \tilde{\mathcal{P}}_{zd}(i) d(k-i) + \sum_{i=0}^{\infty} \tilde{\mathcal{P}}_{zu}(i) u(k-i) = \\ &= \sum_{i=0}^{\infty} \tilde{\mathcal{P}}_{zd}(i) d(k-i) + \sum_{i=0}^{\infty} \tilde{\mathcal{P}}_{zu}(i) \sum_{j=0}^{N_{uy}} \tilde{\mathcal{K}}_{uy}(j) y(k-i-j) = \\ &= \sum_{i=0}^{\infty} \tilde{\mathcal{P}}_{zd}(i) d(k-i) + \sum_{j=0}^{N_{uy}} \tilde{\mathcal{K}}_{uy}(j) \sum_{i=0}^{\infty} \tilde{\mathcal{P}}_{zu}(i) y(k-j-i). \end{aligned}$$

From this expression it is possible to obtain the gradient

$$\lambda(j|k) = -\frac{\partial z(k)^2}{\partial \tilde{\mathcal{K}}_{uy}(j)} = -2 z(k) \sum_{i=0}^{\infty} \tilde{\mathcal{P}}_{zu}(i) y(k-j-i), \quad (91)$$

which can be simplified by introducing the filtered signal $y_f(k)$,

$$y_f(k) = \sum_{i=0}^{\infty} \tilde{\mathcal{P}}_{zu}(i) y(k-j-i) \approx \sum_{i=N_{i,zu}}^{N_{f,zu}} \tilde{\mathcal{P}}_{zu}(i) y(k-i) \quad (92)$$

Note that a FIR approximation of $\tilde{\mathcal{P}}_{zu}(i)$ has been used. Hence, the expression in (91) becomes,

$$\lambda(j|k) = -2z(k) y_f(k-j). \quad (93)$$

In order to get the descend direction, the measurement $y(t)$ is filtered by the plant transfer function $\tilde{\mathcal{P}}_{zu}(i)$.

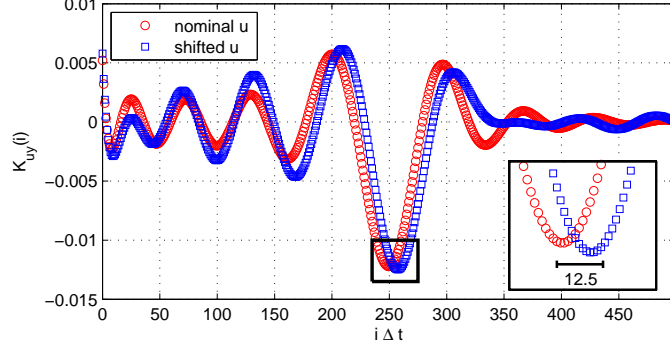


FIGURE 24. Robustness to uncertainties of the system: FXLMS control gain $\tilde{\mathcal{K}}_{uy}(i)$ (\square) is shifted along the time-discrete coordinate if compared to the static LQG gain (\circ) to compensate for the un-modelled shift in actuator position. [script10.m]

Starting the on-line optimization from the compensator kernel $\tilde{\mathcal{K}}_{uy}(j)$ given by the LQG solution, the algorithm is tested on our problem. In Figure 23 we observe that the algorithm is able to recover some of the lost performance of LQG (due to shift in actuator position) and it is comparable to the full-information control performed by the LQR controller with the nominal gain \mathbf{K} . This is possible because of the adaptation of the kernel $\tilde{\mathcal{K}}_{uy}(j)$, to the new actuator location. Figure 24 shows how the convolution kernel has been modified by the algorithm; the kernel is shifted in time in order to restore the correct phase shift between the control signal $u(t)$ and the measurement signal $y(t)$ in the modified system. The shift in time between the two peaks (visible in the inset figure) is exactly the time that it takes for the wave-packet to cover the additional distance between the sensor and the actuator. Recalling from §2, that the wave-packet travels with a speed $V = 0.4$, it will take $\Delta x_u/V = 5/0.4 = 12.5$ time units to cover the extra space between u and y .

From (91), it can be noted that the FXLMS is not completely independent from a model of the system; in fact the convolution kernel $\tilde{\mathcal{P}}_{zu}(i)$ is needed to compute the gradient $\lambda(j|k)$ used by the algorithm. In the previous example, the nominal transfer function has been used, given by the model of the plant

$$\tilde{\mathcal{P}}_{zu}(i) = \mathbf{C}_z e^{\mathbf{A} \Delta t(i-1)} \mathbf{B}_u, \quad i = 1, 2, \dots \quad (94)$$

One may obtain a kernel $\tilde{\mathcal{P}}_{zu}(i)$ that is totally independent by the model – thus without any assumption on placement/shape of both actuator and sensors – by using the LMS identification algorithm derived in §4.2.1. In Figure 23, we compare $\tilde{\mathcal{P}}_{zu}(i)$ obtained from (94) using inaccurate state-space model – since actuator position has shifted (solid blue) – with $\tilde{\mathcal{P}}_{zu}(i)$ obtained by model-free

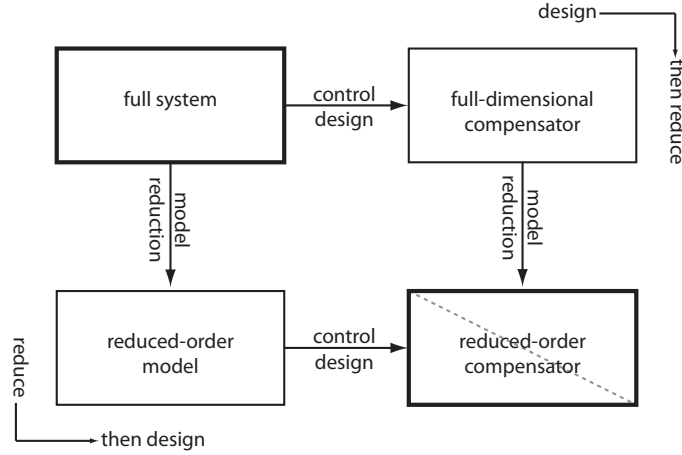


FIGURE 25. Two strategies are possible to compute a reduced-order compensator, reduce-then-design and design-then-reduce. In general, the two paths do not lead at the same results.

identification using LMS technique (dashed blue). We observe that when combining adaptiveness with a more accurate model-free identification of $\tilde{\mathcal{P}}_{zu}(i)$, the performance is improved significantly.

Note that this algorithm when applied to flows dominated by convection, and thus characterized by strong time-delays, results in a feedforward controller where the feedback information is recovered by the processing of the measurements in z . This method is known to as *active noise cancellation* (Sturzebecher & Nitsche 2003; Erdmann *et al.* 2012). We can identify two time scales: a fast time-scale related to the estimation process and a slow time-scale related to the adaptive procedure (el Hak 2007). For this reason, this method is suitable for static or slowly varying model discrepancies.

6. Discussion

In this section, we discuss a few aspects that have not been addressed so far, but are important to apply the presented techniques to an actual flowing fluid. Many other important subjects such as choice of actuator and sensors, nonlinearities and receptivity are not covered by this discussion.

Low-order control design. The discretization of the Navier-Stokes system leads to high-dimensional systems that easily exceed 10^5 degrees of freedom. For instance, the full-order solution of Riccati equations for optimal control and Kalman filter problems cannot be obtained using standard algorithms (Benner 2004). One common strategy is to replace the high-dimensional system with a low-order system able to reproduce the essential input-output dynamics of the original plant. This approach is referred to as reduce-then-design (Anderson & Liu 1989), left part of Figure 25. First, a reduced-order model is identified

using an appropriate model reduction or system identification technique; then the validated reduced-order model is used to design a low-order compensator. The dual approach is called design-then-reduce or compensator reduction, right part of Figure 25. In this case, a high-order compensator is designed as first step (if possible). The second step is the reduction of the compensator to a low-order approximation.

Both the approaches lead to a low-order compensator that can be used to control the full-order plant, but they are not necessarily equivalent (Anderson & Liu 1989). In the reduce-then-design approach, we neglect a number of states during the model-order reduction of the open loop, that might become important for the dynamics of the closed-loop system. Despite these limitations, the reduce-then-design approach is the most common in flow control due to its computational advantages; indeed, the challenge of designing a high-dimensional compensator to be reduced strongly limits this alternative.

Model reduction. Following the reduce-then-design approach, the first step consists of identifying a reduced-order model, typically reproducing the I/O behaviour of the system. We can distinguish two classes of algorithms. The first category is based on a Petrov-Galerkin projection of the full-order system. In this case, the I/O behaviour of the system is reconstructed starting from a low-order approximation of the state-vector \mathbf{v}_r , characterized by a number of degree of freedom $r \ll n$; the projection can be performed on global modes (Akervik *et al.* 2007), proper orthogonal modes (POD), obtained from the diagonalization of the controllability Gramian (see §2.6), or balanced modes, for which the controllability and observability Gramians are equal and diagonal (Moore 1981; Rowley 2005; Bagheri *et al.* 2009c). This strategy has been widely used in the flow-control community in the past years for the identification of linear (Akervik *et al.* 2007; Ilak & Rowley 2008; Bagheri *et al.* 2009b; Barbagallo *et al.* 2009; Semeraro *et al.* 2011) and nonlinear models (Noack *et al.* 2003; Siegel *et al.* 2008; Ilak *et al.* 2010). In particular, when nonlinear effects are considered, it is necessary to take into account the effect that a finite disturbance in the flow has on the base-flow, as shown by Noack *et al.* (2003) for a cylinder wake flow. At low Reynolds numbers, a small number of modes are sufficient to reproduce the behaviour of oscillators such as the cylinder wake, while a larger number of modes is required to reproduce the I/O behaviour of convective unstable flows. This is mainly due to the presence of strong time-delays (Glad & Ljung 2000) that characterize this type of systems, §2.5.

The second approach stems from the I/O analysis of the formal solution carried out in §2.5; we note that a low-order representation of the transfer function is enough to reconstruct the I/O behaviour of the system. The computation of this representation can be performed applying *system identification* algorithms (Ljung 1999). Once the transfer functions are identified, one constructs a reduced-order model in canonical form. These techniques were widely used for experimental investigations (see e.g. Lundell (2007) and Rathnasingham & Breuer (2003)) and have been recently applied also in numerical studies

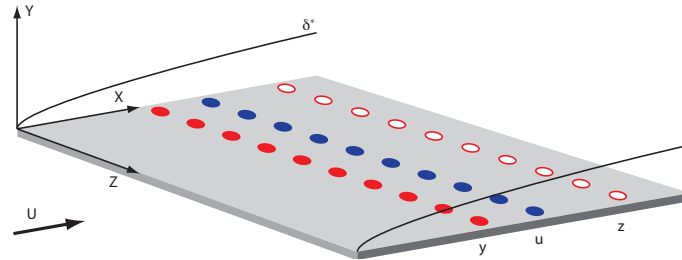


FIGURE 26. Control configuration for a three dimensional (3D) flow developing over a flat plate. A possible configuration consists of localized sensors and actuators placed along the spanwise direction.

(Huang & Kim 2008; Hervé *et al.* 2012). Indeed, for linear systems, it can be shown that projection-based techniques and system identification techniques can provide equivalent reduced-order models (Ma *et al.* 2011). We refer the reader to the reviews by (Bagheri & Henningson 2011) and (Sipp & Schmid 2013) for a broader overview.

Control of three-dimensional disturbances. A sketch of the three-dimensional control setup of the flow over a flat-plate is shown Figure 26. Compared to the 2D boundary-layer flow a single actuator u , sensor y and output z are now replaced by arrays of elements localized along the span-wise direction, resulting in a multi-input multi-output (MIMO) system. The localization (size and distance between elements) of sensors and actuators may significantly influence efficiency of the compensator (Semeraro *et al.* 2011, 2013). An important question one must address for MIMO systems is how to connect inputs to outputs. A first approach consists of coupling one actuator with only one sensor (for instance, the one upstream); in this case, the number of single-input single-output (SISO) *control units* equals the number of sensor/actuator pairs. This approach is called *decentralized* control-design; despite its simplicity in practical implementations, the stability in closed loop is not guaranteed (Glad & Ljung 2000). The dual approach where only one control-unit is designed and all the sensors are coupled to all the available actuators is called *centralized* control. In Semeraro *et al.* (2011), the centralized-controller strategy was found necessary for the design of a stable TS-wave controller. The main drawback of a fully centralized-control approach is that the number of connections for a flat plate of large span quickly becomes impractical due to all the wiring. One may then introduce a *semi-decentralized* controller, where small MIMO control-units are designed and connected to each other; in Dadfar *et al.* (2014), it is shown that a number of control-units can efficiently replace a full centralized control with a limited loss of performance.

Another important aspect that has been accounted for in a MIMO setting, is the choice of the objective function z . The minimization of a set of signals

obtained from localized outputs with compact support does not necessarily correspond to a reduction of the actual perturbation amplitude in a global sense. For 1D and 2D flow systems any measurement taken locally, close to the solid wall and downstream in the computational domain, is sufficient for obtaining consistency between the perturbation and signal minimization (Bagheri *et al.* 2009*b*); this is not the case for 3D systems. An optimal way for choosing the output \mathbf{C}_z is the *output projection* suggested by Rowley (2005), where a projection on a POD basis is performed. The resulting signal $z(t)$ corresponds to the amplitude coefficients of the POD modes, i.e. the temporal behaviour of the most energetic coherent structure of the flow. This method can also provide useful guidelines for the location of output sensors.

7. Summary and conclusions

This work provides a comprehensive review on standard model-based techniques (LQR, Kalman filter, LQG, MPC) and model-free techniques (LMS, X-filtered LMS) for the delay of the transition from laminar to turbulence. We have focussed on the control of perturbation evolving in convective flows, using the linearized Kuramoto-Sivashinsky equation as a model of the flow over the flat-plate to characterize and compare these techniques. Indeed, this model provides the two important traits of convectively unstable fluid systems, namely, the amplifying behaviour of a stable system and a very large time delay.

Much research have been performed on flow control using the very elegant techniques based on LQR and LQG (Bagheri *et al.* 2009*c*; Semeraro *et al.* 2013; Julliet *et al.* 2013). Although, these techniques may lead to the best possible performance and they have stability guarantees (under certain restrictions), their implementation in experimental flow control settings raises a number obstacles: (1) The choice of actuator and sensor placement that yields a good performance of convectively unstable systems results in a feedforward system. We have highlighted the robustness issues arising from this configuration when using standard LQG-based techniques. (2) Disturbances, such as free-stream turbulence, and actuators, such as plasma actuators, can be difficult to model under realistic conditions. (3) The requirement of solving two Riccati equations is a major computational hassle, although it has successfully been addressed by the community using model-order reduction techniques (Bagheri *et al.* 2009*b*) or iterative methods (Semeraro *et al.* 2013).

Model-free techniques based on classical system-identification methods or adaptive-noise-cancellation techniques can cope with the limitations of model-based methods (Sturzebecher & Nitsche 2003). For example, we have presented algorithms that improve robustness by adapting to varying and un-modelled conditions. However, model-free techniques have their own limitations; (i) one may often encounter instabilities, which in contrast to LQR/LQG, cannot always be addressed in a straight-forward manner by using concepts such as controllability and observability. (ii) The number of free parameters (such as

the limits of the sums appearing in FIR filters) that need to be modelled are many and chosen in a somewhat *ad-hoc* manner.

The conclusion is that there does not exist one single method that is able to deal with all issues, and the final choice depends on the particular conditions that must be addressed. While a model-based technique may provide optimality and physical insight, it may lack the robustness to uncertainties that adaptive methods are able to provide. We believe that future research will head towards hybrid methods, where controllers are partially designed using numerical simulations and partially using adaptive experiment-based techniques.

Acknowledgement

The authors acknowledge support the Swedish Research Council (VR-2012-4246, VR-2010-3910) and the Linné Flow Centre.

Appendix A. Numerical method

Finite-difference (FD) schemes are used to approximate the spatial derivatives in (12). In particular, a centered scheme based on stencils of five-nodes are used for the second-order and fourth-order derivatives while a one-node-backward scheme is used for the first-order derivative. The latter is required due to the convective nature of the system: a de-centered scheme reduces the spurious, numerical oscillation of the approximated solution (Quarteroni 2009).

The grid is equispaced $x_i = i \frac{L}{n_v}$, with $i = 1, 2, \dots, n_v$. Once the FD scheme is introduced, the time evolution at each of the internal node is solution of the ODE equation

$$\begin{aligned} \frac{dv'(t)}{dt} = & -V \sum_{j=-3}^1 d_{1,j}^b v'_{i+j}(t) - \frac{\mathcal{P}}{\mathcal{R}} \sum_{l=-2}^2 d_{2,l}^c v'_{i+l}(t) + \\ & - \frac{1}{\mathcal{R}} \sum_{l=-2}^2 d_{4,l}^c v'_{i+l}(t) + b_d(x_i) d(t) + b_u(x_i) u(t), \end{aligned} \quad (95)$$

where $v'_i(t) = v'(x_i, t)$ for $i = 1, 2, \dots, n_v$. The outflow boundary conditions in (10) on the right boundary of the domain lead to the linear system of equations,

$$\left. \frac{\partial v'}{\partial x} \right|_{x=L} = 0 \quad \Rightarrow \quad \sum_{j=-3}^1 d_{1,j}^b v'_{n_v+j}(t) = 0 \quad (96)$$

$$\left. \frac{\partial^3 v'}{\partial x^3} \right|_{x=L} = 0 \quad \Rightarrow \quad \sum_{j=-2}^2 d_{3,j}^c v'_{n_v+j}(t) = 0 \quad (97)$$

The solution of this system allows us to express the boundary nodes $i = n_v + 1, n_v + 2$ as a linear combination of the inner nodes. Similarly, the left boundary

condition in (11) leads to an expression for the nodes $i = 0, -1$:

$$v'|_{x=0} = 0 \Rightarrow v'_0(t) = 0 \quad (98)$$

$$\frac{\partial v'}{\partial x}\bigg|_{x=0} = 0 \Rightarrow \sum_{j=-1}^3 d_{1,j}^f v'_{0+j}(t) = 0 \quad (99)$$

where a forward FD scheme is used for the first-order derivative approximation. Equation (95) together with the boundary conditions can be rewritten in compact form as

$$\dot{\mathbf{v}}(t) = \mathbf{A} \mathbf{v}(t) + \mathbf{B}_d d(t) + \mathbf{B}_u u(t)$$

where $\mathbf{B}_d = \{b_d(x_i)\}$, $\mathbf{B}_u = \{b_u(x_i)\}$ and the matrix $\mathbf{A} \in \mathbb{R}^{n_v \times n_v}$ is a banded matrix (see also (18)).

The Crank-Nicolson method is used to march the system forward in time (18). Given a time step Δt , the value of the state $\mathbf{v}(t + \Delta t)$ is given by the expression:

$$\mathbf{v}(t + \Delta t) = \mathbf{CN}_I^{-1} [\mathbf{CN}_E \mathbf{v}(t) + \Delta t (\mathbf{B}_d d(t) + \mathbf{B}_u u(t))] \quad (100)$$

where $\mathbf{CN}_I = \mathbf{I} - \frac{\Delta t}{2} \mathbf{A}$ and $\mathbf{CN}_E = \mathbf{I} + \frac{\Delta t}{2} \mathbf{A}$. This is an implicit method, i.e. requires the solution of the linear system \mathbf{CN}_I^{-1} , and this operation can be numerically expensive.

Appendix B. Numerical code

A downloadable package of the MATLAB routines used to produce the results presented in this paper can be found at <http://www.mech.kth.se/nicolo/ks/>. The 11 scripts listed below cover all the methods that are presented in this work.

`script00.m`: Time evolution of a spatially localized initial condition. The time response of the plant to a Gaussian-shaped initial condition is calculated: the generated wave-packet travels downstream while growing and is detected by the outputs y and z . The spatio-temporal time evolution of $v(x, t)$ is plotted together with the output signals.

`script01.m`: Response to a white Gaussian disturbance $d(t)$. A white noise signal is considered as input $d(t)$ and the time-response of the plant is calculated. The statistics of the velocity are computed and visualized for comparison with the controlled cases.

`script02.m`: External description. An alternative description of the system, based on the Input/Output behaviour of the system is calculated. In particular, the response of the system is calculated via a FIR filter and compared with the LTI system description, i.e. internal description.

`script03.m`: Controllability and observability Gramians. The controllability and observability Gramians are computed solving the Lyapunov equations in (33–34).

78 *N. Fabbiane, O. Semeraro, S. Bagheri & D. S. Henningson*

`script04.m`: Linear-Quadratic Regulator. A LQR controller is applied to the plant and tested when the system is excited by a white Gaussian noise $d(t)$. The statistics of the velocity are computed and visualized in order to be compared to the other controlled cases.

`script05.m`: Model Predictive Control. Constrained MPC is used in presence of saturation of the actuator. The system is excited by a white Gaussian noise $d(t)$. The statistics of the velocity are computed and visualized in order to be compared with the other controlled cases.

`script06.m`: Kalman filter. A Kalman filter is designed for the plant and used to estimate the system state when excited by a white Gaussian noise $d(t)$.

`script07.m`: Least-Mean Square filter. A LMS filter is used to identify the FIR-kernel E_{zy} . The resulting kernel is compared with the Kalman filter solution.

`script08.m`: Linear-Quadratic Gaussian compensator. A LQG compensator is designed coupling a LQR controller and a Kalman filter. The compensator is tested when the system is excited by a white Gaussian noise $d(t)$.

`script09.m`: $P - \tau$ compensator. A simple opposition control is designed using explicitly the time-delay. The system is excited by a white Gaussian noise $d(t)$. The control gain has been obtained by a trial and error procedure.

`script10.m`: Filtered-X Least-Mean Square algorithm. FXLMS algorithm is implemented. The initial condition is provided by the impulse response of the corresponding LQG compensator; a robustness test is carried by displacing the actuator location.

Following functions are required by the above scripts:

`[A,x,I] = KS_init(nq)`. Given the number of degree of freedom n_v , it provides the state matrix \mathbf{A} obtained by a FD discretization of the spatial derivatives. Five grid-point stencil FD schemes are used: in particular, a one grid point de-centered scheme is used to enhance the stability of the numerical solution.

`d = fd_coeff(n,dx)`. It provides the FD coefficients used by `KS_init`.

References

- AKERVIK, E., HEPFFNER, J., EHRENSTEIN, U. & HENNINGSON, D. S. 2007 Optimal Growth, Model Reduction and Control in a Separated Boundary-layer Flow Using Global Eigenmodes. *J. Fluid Mech.* **579**, 305–314.
- AKHTAR, I., BORGGAARD, J., STOYANOV, M. & ZIETSMAN, L. 2010 On Commutation of Reduction and Control: Linear Feedback Control of a von Kármán Street. In *5th Flow Control Conference*, pp. 1–14. American Institute of Aeronautics and Astronautics.
- ANDERSON, B. & LIU, Y. 1989 Controller Reduction: Concepts and Approaches. *IEEE Trans. Autom. Control* **34**, 802–812.
- ANDERSON, B. & MOORE, J. 1990 *Optimal control: Linear Quadratic Methods*. Prentice Hall, New York.
- ARNOLD, W. I. & LAUB, A. 1984 Generalized eigenproblem algorithms and software for algebraic Riccati equations. *Proceedings of the IEEE* **72** (12), 1746–1754.
- ASTRÖM, K. J. & WITTENMARK, B. 1995 *Adaptive Control*, 2nd edn. Addison Wesley.
- BAGHERI, S., BRANDT, L. & HENNINGSON, D. S. 2009a Input–output analysis, model reduction and control of the flat-plate boundary layer. *J. Fluid Mech.* **620** (1), 263–298.
- BAGHERI, S. & HENNINGSON, D. S. 2011 Transition delay using control theory. *Philos. Trans. R. Soc.* **369**, 1365–1381.
- BAGHERI, S., HEPFFNER, J., SCHMID, P. J. & HENNINGSON, D. S. 2009b Input-Output Analysis and Control Design Applied to a Linear Model of Spatially Developing Flows. *Appl. Mech. Rev.* **62**.
- BAMIEH, B., PAGANINI, F. & DAHLEH, M. 2002 Distributed control of spatially invariant systems. *IEEE Trans. Autom. Control* **47** (7), 1091–1107.
- BANKS, H. T. & ITO, K. 1991 A numerical algorithm for optimal feedback gains in high dimensional linear quadratic regulator problems. *SIAM J. Control and Optimization* **29** (3), 499–515.
- BARBAGALLO, A., SIPP, D. & SCHMID, P. J. 2009 Closed-loop control of an open cavity flow using reduced order models. *J. Fluid Mech.* **641**, 1–50.
- BELSON, B. A., SEMERARO, O., ROWLEY, C. W. & HENNINGSON, D. S. 2013 Feedback control of instabilities in the two-dimensional Blasius boundary layer: The role of sensors and actuators. *Phys. Fluids* **25**.
- BENNER, P. 2004 Solving Large-Scale Control Problems. *IEEE Contr. Sys.* **24** (1), 44–59.
- BENNER, P., LI, J. & PENZL, T. 2008 Numerical solution of large-scale Lyapunov equations, Riccati equations, and linear-quadratic optimal control problems. *Numer. Linear Algebra Appl.* **15**, 755–777.
- BEWLEY, T. R. 2001 Flow Control: New Challenges for a New Renaissance. *Progr. Aerospace Sci.* **37**, 21–58.
- BEWLEY, T. R. & LIU, S. 1998 Optimal and Robust Control and Estimation of Linear Paths to Transition. *J. Fluid Mech.* **365**, 305–349.

- 80 *N. Fabbiane, O. Semeraro, S. Bagheri & D. S. Henningson*
- BEWLEY, T. R., MOIN, P. & TEMAM, R. 2001 DNS-based predictive control of turbulence: an optimal benchmark for feedback algorithms. *J. Fluid Mech.* **447** (1), 179–225.
- BOYD, S. & VANDENBERGHE, L. 2004 *Convex optimization*. Cambridge university press.
- BRYD, R. H., HRIBAR, M. E. & NOCEDAL, J. 1999 An Interior Point Algorithm for Large-Scale Nonlinear Programming. *SIAM Journal on Optimization* .
- BUSHNELL, D. M. & MOORE, K. J. 1991 Drag Reduction in Nature. *Ann. Rev. Fluid Mech.* **23** (65–79).
- CHARRU, F. 2011 *Hydrodynamic Instabilities*, 1st edn. Cambridge.
- CHEVALIER, M., HËPFFNER, J., AKERVIK, E. & HENNINGSON, D. S. 2007a Linear Feedback Control and Estimation Applied to Instabilities in Spatially Developing Boundary Layers. *J. Fluid Mech.* **588**, 163–187.
- CHEVALIER, M., HËPFFNER, J., BEWLEY, T. R. & HENNINGSON, D. S. 2006 State Estimation in Wall-bounded Flow Systems. Part 2: Turbulent Flows. *J. Fluid Mech.* **552**, 167–187.
- CHEVALIER, M., SCHLATTER, P., LUNDBLADH, A. & HENNINGSON, D. S. 2007b A pseudo-spectral solver for incompressible boundary layer flows. *Tech. Rep. TRITA-MEK 2007:07*. KTH Mechanics, Stockholm, Sweden.
- CHOI, H., MOIN, P. & KIM, J. 1994 Active Turbulence Control for Drag Reduction in Wall-bounded Flows. *J. Fluid Mech.* **262**, 75–110.
- COLEMAN, T. F. & LI, Y. 1996 A reflective Newton method for minimizing a quadratic function subject to bounds on some of the variables. *SIAM Journal on Optimization* **6** (4), 1040–1058.
- COLLIS, S. S., JOSLIN, R. D., SEIFERT, A. & THEOFILIS, V. 2004 Issues in active flow control: theory, control, simulation, and experiment. *Progr. Aerospace Sci.* **40** (4), 237–289.
- CORBETT, P. & BOTTARO, A. 2001 Optimal control of nonmodal disturbances in boundary layers. *Theoretical and Computational Fluid Dynamics* **15** (2), 65–81.
- CORKE, T. C., ENLOE, C. L. & WILKINSON, S. P. 2010 Dielectric Barrier Discharge Plasma Actuators for Flow Control. *Ann. Rev. Fluid Mech.* **42** (1), 505–529.
- CORTELEZZI, L., SPEYER, J. L., LEE, K. H. & KIM, J. 1998 Robust Reduced-Order Control of Turbulent Channel Flows via Distributed Sensors and Actuators. *IEEE 37th Conf. on Decision and Control* pp. 1906–1911.
- CVITANOVIĆ, P., ARTUSO, R., MAINIERI, R., TANNER, G. & VATTAY, G. 2012 Turbulence? In *Chaos: Classical and Quantum*, chap. 4. Niels Bohr Institute, Copenhagen, <http://ChaosBook.org/version14>.
- DADFAR, R., FABBIANE, N., BAGHERI, S. & HENNINGSON, D. S. 2014 Centralised versus Decentralised Active Control of Boundary Layer Instabilities. *Flow, Turb. and Comb.* .
- DOYLE, J. C. 1978 Guaranteed Margins for LQG Regulators. *IEEE Trans. Autom. Control* **AC-23** (4), 756–757.
- DOYLE, J. C., GLOVER, K., KHARGONEKAR, P. P. & FRANCIS, B. A. 1989 State-Space Solutions to Standard H_2 and H_∞ Control Problems. *IEEE Trans. Autom. Control* **34**, 831–847.
- ELLIOTT, S. & NELSON, P. 1993 Active noise control. *Signal Processing Magazine, IEEE* **10** (4), 12–35.

Adaptive and Model-Based Control Th. Applied to Conv. Unst. Flows 81

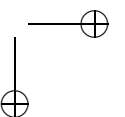
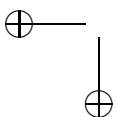
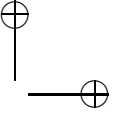
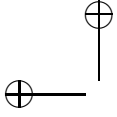
- ERDMANN, R., PÄTZOLD, A., ENGERT, M., PELTZER, I. & NITSCHKE, W. 2012 On active control of laminar-turbulent transition on two-dimensional wings. *Philos. Trans. R. Soc.* **369**, 1382–1395.
- GARCIA, C. E., PRETT, D. M. & MORARI, M. 1989 Model Predictive Control: Theory and Practice – A Survey. *Automatica* **25** (3), 335–348.
- GLAD, T. & LJUNG, L. 2000 *Control Theory*. London: Taylor & Francis.
- GOLDIN, N., KING, R., PÄTZOLD, A., NITSCHKE, W., HALLER, D. & WOIAS, P. 2013 Laminar Flow Control With Distributed Surface Actuation: Damping Tollmien-Schlichting Waves with Active Surface Displacement. *Exp. Fluids* **54** (3), 1–11.
- GRUNDMANN, S. & TROPEA, C. 2008 Active Cancellation of Artificially Introduced Tollmien-Schlichting Waves using Plasma Actuators. *Exp. Fluids* **44** (5), 795–806.
- GUNZBURGER, M. 2003 *Perspectives in Flow Control and Optimization*. SIAM.
- EL HAK, M. G. 1996 Modern Developments in Flow Control. *Appl. Mech. Rev.* **49**, 365–379.
- EL HAK, M. G. 2007 *Flow control: passive, active, and reactive flow management*. Cambridge University Press.
- HAYKIN, S. 1986 *Adaptive Filter Theory*. Prentice-Hall.
- HERVÉ, A., SIPP, D., SCHMID, P. J. & SAMUELIDES, M. 2012 A physics-based approach to flow control using system identification. *J. Fluid Mech.* **702**, 26–58.
- HÖGBERG, M. & BEWLEY, T. R. 2000 Spatially Localized Convolution Kernels for Feedback Control of Transitional Flows. *IEEE 39th Conf. on Decision and Control* **3278–3283**.
- HÖGBERG, M., BEWLEY, T. R. & HENNINGSON, D. S. 2003a Linear Feedback Control and Estimation of Transition in Plane Channel Flow. *J. Fluid Mech.* **481**, 149–175.
- HÖGBERG, M., BEWLEY, T. R. & HENNINGSON, D. S. 2003b Relaminarization of $Re_\tau = 100$ Turbulence Using Gain Scheduling and Linear State-feedback Control Flow. *Phys. Fluids* **15**, 3572–3575.
- HUANG, S. & KIM, J. 2008 Control and system identification of separated flow. *Phys. Fluids* **20**, 101509.
- HUERRE, P. & MONKEWITZ, P. A. 1990 Local and Global Instabilities in Spatially Developing Flows. *Ann. Rev. Fluid Mech.* **22**, 473–537.
- ILAK, M., BAGHERI, S., BRANDT, L., ROWLEY, C. W. & HENNINGSON, D. S. 2010 Model Reduction of the Nonlinear Complex Ginzburg-Landau Equation. *SIAM J. Appl. Dyn. Sys.* **9** (4), 1284–1302.
- ILAK, M. & ROWLEY, C. W. 2008 Modeling of Transitional Channel Flow Using Balanced Proper Orthogonal Decomposition. *Phys. Fluids* **20**, 034103.
- JACOBSON, S. A. & REYNOLDS, W. C. 1998 Active control of streamwise vortices and streaks in boundary layers. *J. Fluid Mech.* **360**, 179–211.
- JOSHI, S. S., SPEYER, J. L. & KIM, J. 1997 A Systems Theory Approach to the Feedback Stabilization of Infinitesimal and Finite-amplitude Disturbances in Plane Poiseuille Flow. *J. Fluid Mech.* **332**, 157–184.
- JOVANOVIĆ, M. R. & BAMIEH, B. 2005 Componentwise Energy Amplification in Channel Flows. *J. Fluid Mech.* **534**, 145–183.
- JULLIET, F., SCHMID, P. J. & HUERRE, P. 2013 Control of amplifier flows using subspace identification techniques. *J. Fluid Mech.* **725**, 522–565.

82 *N. Fabbiane, O. Semeraro, S. Bagheri & D. S. Henningson*

- KIM, J. & BEWLEY, T. R. 2007 A Linear Systems Approach to Flow Control. *Ann. Rev. Fluid Mech.* **39**, 39–383.
- KRIEGSEIS, J. 2011 Performance Characterization and Quantification of Dielectric Barrier Discharge Plasma Actuators. PhD thesis, TU Darmstadt.
- KURAMOTO, Y. & TSUZUKI, T. 1976 Persistent Propagation of Concentration Waves in Dissipative Media Far from Thermal Equilibrium. *Progr. Theoretical Physics* **55** (2), 356–369.
- LEE, K. H., CORTELEZZI, L., KIM, J. & SPEYER, J. 2001 Application of Reduced-order Controller to Turbulent Flow for Drag Reduction. *Phys. Fluids* **13**, 1321–1330.
- LEWIS, F. L. & SYRMOUS, L. V. 1995 *Optimal Control*. John Wiley & Sons, New York.
- LJUNG, L. 1999 *System identification*. Wiley Online Library.
- LUENBERGER, D. G. 1979 *Introduction to Dynamic System*. John Wiley & Sons, New York.
- LUNDELL, F. 2007 Reactive control of transition induced by free-stream turbulence: an experimental demonstration. *J. Fluid Mech.* **585**, 41–71.
- MA, Z., AHUJA, S. & ROWLEY, C. W. 2011 Reduced-order models for control of fluids using the eigensystem realization algorithm. *Theoretical and Computational Fluid Dynamics* **25** (1-4), 233–247.
- MANNEVILLE, P. 1995 *Dissipative structures and weak turbulence*. Springer.
- MARTENSSON, K. & RANTZER, A. 2011 Synthesis of structured controllers for large-scale systems. *IEEE Trans. Autom. Control* .
- MCKEON, B. J., SHARMA, A. S. & JACOBI, I. 2013 Experimental manipulation of wall turbulence: A systems approach. *Phys. Fluids* **25** (3), –.
- MILLING, R. W. 1981 Tollmien–Schlichting wave cancellation. *Phys. Fluids* **24**, 979.
- MONOKROUSOS, A., BRANDT, L., SCHLATTER, P. & HENNINGSON, D. S. 2008 DNS and LES of estimation and control of transition in boundary layers subject to free-stream turbulence. *Intl J. Heat and Fluid Flow* **29** (3), 841–855.
- MOORE, B. 1981 Principal Component Analysis in Linear Systems: Controllability, Observability, and Model reduction. *IEEE Trans. Autom. Control* **26** (1), 17–32.
- NOACK, B. R., AFANASIEF, K., MORZYNSKI, M., TADMOR, G. & THIELE, F. 2003 A hierarchy of low-dimensional models for the transient and post-transient cylinder wake . *J. Fluid Mech.* **497**, 335–363.
- NOACK, B. R., MORZYNSKI, M. & TADMOR, G. 2011 *Reduced-Order Modelling for Flow Control*, , vol. 528. Springer Verlag.
- PENROSE, R. 1955 A generalized inverse for matrices. *Mathematical Proceedings of the Cambridge Philosophical Society* **51**, 406–413.
- PRALITS, J. O. & LUCHINI, P. 2010 Riccati-less optimal control of bluff-body wakes. In *Seventh IUTAM Symposium on Laminar-Turbulent Transition* (ed. P. Schlatter & D. S. Henningson), , vol. 18. Springer.
- PRESS, W. H., TEUKOLSKY, S. A., VETTERLING, W. T. & FLANNERY, B. P. 2007 *Numerical Recipes 3rd Edition: The Art of Scientific Computing*, 3rd edn. Cambridge University Press.
- QIN, S. J. & BADGWELL, T. A. 2003 A Survey of Industrial Model Predictive Control Technology. *Contr. Eng. Pract.* **11** (7), 733–764.
- QUARTERONI, A. 2009 *Numerical Models for Differential Problems*. Springer.

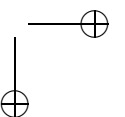
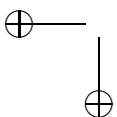
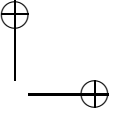
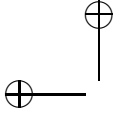
Adaptive and Model-Based Control Th. Applied to Conv. Unst. Flows 83

- RATHNASINGHAM, R. & BREUER, K. S. 2003 Active control of turbulent boundary layers. *J. Fluid Mech.* **495**, 209–233.
- ROWLEY, C. W. 2005 Model reduction for fluids, using balanced proper orthogonal decomposition. *Intl J. of Bifurcation and Chaos* **15** (03), 997–1013.
- SARIC, W. S., REED, H. L. & KERSCHEN, E. J. 2002 Boundary-layer Receptivity to Freestream Disturbances. *Ann. Rev. Fluid Mech.* **34** (1), 291–319.
- SCHLICHTING, H. & GERSTEN, K. 2000 *Boundary-Layer Theory*. Springer Verlag, Heidelberg.
- SCHMID, P. J. 2007 Nonmodal Stability Theory. *Ann. Rev. Fluid Mech.* **39**, 129–62.
- SCHMID, P. J. & HENNINGSON, D. S. 2001 *Stability and Transition in Shear Flows. Applied Mathematical Sciences* v. 142. Springer-Verlag.
- SEMERARO, O., BAGHERI, S., BRANDT, L. & HENNINGSON, D. S. 2011 Feedback control of three-dimensional optimal disturbances using reduced-order models. *J. Fluid Mech.* **677**, 63–102.
- SEMERARO, O., BAGHERI, S., BRANDT, L. & HENNINGSON, D. S. 2013a Transition delay in a boundary layer flow using active control. *J. Fluid Mech.* **731** (9), 288–311.
- SEMERARO, O., PRALITS, J. O., ROWLEY, C. W. & HENNINGSON, D. S. 2013b Riccati-less approach for optimal control and estimation: an application to two-dimensional boundary layers. *J. Fluid Mech.* **731**, 394–417.
- SIEGEL, S. G., SIEGEL, J., FAGLEY, C., LUCHTENBURG, D. M., COHEN, K. & MCLAUGHLIN, T. 2008 Low Dimensional Modelling of a Transient Cylinder Wake Using Double Proper Orthogonal Decomposition. *J. Fluid Mech.* **610**, 1–42.
- SIPP, D., MARQUET, O., MELIGA, P. & BARBAGALLO, A. 2010 Dynamics and Control of Global Instabilities in Open-Flows: a Linearized Approach. *Appl. Mech. Rev.* **63** (3), 30801.
- SIPP, D. & SCHMID, P. J. 2013 Closed-Loop Control of Fluid Flow: a Review of Linear Approaches and Tools for the Stabilization of Transitional Flows. *Aerospace-Lab Journal*.
- SIVASHINSKY, G. I. 1977 Nonlinear Analysis of Hydrodynamic Instability in Laminar Flames – I. Derivation of Basic Equations. *Acta Astronautica* **4**, 1177–1206.
- SKOGESTAD, S. & POSTLETHWAITE, I. 2005 *Multivariable Feedback Control, Analysis to Design*, 2nd edn. Wiley.
- STURZEBECHER, D. & NITSCHKE, W. 2003 Active cancellation of Tollmien–Schlichting instabilities on a wing using multi-channel sensor actuator systems. *Intl J. Heat and Fluid Flow* **24**, 572–583.
- SUZEN, Y., HUANG, P., JACOB, J. & ASHPIS, D. 2005 Numerical Simulations of Plasma Based Flow Control Applications. *AIAA J.* **4633**, 2005.
- ZHOU, K., DOYLE, J. C. & GLOVER, K. 2002 *Robust and Optimal Control*. Prentice Hall, New Jersey.



Paper 2

2



On the Role of Adaptivity for Robust Laminar Flow Control

By Nicolò Fabbiane¹, Bernhard Simon², Felix Fischer²,
Sven Grundmann², Shervin Bagheri¹ & Dan S. Henningson¹

¹ Linné FLOW Centre, KTH Mechanics, S-100 44 Stockholm, Sweden

² Center of Smart Interfaces, TU Darmstadt, 64347 Griesheim, Germany

To be submitted to *J. Fluid Mech.*

In boundary-layer flows, it is possible to reduce the friction drag by attenuating the amplitude of local flow instabilities – Tollmien-Schlichting waves – that growing may onset the laminar-to-turbulent transition. In this work, adaptive and model-based techniques are compared in controlling the growth of these disturbances in a zero-pressure-gradient two-dimensional boundary-layer flow. In particular, it is shown how the adaptivity (i.e. the capacity to adapt to the real flow conditions) is necessary to effectively control the laminar flow in real applications or, in general, in those situations where a perfect repeatability of the flow condition is not possible. A dielectric-barrier-discharge plasma actuator is used to perform the control action, based on the measurement by surface hot-wires. A linear model of the flow is build based on direct numerical simulations simulations of the experiment in order to design a Linear Quadratic Gaussian (LQG) regulator. The resulting model-based compensator is compared with an adaptive Filtered-X Least Mean Square (FXLMS) algorithm. The sensitivity of the compensator performance to disturbances amplitude and changes in the free-stream conditions are investigated. In particular, the LQG regulator is found to be very sensitive to model inaccuracies, showing incapable to prescribe the correct phase information to the actuator when strong variations of the free-stream velocity occur. Moreover, by a performance comparison at design condition, FXLMS control action is shown to be close to the optimal solution guaranteed by LQG approach.

1. Introduction

Avoiding the transition from a laminar to a turbulent regime in the boundary-layer region is one technique to reduce the friction drag in wall-bounded flows. In a low-turbulence environment the transition is dominated by the exponential growth of flow instabilities - Tollmien Schlichting (TS) waves - that eventually break down to turbulence (Saric *et al.* 2002). However, it has been shown that is possible to attenuate the growth of these instabilities by manipulating the flow and eventually delay the onset of the turbulent regime. In this framework, two

possible strategies can be adopted to pursue this aim. (i) The mean-flow can be conveniently modified by passive (Shahinfar *et al.* 2014) or active (Duchmann *et al.* 2013) devices in order to elude or control the onset of the instability itself. (ii) The upcoming wave can be detected by suitable sensors and cancelled by an targeted forcing on the flow: this technique requires a smaller amount of power, since the control action is limited to counteract the upcoming wave (Bewley & Liu 1998; Bagheri *et al.* 2009b; Goldin *et al.* 2013). The core of this control framework is to design a compensator, i.e. the system that, given the on-line measurements of the flow, computes a suitable forcing to reduce the amplitude of the upcoming wave.

One of the first attempts to design a compensator in order to delay the laminar-to-turbulent transition was presented by Bewley & Liu (1998). Optimal and robust control theory were used to precompute the compensator based on a Linear-Time-Invariant (LTI) system that describes the time evolution of the disturbances in the flow. This and the guaranteed optimality of the control action lead this control technique to fast spread in the numerical community (Barbagallo *et al.* 2009; Bagheri *et al.* 2009b; Semeraro *et al.* 2013) and reached the experimental level (Juillet *et al.* 2014, via identified models of the flow). Because in this class of methods the compensator is precomputed off-line based on a model of the flow and then applied to the experimental/numerical set-up, the compensator that results is *static*, i.e. its control law is constant in time.

Parallel to these numerical studies, the experimental community started to use adaptive control techniques (e.g. Sturzebecher & Nitsche 2003; Kurz *et al.* 2013). Unlike the previous approach, the control law is not precomputed but it is identified on-line by the compensator itself: in fact, it is able to learn how to properly control the flow by monitoring a measurement of its performances. Less modelling of the flow response is needed to perform the control action, but no optimality of the control action is guaranteed.

The aim of this work is to compare these two different design approaches and assess their advantages and limitations: a Linear Quadratic Gaussian (LQG) regulator (Bagheri *et al.* 2009b) and a Filtered X Least Mean Square (FXLMS) filter (Sturzebecher & Nitsche 2003) are chosen as representative respectively of static and adaptive compensators class. To our knowledge, this is the first time that an LQG compensator based on DNS simulations of the flow is applied to an experimental setup.

2. Experimental set-up

A 2D TS wave is generated by a disturbance source (d) in a flat-plate boundary-layer flow and is detected farther downstream by a surface hot-wire (y), see Figure 1. This sensor provides the reference signal to the compensator to compute the control action and a dielectric barrier discharge (DBD) plasma actuator (u) provides the prescribed forcing on the flow. A second surface hot-wire sensor (z) is positioned downstream of the actuator to evaluate the compensator performance.

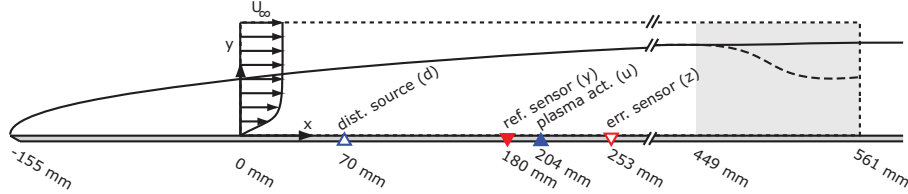


FIGURE 1. Experimental set-up. The computational domain used in the DNS simulations (dashed line) starts at $(x, y) = (0, 0)$ and it extends $750 \delta_0^*$ in streamwise direction and $30 \delta_0^*$ in the wall-normal direction, where $\delta_0^* = 0.748$ mm is the displacement thickness at the beginning of the domain. In the last part of the domain (grey area) a fringe region enforces the periodicity along the streamwise direction (Nordström *et al.* 1999).

The experiments are conducted in an open-circuit wind tunnel at TU Darmstadt, which provides a $450 \text{ mm} \times 450 \text{ mm}$ test section and an averaged turbulence intensity of $Tu = 0.1\%$, measured at the end of the 1:24 contraction nozzle. A 1,600 mm long flat plate with an 1:6 elliptical leading edge and adjustable trailing edge is mounted horizontally in the middle of the test section. Figure 1 shows a sketch of the flat plate containing surface mounted sensors, the disturbance source and the plasma actuator. The zero position is chosen to be 70 mm upstream of the disturbance source as the DNS computational box starts at this point.

A dSPACE system consisting of a DS1006 processor board, a DS2004 A/D board as well as a DS2102 high resolution D/A Board provides the computational power for the flow control algorithm. An additional 16bit NI PCI 6254 A/D board is used for data acquisition of hot wire sensors signals as well as the disturbance source signals.

Disturbances are created by pressure fluctuations at the wall, caused by conventional loudspeakers. This method is a widely used method for exciting TS waves (Borodulin *et al.* 2002; Würz *et al.* 2012). The disturbance source consists of 16 Visaton BF 45 speakers, amplified by 16 Kemo M031N, which can be controlled individually by the 16 channels analog output module NI9264. The set of loudspeakers is placed outside of the testsection and 1.2 m long tubes are led into the testsection from below the flat plate. The tubes are arranged along a line in spanwise direction beneath a 0.2 mm wide slot in the flat plate surface. An outer tube diameter of 3 mm gives a total width of the disturbance source of 240 mm. Two spanwise rows of 30 Sennheiser KE 4-211-2 microphones enable the on-line monitoring of the phase and amplitude of the artificially excited TS waves in order to assure an even 2D wave front. The first row is positioned upstream of the plasma actuator at $x = 164$ mm while the second row downstream of the plasma actuator at $x = 224$ mm. All microphones are

mounted below the surface and are connected to the surface through a 0.2 mm circular orifice with a spacing of only 9 mm in spanwise direction. All channels are sampled by two NI 9205 A/D converter modules with 4 kHz.

In addition, a boundary-layer hot wire probe Dantec 55P15 is mounted on a 2D traverse for phase-averaged boundary layer measurements. The DC signal is filtered with an 1 kHz low pass filter to avoid aliasing.

2.1. Actuator and sensors for flow-control

The flow control device for this experiment, the plasma actuator, consists of a 10 mm wide grounded lower electrode of 35 μm thickness and a 5 mm wide upper electrode, which are divided in the vertical direction by five layers of Kapton tape with a total thickness of 0.3 mm. A GBS Minipuls 2.1 high voltage supply is driving the 230 mm long plasma actuator, which is installed flush mounted to a spanwise groove in order to minimize roughness of the surface.

The plasma actuator driving frequency f_{PA} is chosen to be 10 kHz, which is more than one order of magnitude higher than the unstable TS wave frequency band for this experiment. In order to assure a stable discharge in time and space, an operation range from $V = 5 \text{ kV}_{pp}$ to 13 kV_{pp} has to be maintained for this actuator design (Barckmann 2014): therefore a mean voltage supply $V = 7 \text{ kV}_{pp}$ is chosen for all experiments. The compensator can modulate the amplitude of the high voltage supply via the control signal $u(t)$ and, as consequence, vary the plasma actuator force on the time scale of the TS waves. The control signal $u(t)$, fed into the high voltage generator, is a linearized function with respect to the plasma actuator force at that working point.

Two surface hot-wires sensors are used to provide the compensator the required information to compute a suitable control signal $u(t)$. Introduced by Sturzebecher & Nitsche (2003) the surface hot-wire has proven to be an excellent sensor type for reactive flow control (Lundell 2007; Goldin *et al.* 2013). Due to the high electromagnetic interference of the plasma actuator, a classic hot-wire design with prongs is preferred and modified to serve as a surface hot-wire. Two conventional needles are moulded in a plastic case, which can be flush mounted on the flat plate. A small groove between the needle tips avoids heat loss to the structure and improves the signal to noise ratio. The 5 μm thin and 1.25 mm long gilded-tungsten wire is heated with an overheat ratio of 1.7. Due to shielded signal lines, this sensor is less sensitive for electromagnetic interferences than the conventional surface hot-wire design based on photo-etched printed circuit boards. A 4 channels Dantec Streamline constant temperature anemometer (CTA) provides the band pass filtered AC signal of the sensors (10 Hz – 1 kHz). All hot wire sensor signals are acquired with an sample rate of 10 kHz. The surface hot-wires are calibrated for quantifying the TS wave amplitude according to the definition in (2). The calibration was conducted by exciting 2D TS waves whose maximum amplitude was measured above the surface hot-wire using the traversable boundary-layer hot-wire probe as a reference.

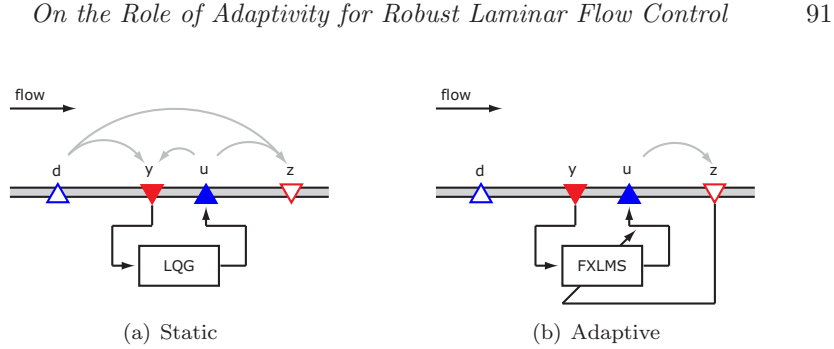


FIGURE 2. Compensator schemes for static (LQG) and adaptive (FXLMS) strategies. The measurements by the error sensor z are used by the FXLMS algorithm to adapt to the current flow conditions. The grey lines indicate the I/O relations required to be modelled by each strategy.

3. Static and adaptive compensator

The compensators is the dynamical systems that takes the measurements as inputs and gives the control action as output (Figure 2). In this work a linear compensator is considered, i.e. the compensator is described by a system of linear ordinary differential equations (ODE) in time. It can be either represented by its state-space formulation or by its Input/Output (I/O) relations (Glad & Ljung 2000). The latter representation is chosen: hence, the compensator response is described by a Finite Impulse Response (FIR) filter that reads (Haykin 1986)

$$u(n) = \sum_{i=1}^{N_k} K(i) y(n-i) \quad (1)$$

where $u(n) = u(n \Delta t)$ and $y(n) = y(n \Delta t)$ are the time-discrete representation of the time-continuous signals $u(t)$ and $y(t)$ and $\Delta t = 1 \text{ ms}$ is the sampling time. The N_K coefficients $K(i)$ are the kernel of the filter and they describe how the compensator filters the measurements $y(n)$ in order to provide the control action $u(n)$.

In this framework, two compensator classes can be identified by whether their kernel is static or adaptive. The former strategy consists in precomputing the control law usually relying on a model of the controlled system (*plant*): the model can be either identified from experimental measurements (Juillet *et al.* 2014) or based on DNS simulations of the flow (e.g. Bewley & Liu 1998; Bagheri *et al.* 2009b). In an adaptive compensator, instead, control action and kernel design are simultaneous: the kernel coefficients $K(i)$ are updated on-line by the compensator itself relying on a on-line measurements of its performances.

In this work, these two control strategies are compared. A Linear Quadratic Gaussian (LQG) regulator is chosen as representative of the static compensator

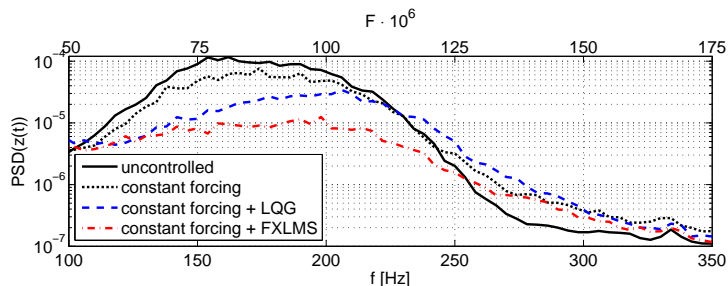


FIGURE 3. Experimental time-averaged Power Spectral Density (PSD) functions for $z(t)$. The flow is excited by a white-noise signal $d(t)$. The top axis reports the non-dimensional frequency $F = (2\pi\nu/U_\infty^2) f$. The Reynolds number at error sensor location is $Re_{x,z} = 375 \cdot 10^3$

class (Figure 1.2(a)). The compensator design is based on two separated optimisation procedures based on a full model of the plant (Glad & Ljung 2000). The first optimally estimates the actual conditions in the flow from the measurements $y(t)$. The second, computes the optimal control action $u(t)$ from the estimated state. The time-discrete response of the resulting Linear Time Invariant (LTI) system to an impulse $y(t)$ gives the convolution kernel $K(i)$ in (1). A Filtered-X Least-Mean-Squares (FXLMS) algorithm, instead, represents the class of adaptive compensators (Sturzebecher & Nitsche 2003; Engert *et al.* 2008). As reported in Figure 1.2(b), it uses the measurement signal of the error sensor $z(t)$ to dynamically adapt itself to the actual condition of the flow, given a model of the I/O relation $u \rightarrow z$ between the plasma actuator and the error sensor. If the flow conditions are constant, the compensator kernel asymptotically converge to stable sub-optimal solution. For both the control techniques, refer to Fabbiane *et al.* (2014) for more detailed information.

Figure 3 reports the performances of the two compensators when the disturbance source is fed with a white-noise signal $d(t)$ for a wind tunnel speed $U_{WT} = 12 \text{ m/s}$. The solid line depicts the time-averaged spectrum of $z(t)$ for the uncontrolled case: as the signal $z(t)$ is a measure of the wall-stress fluctuations, it is related to the amplitude of the TS wave-packets that are generated by the disturbance $d(t)$. This results in a TS-wave band that ranges from 100 Hz to 250 Hz, as predicted by local stability theory (Schmid & Henningson 2001). The dashed and dot-dashed lines depict the z -signal spectra when the LQG and FXLMS compensators are applied: the FXLMS algorithm appears to be more effective than the LQG regulator. As mentioned in §2.1, the plasma actuator is operated at a mean high voltage $V = 7 \text{ kV}_{pp}$, corresponding to an average specific-power consumption of $P = 16 \text{ W/m}$. The resulting constant forcing is small enough to have only a marginal stabilizing effect on the flow, as it is shown by the dotted line in Figure 3.

4. A DNS model of the flow

In order to provide a model for the LQG design, numerical simulations are designed to simulate the flow in the test section. The experimental set-up described in §2, produces a 2D perturbation in a 2D boundary layer that are small enough not to trigger non-linear phenomena. The linearised Navier-Stokes (NS) equations around a laminar zero-pressure-gradient boundary-layer flow are considered to describe the temporal evolution of the disturbances. The free-stream velocity $U_\infty = 14$ m/s and the displacement thickness in the beginning of the domain $\delta_0^* = 0.748$ mm are identified by a parameter fitting procedure of the laminar solution over 10 measured mean-velocity profiles between $x = 0$ mm and $x = 330$ mm. The resulting Reynolds number is $Re = \frac{U_\infty \delta_0^*}{\nu} = 656$. A pseudo-spectral DNS code is used to perform the simulations (Chevalier *et al.* 2007). Fourier expansion over $N_x = 768$ modes is used to approximate the solution along the streamwise direction, while Chebyshev expansion is used in the wall-normal direction on $N_y = 101$ Gauss-Lobatto collocation points. The computational domain is shown in Figure 1.

The disturbance source and the plasma actuator are modelled by volume forcings. Each forcing term is decomposed in a constant spatial shape and in a time dependent part, i.e. the input signals. The forcing shape for the disturbance source is a synthetic vortex localized at the disturbance source position (Bagheri *et al.* 2009b). The plasma actuator shape, instead, is modelled by a distributed streamwise forcing, according to the results by Kriegseis *et al.* (2013). As the forcing shape is dependent by the high-voltage supply to the actuator, a linearisation around $V = 7$ kV_{pp} is considered. The surface hot-wires sensors $y(t)$ and $z(t)$ are modelled as point-wise measurements of the skin-friction fluctuations.

Simulated and measured performance of the LQG compensator are reported in Figure 4. The flow is excited by a single-frequency constant-amplitude signal $d(t)$ with frequency $f_d = 200$ Hz. The amplitude of the velocity fluctuation in the flow is measured by an hot-wire probe mounted on a traverse system. A non-dimensional measure for the TS-wave amplitude is introduced:

$$A_{TS,int}(x) = \frac{1}{\delta_0^*} \int_0^\infty \frac{|\mathcal{U}(x, y, f_d)|}{U_\infty} dy = \frac{1}{\delta_0^*} \int_0^\infty A_{TS}(x, y) dy \quad (2)$$

where $\mathcal{U}(x, y, f)$ is the Fourier transform of the streamwise component of the velocity. In Figure 1.4(a) $A_{TS,int}(x)$ is reported for the LQG-controlled (blue dashed line) and uncontrolled case (black solid line). The simulated uncontrolled case matches very well the experimental data (black circles). The blue dashed line depicts the simulated perturbation amplitude when the LQG control is applied: the attenuation is overestimated respect the experimental data (blue squares). The performance prediction is improved if the average constant forcing by the plasma actuator is considered when computing the baseflow used for testing the compensator (green dotted line). This indicates a small difference between the modelling and the experiments. In Figure 4(b-c) the

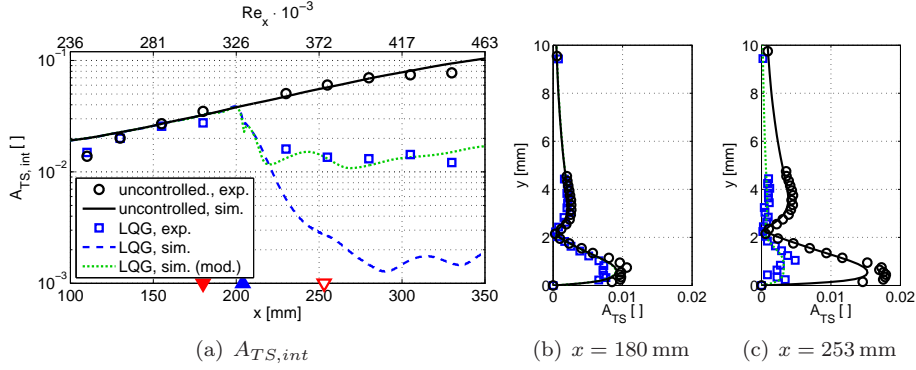


FIGURE 4. TS-wave amplitude for $f_d = 200$ Hz. Lines and circles depict simulated and experimental data respectively. (a) shows the integral TS-wave amplitude ($A_{TS,int}$) as a function of the streamwise position. The top $i_{i\frac{1}{4}}$ axis reports $Re_x = \frac{(x-x_{LE})U_\infty}{\nu}$, where x_{LE} is the leading-edge position. (b) and (c) show the TS-wave shape at two different x positions upstream and downstream the actuator. The triangles indicate where the reference sensor, plasma actuator, and error sensor are positioned, cfr. Figure 1.

controlled and uncontrolled cases are compared where the reference sensor y and the error sensor z are positioned. From Figure 1.4(c), the disturbance appears to be damped all along the wall-normal direction, both in simulation (green dotted line) and experiment (blue squares). A double-peak shape is visible near the wall that can be explained by the proximity to the plasma actuator. In fact, the lower peak of the TS amplitude is located at the wall-normal position where Kriegseis *et al.* (2013) measured the maximum forcing of a similar plasma actuator. However, as the controlled TS-wave evolves further downstream it shows a less pronounced double peak structure.

5. Robustness

In this section, the robustness of the two control techniques is analysed. Here, *robustness* means the capacity of the compensator to overcome the unavoidable differences between design and working condition. In particular, effects by amplitude of the disturbances and changes in the free-stream conditions are investigated. The ratio between the root-mean-square (rms) of $z(t)$ signal of the controlled and uncontrolled case

$$Z = \frac{\text{rms}(z_{ctr}(t))}{\text{rms}(z_{unctr}(t))} \quad (3)$$

is used as performance index of the control strategy.

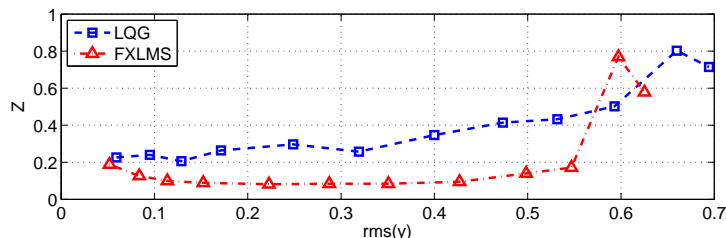


FIGURE 5. Effect of the TS-wave amplitude on the performance indicator Z . The flow is excited by the disturbance source operated with a 200 Hz single-frequency signal.

5.1. TS-wave amplitude

A 200 Hz single-frequency disturbance is used to investigate the robustness of the LQG controller against higher TS-wave amplitude with forcing frequency $f_d = 200$ Hz. The amplitude is gradually increased and the rms of the reference sensor signal $y(t)$ is used as an indicator of disturbance amplitude. In Figure 5, it can be seen how controller performance is gradually degraded while the amplitude rises and it reaches a saturation beyond $rms(y) = 0.6$. The FXLMS compensator, instead, is able to maintain good performance until an abrupt breakdown of the performances around $rms(y) = 0.6$, when the compensator adaptivity can not compensate any more the non-linearities in the flow.

5.2. Free-stream velocity (Reynolds number)

Unexpected changes of the free stream conditions may also degrade the control performance: they modify the baseflow on which NS equations are linearised, introducing a modelling error that may lead to a performance loss for the compensator. To investigate this condition, the compensator performance is monitored while the wind-tunnel speed is varied around the design condition $U_{WT} = 12 \text{ m/s}^2$, changing the Reynolds number and, as a consequence, the stability properties of the flow (Schmid & Henningson 2001). A white-noise disturbance $d(t)$ is considered and the disturbance is monitored in order to ensure a 2D wave-front. The ratio between $rms(y)$ and the wind-tunnel speed U_{WT} is kept constant and equal to $6.5 \cdot 10^{-3}$ in order to avoid non-linear effects.

Figure 1.6(a) reports the performance index Z as a function of the wind-tunnel speed variation ΔU_{WT} . LQG performance varies as the speed is changed, showing a strong dependence to Reynolds number variations (blue dashed line). In particular, the best performance is obtained for a velocity lower than the design speed. This shift is due to repeatability issues of the experiments: even if speed and length are fixed, unavoidable daily fluctuations of the viscosity cause a shift of the actual Reynolds number of the flow. The

²Note that the asymptotic velocity U_∞ differs from U_{WT} because of blockage effects due to the presence of the flat-plate and experimental equipment.

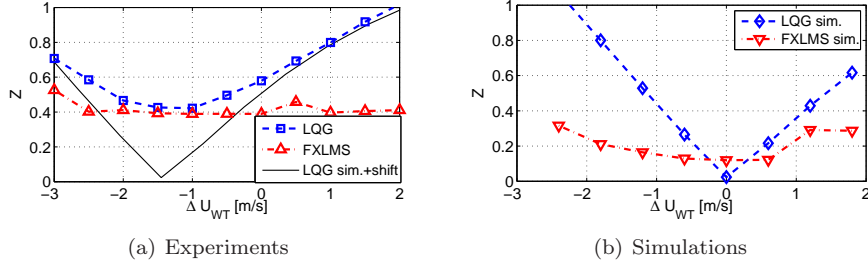


FIGURE 6. Effect of wind-tunnel speed variation ΔU_{WT} on the performance indicator Z . The solid line in (b) depicts the DNS data shifted to fit the experimental curve. The flow is excited by the disturbance source operated with a white noise signal $d(t)$.

FXLMS compensator, instead, is able to adapt to the changed condition. Even if the required I/O relation $u \rightarrow z$ is changed by the speed variation, the adaptive nature of the compensator is able to neutralise this error and ensure almost unaltered performances for all the investigated wind-tunnel speeds. These robustness results are also confirmed by the DNS data in Figure 1.6(b): as in the experiment, the free-stream velocity is varied respect to the design condition and the performance of the control action is monitored.

The simulations data give also a better insight about the optimality of the control action by the FXLMS compensator. At the design condition $\Delta U_{WT} = 0$, simulation and design model of the flow coincide: the attenuation achieved by the FXLMS algorithm is very close to the optimal solution guaranteed by the LQG regulator in this condition. The same observation can be also done starting from the experimental data. If the simulated LQG performances are reported in Figure 1.6(a) and a proper shift is applied (solid black line), they asymptotically approach the experimental data (blue dashed line): it can be thus claimed that the minimum showed by the LQG experimental data represents an experimental-optimal solution. Once again, the FXLMS performance is close to the optimal one. These numerical and experimental observations show that the control action performed by the FXLMS compensator is not far from the optimal solution.

Having observed that the performance of LQG regulator is significantly reduced compared to FXLMS compensator in off-design conditions, an explanation of this observation is provided. The signal $z(t)$ can be seen as the superposition of the two counter-phase TS-waves one generated by the disturbance source and one by the plasma actuator. Consider the single harmonic case for simplicity:

$$z(t) = z_d(t) + z_u(t) = a \sin(\omega(t + \Delta\tau)) - a \sin(\omega t). \quad (4)$$

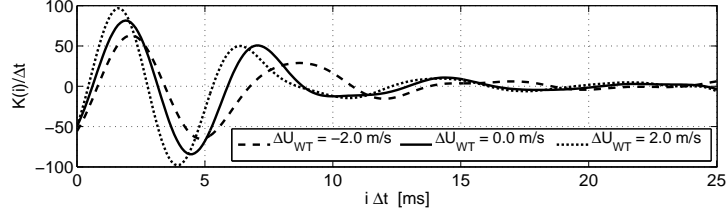


FIGURE 7. FXLMS kernels $K(i)$ for different wind-tunnel speeds. The solid line represents the design condition. When U_{WT} decreases (dashed line) or increases (dotted line), the compensator adapts to the new conditions by stretching or shrinking the compensator kernel.

If a velocity variation occurs, $z_d(t)$ experiences a phase-shift $\Delta\tau$ due to a change in the phase-speed of the TS-wave. The expression in (4) can be manipulated in order to highlight the role of $\Delta\tau$:

$$z(t) = 2a \sin\left(\omega \frac{\Delta\tau}{2}\right) \cos\left(\omega \left(t - \frac{\Delta\tau}{2}\right)\right) \approx a\omega\Delta\tau \cos\left(\omega \left(t - \frac{\Delta\tau}{2}\right)\right). \quad (5)$$

For small values of $\omega\Delta\tau$, the amplitude of $z(t)$ is linear with the phase shift $\Delta\tau$. Moreover, considering for small velocity variation the phase-shift linear with ΔU_{WT} , (5) explains the linear dependence between the performance index Z and the speed variation.

Figure 7 compares the experimental FXLMS kernels for a positive and a negative ΔU_{WT} to the design condition (solid line). A lower wind-tunnel speed (dashed line) has two effects on the flow: (i) the amplification of the TS wave is reduced and (ii) the time scales in the flow increase, i.e. the TS wave moves slower than under design conditions. The compensator reacts to these new conditions by stretching the convolution kernel in time and reducing the magnitude of the $K(i)$ coefficients. On the other hand, if the speed increases (dotted line), the effect on the flow is opposite: the TS wave moves faster and it is more amplified by the flow. Hence, the FXLMS algorithm reacts by shrinking the kernel and increasing the magnitude of the $K(i)$ coefficients.

The time τ where the minimum occurs in the convolution kernel is an indicator of the phase-shift prescribed by the compensator. Figure 8 shows a strong correlation between the phase-shift $|\Delta\tau| = |\tau_{LQG} - \tau_{FXLMS}|$ between the two compensator kernels and the performance loss ΔZ , i.e the gap between the two curves in Figure 6. This correlation further supports the idea that the compensator performances are mainly depending on a correct prediction of the phase-shift of the TS wave between the reference-sensor and plasma-actuator position. In the LQG approach, this information is given by the design-model: any inaccuracy in this model may lead to an incorrect computation of the phase-shift and, eventually, to a performance loss.

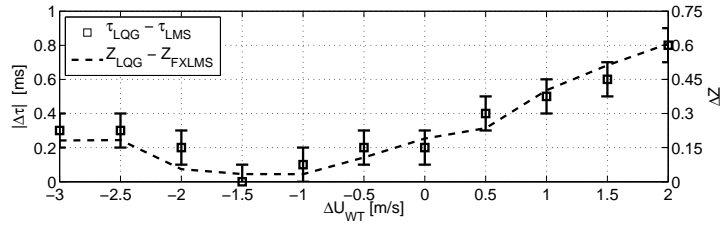


FIGURE 8. Correlation between phase error $|\Delta\tau|$ (squares) and performance loss ΔZ (dashed line) when the wind-tunnel speed is changed. An error $\pm\Delta t$ equal to the sampling-time is considered for $\Delta\tau$.

6. Conclusions

Adaptivity emerges to be crucial for laminar-flow control in real applications.

The optimal performances guaranteed by the model-based approach is shown not able hold against the on-line tailored response of the adaptive techniques when it comes to modelling errors. As shown in §5, the performances of the LQG compensator are strongly dependent on free-stream velocity variations. An adaptive controller, instead, adjusts its response to the new condition and prescribe the correct forcing to the actuator. In fact, the investigated FXLMS compensator is able to adapt to the new free-stream velocity and ensures almost constant performances for a wide range of speed variations.

Moreover, DNS and experimental data show that the control action performed by the FXLMS algorithm is close to the optimal solution guaranteed by the LQG regulator when no modelling error occurs.

Concluding, a static compensator is confined to those applications where a very accurate model of the flow is available and adaptive control is recommended for laminar-flow control in real environments.

The authors acknowledge support the Swedish Research Council (VR-2012-4246, VR-2010-3910) and the Linné Flow Centre.

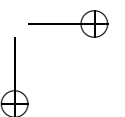
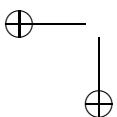
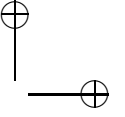
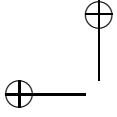
References

- BAGHERI, S., BRANDT, L. & HENNINGSON, D. S. 2009 Input–output analysis, model reduction and control of the flat-plate boundary layer. *J. Fluid Mech.* **620** (1), 263–298.
- BARBAGALLO, A., SIPP, D. & SCHMID, P. J. 2009 Closed-loop control of an open cavity flow using reduced order models. *J. Fluid Mech.* **641**, 1–50.
- BARCKMANN, K. 2014 Active Vortex Generation using Dielectric Barrier Discharge Plasma Actuators in Laminar Boundary Layers. PhD thesis, Technischen Universität Darmstadt.
- BEWLEY, T. R. & LIU, S. 1998 Optimal and Robust Control and Estimation of Linear Paths to Transition. *J. Fluid Mech.* **365**, 305–349.
- BORODULIN, V. I., KACHANOV, Y. S. & KOPTSEV, D. B. 2002 Experimental Study of Resonant Interactions of Instability Waves in Self-Similar Boundary Layer with an Adverse Pressure Gradient: II. Detuned Resonances*. *Journal of Turbulence* **3** (062).
- CHEVALIER, M., SCHLATTER, P., LUNDBLADH, A. & HENNINGSON, D. S. 2007 A pseudo-spectral solver for incompressible boundary layer flows. *Tech. Rep. TRITA-MEK 2007:07*. KTH Mechanics, Stockholm, Sweden.
- DUCHMANN, A., GRUNDMANN, S. & TROPEA, C. D. 2013 Delay of Natural Transition with Dielectric Barrier Discharges. *Exp. Fluids* **54** (3), 1–12.
- ENGERT, M., PÄTZOLD, A., BECKER, R. & NITSCHKE, W. 2008 Active cancellation of tollmien-schlichting instabilities in compressible flows using closed-loop control. In *IUTAM Symposium on Flow Control and MEMS*, , vol. 7, pp. 319–331. Springer Netherlands.
- FABBIANE, N., SEMERARO, O., BAGHERI, S. & HENNINGSON, D. S. 2014 Adaptive and Model-Based Control Theory Applied to Convectively Unstable Flows. *Appl. Mech. Rev.* **66** (6), 060801.
- GLAD, T. & LJUNG, L. 2000 *Control Theory*. London: Taylor & Francis.
- GOLDIN, N., KING, R., PÄTZOLD, A., NITSCHKE, W., HALLER, D. & WOIAS, P. 2013 Laminar Flow Control With Distributed Surface Actuation: Damping Tollmien-Schlichting Waves with Active Surface Displacement. *Exp. Fluids* **54** (3), 1–11.
- HAYKIN, S. 1986 *Adaptive Filter Theory*. Prentice-Hall.
- JUILLET, F., MCKEON, B. J. & SCHMID, P. J. 2014 Experimental Control of Natural Perturbations in Channel Flow. *J. Fluid Mech.* **752**, 296–309.
- KRIEGSEIS, J., SCHWARZ, C., TROPEA, C. & GRUNDMANN, S. 2013 Velocity-Information-Based Force-Term Estimation of Dielectric-Barrier Discharge Plasma Actuators. *J. Phys. D* **46** (5), 055202.
- KURZ, A., GOLDIN, N., KING, R., TROPEA, C. D. & GRUNDMANN, S. 2013 Hybrid Transition Control Approach for Plasma Actuators. *Exp. Fluids* **54** (11), 1–4.
- LUNDELL, F. 2007 Reactive control of transition induced by free-stream turbulence: an experimental demonstration. *J. Fluid Mech.* **585**, 41–71.
- NORDSTRÖM, J., NORDIN, N. & HENNINGSON, D. 1999 The fringe region technique and the Fourier method used in the direct numerical simulation of spatially evolving viscous flows. *SIAM J. Sci. Comp.* **20** (4), 1365–1393.

- SARIC, W. S., REED, H. L. & KERSCHEN, E. J. 2002 Boundary-layer Receptivity to Freestream Disturbances. *Ann. Rev. Fluid Mech.* **34** (1), 291–319.
- SCHMID, P. J. & HENNINGSON, D. S. 2001 *Stability and Transition in Shear Flows. Applied Mathematical Sciences* v. 142. Springer-Verlag.
- SEMERARO, O., PRALITS, J. O., ROWLEY, C. W. & HENNINGSON, D. S. 2013 Riccati-less approach for optimal control and estimation: an application to two-dimensional boundary layers. *J. Fluid Mech.* **731**, 394–417.
- SHAHINFAR, S., SATTARZADEH, S. S. & FRANSSON, J. H. M. 2014 Passive Boundary Layer Control of Oblique Disturbances by Finite-Amplitude Streaks. *J. Fluid Mech.* **749**, 1–36.
- STURZEBECKER, D. & NITSCHKE, W. 2003 Active cancellation of Tollmien–Schlichting instabilities on a wing using multi-channel sensor actuator systems. *Intl J. Heat and Fluid Flow* **24**, 572–583.
- WÜRZ, W., SARTORIUS, D., KLOKER, M., BORODULIN, V. I., KACHANOV, Y. S. & SMORODSKY, B. V. 2012 Nonlinear Instabilities of a Non-Self-Similar Boundary Layer on an Airfoil: Experiments, DNS, and Theory. *Euro. J. Mech. B* **31**, 102–128.

Paper 3

3



Centralised versus Decentralised Active Control of Boundary Layer Instabilities

By **Reza Dadfar**¹, **Nicolò Fabbiane**¹, **Shervin Bagheri**¹ & **Dan S. Henningson**¹

¹ Linné FLOW Centre, KTH Mechanics, S-100 44 Stockholm, Sweden

Flow, Turbulence and Combustion. Published on-line.

We use linear control theory to construct an output feedback controller for the attenuation of small-amplitude three-dimensional Tollmien-Schlichting (TS) wavepackets in a flat-plate boundary layer. A three-dimensional viscous, incompressible flow developing on a zero-pressure gradient boundary layer in a low Reynolds number environment is analyzed using direct numerical simulations. In this configuration, we distribute evenly in the spanwise direction up to 72 localized objects near the wall (18 disturbances sources, 18 actuators, 18 estimation sensors and 18 objective sensors). In a fully three-dimensional configuration, the interconnection between inputs and outputs becomes quickly infeasible when the number of actuators and sensors increases in the spanwise direction. The objective of this work is to understand how an efficient controller may be designed by connecting only a subset of the actuators to sensors, thereby reducing the complexity of the controller, without comprising the efficiency. If n and m are the number of sensor-actuator pairs for the whole system and for a single control unit, respectively, then in a decentralised strategy, the number of interconnections decreases mn compared to a centralized strategy, which has n^2 interconnections. We find that using a semi-decentralized approach – where small *control units* consisting of 3 estimation sensors connected to 3 actuators are replicated 6 times along the spanwise direction – results only in a 11% reduction of control performance. We explain how “wide” in the spanwise direction a control unit should be for a satisfactory control performance. Moreover, the control unit should be designed to account for the perturbations that are coming from the lateral sides (crosstalk) of the estimation sensors. We have also found that the influence of crosstalk is not as essential as the spreading effect.

1. Introduction

Drag reduction methodologies in vehicles and aircrafts have received considerable attention during the past decades (Thomas 1984). These techniques

provide the possibility to significantly reduce the operational cost in transportation sector and also improve the environmental consequences. In boundary layer flows, drag reduction can be achieved by extending the laminar region on the aerodynamics parts of vehicles by delaying the transition from laminar to turbulence. Although, different techniques are used to delay the transition, currently significant efforts are devoted to active control strategies *e.g.* opposition control (Hammond *et al.* 1998), wave cancellation (Sturzebecher & Nitsche 2003), optimal controller (Dadfar *et al.* 2013) and etc. This approach adds external energy to the system in terms of predetermined actuation (open loop) or on-line computation of the actuation law using feedback information from the measurement sensors (reactive control). One particular reactive control strategy employed in this study is output feedback control (Doyle *et al.* 1989), where the actuation is determined by measuring external disturbances.

In an environment characterised by low turbulence levels, two-dimensional perturbations – Tollmien-Schlichting (TS) – wavepackets are triggered inside the boundary layer. The TS waves grow exponentially in amplitude as they move downstream until a point where nonlinear effects are significant and transition to turbulence is triggered. An important trait of this transition scenario, which also enables the use of linear control theory, is that the initial stage of the perturbation growth inside the boundary layer is well described by a linear system. Moreover, due to the large sensitivity of such flows to an external excitation, one can influence the TS waves by introducing small local perturbation in small region of the flow via proper localised devices requiring minute energy. There is now substantial literature where linear control theory is combined with numerical simulations to control transition in wall-bounded flows. Pioneering work include the control of Orr-Sommerfeld equations (Joshi *et al.* 1997), distributed control using convolution kernels (Cortelezzi *et al.* 1998; Högberg *et al.* 2003) and a localised control approach (Dadfar *et al.* 2013; Bagheri *et al.* 2009*b*). The term *localized* in the latter approach refers to the use of a limited number of small compact actuation and estimation devices positioned in specific manner to allow efficient control. The fact that the number of inputs/outputs ($\mathcal{O}(10)$) is order of magnitudes smaller than the dimensions of flow system ($\mathcal{O}(10^7)$) provides amenable conditions for reducing the order of the system by constructing a low-dimensional model (ROM). Here, we report on our most advanced configuration (placing up to 72 inputs/outputs) so far. In order to have a physically realizable configuration, our numerical system is chosen as to resemble the experimental study performed by Li & Gaster (2006). This investigation extends or complements our previous work on two-dimensional disturbances using blowing/suction and shear stress measurements (Bagheri *et al.* 2009*a*), three-dimensional linear (Semeraro *et al.* 2011) and non-linear (Semeraro *et al.* 2013) investigations. Relevant reviews on this subject are provided in Bewley (2001), Kim & Bewley (2007) and Bagheri & Henningson (2011).

We will report on the efficiency of a centralised and a decentralised control strategy (Glad & Ljung 2000; Lewis & Syrmos 1995). In the former approach all the sensors are connected to all the actuators. Since the complexity of a controller is related to the number of interconnections, this approach becomes infeasible when reaching $\mathcal{O}(10^2)$ inputs and outputs. This is certainly a restrictive issue, since in a localized control approach the number of required sensors and actuators increase with the span of the plate. A solution to this restriction is a decentralised controller where one disregards some of the interconnections which are not essential to the dynamics of the system. Then one replicates the same controller (called control unit) along the span of the system to cover a larger spanwise distance. In this study, several different control units are designed and their performances are compared.

2. Flow and Control Configuration

2.1. Governing equations

The dynamics and control of small-amplitude perturbations in a viscous, incompressible flow developing over an unswept flat plate are investigated using direct numerical simulation (DNS). The disturbance dynamics is governed by the Navier-Stokes equation linearised around a spatially developing zero-pressure-gradient boundary layer flow as

$$\frac{\partial u}{\partial t} = -(U \cdot \nabla)u - (u \cdot \nabla)U - \nabla p + \frac{1}{Re} \nabla^2 u + \lambda_f(x)u, \quad (1a)$$

$$\nabla \cdot u = 0, \quad (1b)$$

$$u = u_0 \quad \text{at} \quad t = t_0, \quad (1c)$$

where the disturbance velocity and pressure fields are denoted by $u(x, y, z, t)$ and $p(x, y, z, t)$; x , y and z denote the streamwise, wall normal and spanwise direction, respectively. Furthermore, $U(x, y)$ and $P(x, y)$ represent the baseflow velocity and pressure; they are a solution to the steady, nonlinear Navier-Stokes equation. In this study, all the spatial coordinates are normalised with the displacement thickness δ^* at the inlet of the computational box. The Reynolds number is defined based on the displacement thickness as $Re = U_\infty \delta^* / \nu$ where the U_∞ denotes the uniform free stream velocity and ν is the kinematic viscosity; all the simulations are performed at $Re = 915$ which correspond to a distance of $312\delta^*$ from the origin of the plate to the inlet of the computational box. The no-slip boundary condition is considered at the wall ($y = 0$), while Dirichlet boundary condition with vanishing velocity is employed at the upper boundary ($y = L_y$); this boundary condition is applied far enough from the boundary layer to ensure negligible influence on the dynamics of the perturbations. Periodicity is assumed in the spanwise and streamwise directions. In the latter, the term $\lambda(x)$ is implemented to enforce this periodicity so that a spectral Fourier expansion technique can be employed. The function $\lambda(x)$ is zero

inside the physically relevant part of the domain where the dynamics are investigated and has nonzero value at the end of the domain where a fringe region is applied (Nordström *et al.* 1999). The simulation is performed using a pseudo-spectral DNS code (Chevalier *et al.* 2007) where Fourier series are employed in the wall-parallel directions and the wall-normal direction is expanded in Chebyshev polynomials. The computational domain $\Omega = (0, 500) \times (0, 30) \times (0, 162)$ is discretized with $384 \times 101 \times 128$ grid points in x, y and z directions, respectively. The time integration is performed using a Crank-Nicolson scheme for the linear terms and a third order Runge-Kutta method for the advective terms (Chevalier *et al.* 2007). The time step is $0.4\delta^*/U_\infty$ for the current simulations.

2.2. Input-Output System

A schematic representation of the input-output configuration is depicted in Figure 1. The linearised Navier-Stokes equation with inputs and outputs can be written in state space form as

$$\dot{u}(t) = Au(t) + B_1w(t) + B_2\phi(t), \quad (2a)$$

$$v(t) = C_2u(t) + \alpha g(t), \quad (2b)$$

$$z(t) = \begin{pmatrix} C_1 \\ 0 \end{pmatrix} u(t) + \begin{pmatrix} 0 \\ R^{1/2} \end{pmatrix} \phi(t). \quad (2c)$$

Henceforth, $u(t) \in \mathbb{R}^n$ denotes the state vector, whereas $w(t) \in \mathbb{R}^d, \phi(t) \in \mathbb{R}^m, v(t) \in \mathbb{R}^p, g(t) \in \mathbb{R}$ and $z(t) \in \mathbb{R}^k$ denote time signals. The matrix $A \in \mathbb{R}^{n \times n}$ represents the linearised and spatially discretised Navier-Stokes equation. The above form has been reported in numerous works (see e.g. Semeraro *et al.* (2010)) and only a short description is provided here:

- The first input ($B_1w(t)$) is composed of $B_1 \in \mathbb{R}^{n \times d}$ representing the spatial distribution of d localised disturbances located at the upstream end of the domain and white noise signals $w(t) \in \mathbb{R}^d$. These inputs represent a model of perturbations introduced inside the boundary layer by e.g. roughness and free-stream perturbations.
- In the second input ($B_2\phi(t)$), $B_2 \in \mathbb{R}^{n \times m}$ represents the spatial support of m actuators located inside the boundary layer near the wall. They are fed by the control signal $\phi(t) \in \mathbb{R}^m$, which is to be determined by an appropriate controller.
- The p output measurement provided by $v(t) \in \mathbb{R}^p$ detect information about the travelling structures by the localised sensors $C_2 \in \mathbb{R}^{p \times n}$. These measurements are corrupted by $\alpha g(t)$. More precisely, $g(t) \in \mathbb{R}^p$ is a white noise signal and α the level of noise.
- The output $z(t) \in \mathbb{R}^k$ extracts information from the flow in order to evaluate the performance of the controller. This is done by localised outputs $C_1 \in \mathbb{R}^{k \times n}$ with a spatial distribution located far downstream in the computational box. It also contains the weighted control input. In fact, the minimisation of the output signal detected by C_1 is the

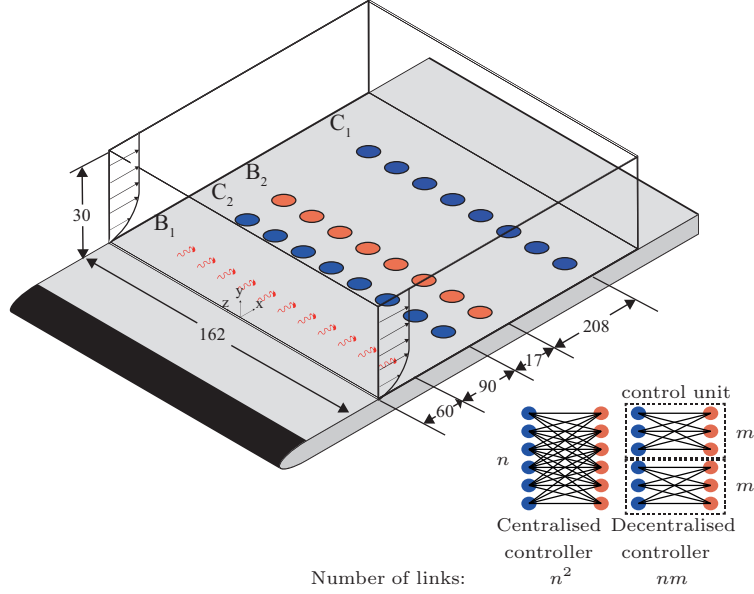


FIGURE 1. Input-output configuration of the system. The input B_1 is a row of localised disturbances located at $x = 60$, convected downstream and converted to a TS wavepacket. The control action is provided by the input B_2 , consists of a row of actuators located at $x = 167$. A set of localised estimation sensors, at $x = 150$ upstream of the actuator is employed. A row of output sensors at $x = 375$ is implemented as the objective function of the controller. Two control strategies, centralised and decentralised are used. In the former all the sensors and actuators are wired together while in the latter, a control unit with a limited interconnections is designed and replicated along the span. There are in total 18 disturbances B_1 , 18 sensors C_2 , 18 actuators B_2 and 18 outputs C_1 . Only 8 of those are depicted in the figure. For a centralised controller with n sensor-actuator pairs, the connections are n^2 while in a decentralised controller, each control unit contains m sensor-actuator pairs, the connections are nm .

objective of our LQG controller; the aim is to find a control signal $\phi(t)$ able to attenuate the amplitude of the disturbance detected by C_1 . Hence, the objective function reads

$$\|z\|_{L^2_{[0,\infty]}}^2 = \mathcal{E} \{ u^T C_1^T C_1 u + \phi^T R \phi \}, \quad (3)$$

where $\mathcal{E}(\cdot)$ is the expectation operator. The matrix $R \in \mathbb{R}^{m \times m}$ contains the control penalty l^2 in each diagonal entry and represents the expense

Element	Symbol	Number	Location	Parameters
—	—		(x_0, y_0)	$(\sigma_x, \sigma_y, \sigma_z)$
Disturbances	B_1	18	(60, 0)	(6, 1.5, 8)
Sensors	C_2	18	(150, 0)	(2, 1.5, 2)
Actuators	B_2	18	(167, 0)	(6, 1.5, 8)
Outputs	C_1	18	(375, 0)	(5, 1.5, 6)

TABLE 1. The main parameters characterising the spatial distribution of the sensors and the actuators. All the elements are located at $z_0 = -76.5$ and distributed along the span with the spanwise spacing $\Delta_z = 9$.

of the control. This parameter is introduced as a regularisation term accounting for physical restrictions. Large values of control penalty results in weak actuation and creates low amplitude control signal whereas low values of control penalty leads to strong actuation.

Following Semeraro *et al.* (2011), we define the spatial distribution of the sensors and actuators with a Gaussian divergence-free function as

$$h(x, y, z) = a \begin{pmatrix} \sigma_x \gamma_y \\ -\sigma_y \gamma_x \\ 0 \end{pmatrix} e^{-\gamma_x^2 - \gamma_y^2 - \gamma_z^2}, \quad (4)$$

where

$$\gamma_x = \frac{x - x_0}{\sigma_x}, \quad \gamma_y = \frac{y - y_0}{\sigma_y}, \quad \gamma_z = \frac{z - z_0}{\sigma_z}, \quad (5)$$

and (x_0, y_0, z_0) is the centre of the Gaussian distribution. The scalar quantities $(\sigma_x, \sigma_y, \sigma_z)$ represent the corresponding size (values given in Table 1). The scalar a represents an amplitude which is equal to 2×10^{-3} for the actuators and one for the sensors. Most of our simulation is performed for the setup reported in Table 1. We denote the i th element of the disturbance vector B_1 by $B_{1,i}$ corresponding to the signal $w_i(t)$.

2.3. Model Reduction

We construct a reduced-order model of the system by projecting the n -dimensional state onto a low-dimensional subspace of dimension r . Expanding the state in a linear combination of columns of the expansion basis $\Phi = (\phi_1, \phi_2, \dots, \phi_r) \in \mathbb{R}^{n \times r}$ as

$$u = \Phi \hat{u} \quad (6a)$$

$$\hat{u} = \Psi^T u, \quad (6b)$$

where $\Psi = (\psi_1, \psi_2, \dots, \psi_r) \in \mathbb{R}^{n \times r}$ are the adjoint modes, bi-orthogonal to the expansion basis Φ , i.e. $\Psi^T \Phi = I$. Substituting Eq. (6a) into the system Eq.

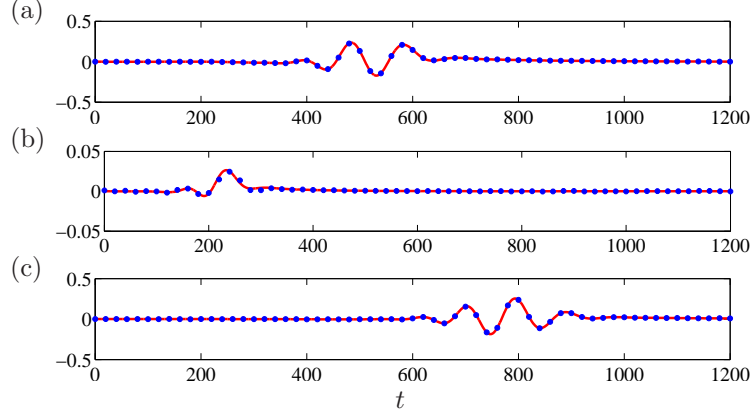


FIGURE 2. Impulse response of the system (a) from the input $B_{2,8}$ to the output $C_{1,8}$, (b) from the input $B_{1,8}$ to the output $C_{2,8}$ and (c) from the input $B_{1,8}$ to the output $C_{1,8}$. The red line shows the DNS results, while the dotted lines indicates the impulse response of the reduced model (Case N Table 2)

(2) and using the bi-orthogonality of the basis, the reduced system of order r is obtained as

$$A_r = \Psi^T A \Phi, \tag{7a}$$

$$B_{1r} = \Psi^T B_1, \quad B_{2r} = \Psi^T B_2, \tag{7b}$$

$$C_{1r} = C_1 \Phi, \quad C_{2r} = C_2 \Phi. \tag{7c}$$

The choice of the basis function is crucial for the performance of the reduced order system (Bagheri *et al.* 2009c; Barbagallo *et al.* 2009). We use a balanced-mode-basis (Moore 1981; Willcox & Peraire 2002; Rowley 2005) that preserves the dynamics between the inputs and outputs of the system. The states that are equally observable and controllable form a hierarchy of so-called balanced modes. The method is based on the concepts of observability and controllability (Zhou *et al.* 2002), which provide a means to characterize the states in terms of how easily triggered they are by the inputs and observed by the outputs, respectively. The states which are neither controllable nor observable or the ones that are weakly controllable or observable are redundant for the input-output behaviour of the system. A limitation pertaining to this method is the necessity of computing the adjoint balanced modes. The Eigensystem Realisation Algorithm (ERA) (Juang & Pappa 1985; Ma *et al.* 2011) is a system identification technique that allows to circumvent this limitation. It is only based on sampling measurements extracted directly from the flow, see a detailed description of the method in Ma *et al.* (2011).

As an example of the performance of the reduced-order model with $r = 435$, in Figure 2 we show the impulse responses:

$$\phi_8 \rightarrow z_8, \quad w_8 \rightarrow v_8, \quad w_8 \rightarrow z_8.$$

In the figure, the solid lines are the impulse response of the full system obtained from solving Navier-Stokes equation while the dotted lines presents the results of the reduced-order model. We observe an equally good agreement for all the inputs and output, when comparing the full system and the ROM. Now that an efficient ROM is constructed, may design a linear controller.

2.4. Control Design

We use a classical LQG-approach to determine a controller that minimises the energy of disturbances captured by output C_1 (Lewis & Syrmos 1995; Zhou *et al.* 2002). The control signal $\phi(t)$ is designed for the actuator B_2 such that the mean of the output energy, $z(t)$, is minimised (see Eq. 3). The LQG design procedure involves a two-step process: first the full state - represented in this case by the velocity field - is reconstructed from the noisy measurement $v(t)$ via an estimator. Once the estimated state \hat{u} is computed the control signal can be computed by the following linear relationship

$$\phi(t) = K\hat{u}(t), \tag{8}$$

where $K \in \mathbb{R}^{m \times r}$ is referred to as the control gain. When the disturbances are modelled as white Gaussian noise, the separation principle allows the two steps (estimation and full-information control) to be performed independently. Furthermore, both problems are optimal and stable and the resulting closed loop is also optimal and stable (Zhou *et al.* 2002). The final form of the reduced order controller (also called compensator) of size r is

$$\dot{\hat{u}}(t) = (A_r + B_{2r}K + LC_{2r})\hat{u}(t) - Lv(t), \tag{9a}$$

$$\phi(t) = K\hat{u}(t), \tag{9b}$$

where the term $L \in \mathbb{R}^{r \times p}$ is the estimator gain and can be computed by solving a Riccati equation (Glad & Ljung 2000), such that the error $\epsilon = \|\hat{u} - u\|^2$ is minimised. The controller is thus a state-space system with the measurements $v(t)$ as input and the control signal $\phi(t)$ as output. The evolution of the perturbations is simulated by marching in time the full DNS, while the controller runs on-line, simultaneously. Eq. 9a is based on the reduced-order model and is solved by using a standard Crank-Nicholson scheme.

2.5. Centralised and Decentralised Controllers

A multivariable control approach is necessary since our system has more than one actuator and sensor. The degree of control complexity in a multivariable approach depends on the degree of coupling between inputs and outputs. For example consider the transfer function between the input w_j to the output v_k . Then the effect on v_k due to a small change in w_j may depend on one, a few or all other inputs w_h for $h \neq j$, if the system is uncoupled, weakly coupled or

fully coupled, respectively. The degree of coupling depends usually not only on the actuator/sensor placement but also on the dynamics of the TS wavepackets. As we shall see, we have a situation of a weakly coupled system, due to the fact that a TS wavepacket generated from a point source spreads only in a limited spanwise region.

The most straight-forward approach is the so called centralised controller where all the inputs and outputs are connected together. The main disadvantage is that the number of interconnections – thus the complexity of the controller – increase significantly as we aim to control perturbations over a larger span of the domain. In contrast, a fully decentralised controller connects only one sensor to one actuator, and thus requires by definition the same number of actuators and sensors. This approach disregards any influence of an input which is not placed directly upstream the output; this is a risky model assumption, as the influence that may exist in reality will induce an over- or underestimation of the signals, causing instabilities. A compromise between the centralised and fully decentralised approach is a semi-decentralised approach (henceforth only referred to as decentralised), where the system is divided into a collection of independent sub-systems. For each sub-system a controller is designed – called a control unit – for a few number of sensors and actuators. Then, the same controller is replicated along the span to cover a broader region. As we will see the division into control units provides an efficient means for control of TS waves, since the disturbance source upstream is only observable at a subset of sensors; thus some of the interconnections which are not relevant to the dynamics of the system are neglected (see Figure 1).

The number of interconnections in a control system determines the complexity of a controller. Reducing the complexity has a number of advantages including, easier implementation (less hardware) low-dimensionality of the system (faster system). In a system with a centralised controller using n sensors and n actuators, n^2 interconnections are required. However if we split this system into $\sim n/m$ control units with m sensors and m actuators each, the total number of interconnections becomes $n/m \times m^2 = nm$. This is a linear function of n instead of a quadratic function. The net gain of a decentralised controller is more evident when the number of sensors and actuators increases in the system *e.g.* when the objective is to control a larger span of the boundary layer.

3. Results

In the following sections, we first design and analyse a centralised controller for the attenuation of small-amplitude TS wavepackets. After a parametric study of the control penalty, we identify a reference controller, as the centralised controller that for the chosen flow parameters (Re , domain, etc) provides the best performance. Second, we design a set of decentralised controllers by assembling several control units of different sizes. Their control efficiency in terms of performance (robustness is left for future studies) will be compared to the

Case	Description	Control Penalty		Order	Norm Reduction	Energy Reduction
k	—	l	r		$1 - \frac{\ G_k\ _2^2}{\ G_n\ _2^2}$	\bar{E}_k
N	18/18 – 18 – 18 – 18/1	—	—	—	0%	0.00
A	18/18 – 18 – 18 – 18/1	100	—	435	45%	0.27
B	18/18 – 18 – 18 – 18/1	10	—	435	98%	0.80
C	18/18 – 18 – 18 – 18/1	1	—	435	98%	0.80

TABLE 2. The performance of a LQG controller designed with different control penalties. The noise autocovariance on the estimation sensors and for all cases are assumed constant $\alpha^2 = 10^{-6}$. The norms are computed in the time interval $t \in [2000, 8000]$. The description identifier is defined as the following; number of disturbances B_1 / the design configuration of the system consists of $d - p - m - k$ disturbances-estimation sensors-actuators-outputs/ number of control units.

reference controller. In order to determine the performance of the controller, we use the 2-norm of a system G . When the inputs of the system are white noises with variance σ_w^2 , $\|G\|_2^2$ can be computed as:

$$\|G\|_2^2 = \frac{1}{d\sigma_w^2} \sum_i \frac{1}{T} \int_{t_0}^{t_1} (C_{1i}u)^2 dt \quad (10)$$

where $T = t_1 - t_0$ is the period over which the performance is evaluated. In Table 2-4, we compare the norm of the uncontrolled system $\|G_n\|_2^2$ to the ones with control $\|G_k\|_2^2$.

3.1. Centralised Controller

In Table 2 the effect of different control penalties (parameter l in Eq. 3) on the performance of the closed-loop system is investigated for a centralized LQG controller and the setup in Table 1. The optimal value of the control penalty is usually not known before applying the controller to the full DNS and involves an iterative procedure. In general, small values of the control penalty correspond to a reduction of the perturbation amplitude; however, too low values of control penalties may result in unfavourable behaviour such as unphysical control signal (Semeraro *et al.* 2011). Case *C* in Table 2 is selected as the baseline reference controller, for which all decentralized controller will be compared to, while case *N* represents the system without implementing the control (uncontrolled case) and is used to compute the performance of the controller.

First, we characterize the performance of controller *C* using a number of different observables. Figure 3 represents the input-output behaviour of the closed-loop system for case *C*. In this setup, there are totally 18 inputs B_1 ;

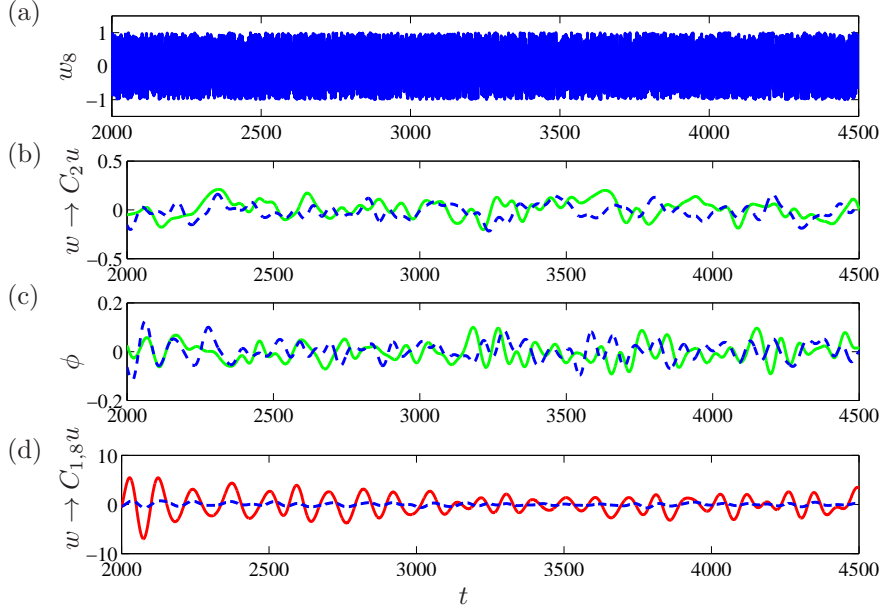


FIGURE 3. Noise response of the closed-loop system: Stochastic excitation of the input $B_{1,8}$ is shown in (a), estimation signals $C_{2,8}$ (dashed blue line) and $C_{2,18}$ (solid green line) in (b), control signal feeding the actuator $B_{2,8}$ (dashed blue lines) and $B_{2,18}$ (solid green line) in (c) and measurement extracted by sensor $C_{1,8}$ for uncontrolled (solid line) and controlled and dashed (dashed line) system (cases N and C in Table 2) in (d).

each of them are excited by an independent white noise of variance $\frac{1}{3}$. In the first frame (Figure 3a), the disturbance input w_8 is shown. It is a white noise signal that provides a continuous forcing at $B_{1,8}$. Figure 3b shows the measurement detected by upstream sensors $C_{2,8}$ and $C_{2,18}$. The sensors are located close to the wall, inside of the boundary layer and can register the evolution of the disturbance. One clearly observes that certain frequencies are amplified by the system, whereas others are damped. Figure 3c reports the control signals related to actuators $B_{2,8}$ and $B_{2,18}$. Since the disturbances are uncorrelated, we can observe independent behaviour for different actuators. Finally, in Figure 3d, the signal extracted from output $C_{1,8}$ for the uncontrolled and controlled cases is shown. The root mean square (r.m.s) of the signal is reduced up to 89%.

The input-output behaviour of the closed-loop system in frequency domain is shown in Figure 4. The power spectrum density of the input signal w_8 together with the output signal $C_{1,8}u$ in the controlled and uncontrolled configuration are plotted (cases N and C). In this configuration the most amplified

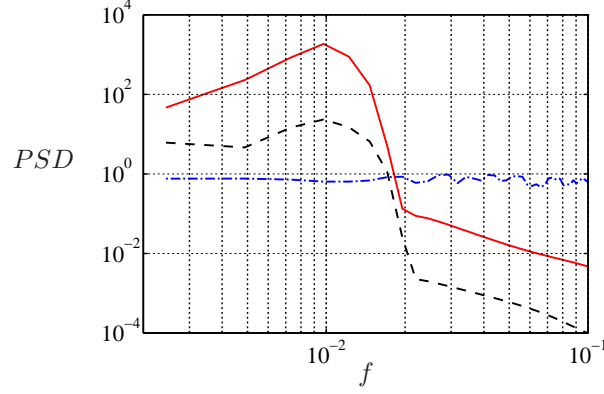


FIGURE 4. Power spectrum density (PSD) of the input signal w_8 (dashed-dots blue – cases $N - C$), uncontrolled output signal $C_{1,8}u$ (solid red – case N) and the controlled output signal $C_{1,8}u$ (dashed black – case C) are shown.

frequency in the system is 0.00171, where its energy is damped up to one order of magnitude.

In a three-dimensional configuration, the minimisation of the sensor measurements near the wall, does not guarantee the reduction of the perturbation energy in the full domain. This has to be evaluated a posteriori. Figure 5 shows the energy, $E(t) = u^T u / 2$, of the perturbation as a function of time. The mean value of the energy reduction \bar{E}_k is defined as

$$\bar{E}_k = \frac{\int_{t_0}^{t_1} E_N dt - \int_{t_0}^{t_1} E_k dt}{\int_{t_0}^{t_1} E_N dt}, \quad (11)$$

where $[t_0, t_1]$ is the time interval in which the statistics are computed. In Figure 5, the uncontrolled energy E_N is shown by a solid red line while the controlled energy, E_k is shown with a blue line. We observed that the energy is reduced by approximately 80%.

Finally, in order to gain an insight into where in the physical domain, the controller has a strong effect, we show in Figure 6 the distribution of the r.m.s value of the streamwise velocity of disturbances in horizontal plane (streamwise-spanwise) averaged along wall normal direction. The disturbances B_1 are located at $x = 60$ from the beginning of the computational box. We expect the amplitude of the perturbations to grow as we move toward the end of the domain in uncontrolled case N (Figure 6a). Figure 6b shows the resulting r.m.s value of the perturbations when the controller is active. The suppression of the perturbations begin from $x = 167$ where the actuators are located. Figure 6c reports the percentage of the reduction in r.m.s of the perturbation. Since the

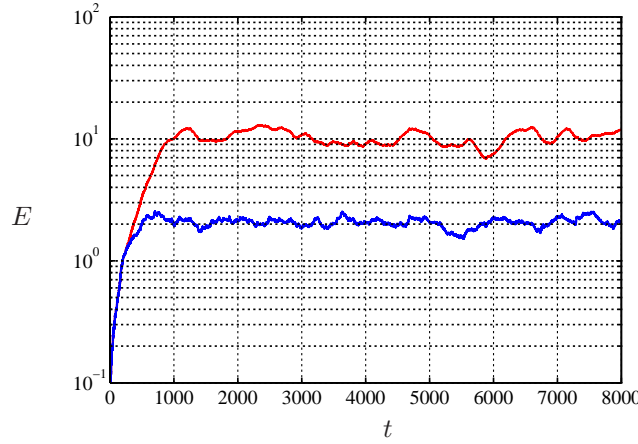


FIGURE 5. Energy of the perturbations E as a function of time t ; solid red line corresponds to the energy of uncontrolled case E_N and solid blue line to the controlled case E_C . The statistics are computed for the time interval $t \in [3000 \ 8000]$.

objective function of the controller is to attenuate the amplitude of the perturbation where the outputs are located, a significant reduction is observed at that region; the reduction is also homogeneous in spanwise direction.

3.2. Decentralised Controllers

Having shown that centralized controller with a very high complexity may reduce energy by nearly an order of magnitude, we now investigate how decentralized controllers of lower complexity compare in performance. As already mentioned, the decentralized controllers are designed in two steps; (i) constructing a control unit using only a few actuators and sensors; (ii) by replicating the units in the spanwise direction.

3.2.1. Design and Performance of Single Control Units

The simplest control unit is obtained by connecting one sensor C_2 to one actuator B_2 . Despite the relative simplicity of this configuration both in terms of the design and implementation, the results are prone to the stability problems and poor control performance (Li & Gaster 2006; Semeraro *et al.* 2011).

Motivated by the experimental work of Li & Gaster (2006), we choose to investigate two control units:

1. The first one consists of three actuators (the center actuator $B_{2,8}$ and two adjacent to the center $B_{2,7}$ and $B_{2,9}$), three estimation sensors ($C_{2,7}$, $C_{2,8}$ and $C_{2,9}$) and 9 objective sensors $C_{1,(4,5,\dots,12)}$. During the design process of the control unit, we assume that there exists 5 upstream disturbances $B_{1,(6,7,\dots,10)}$, but the actual performance of the controller is

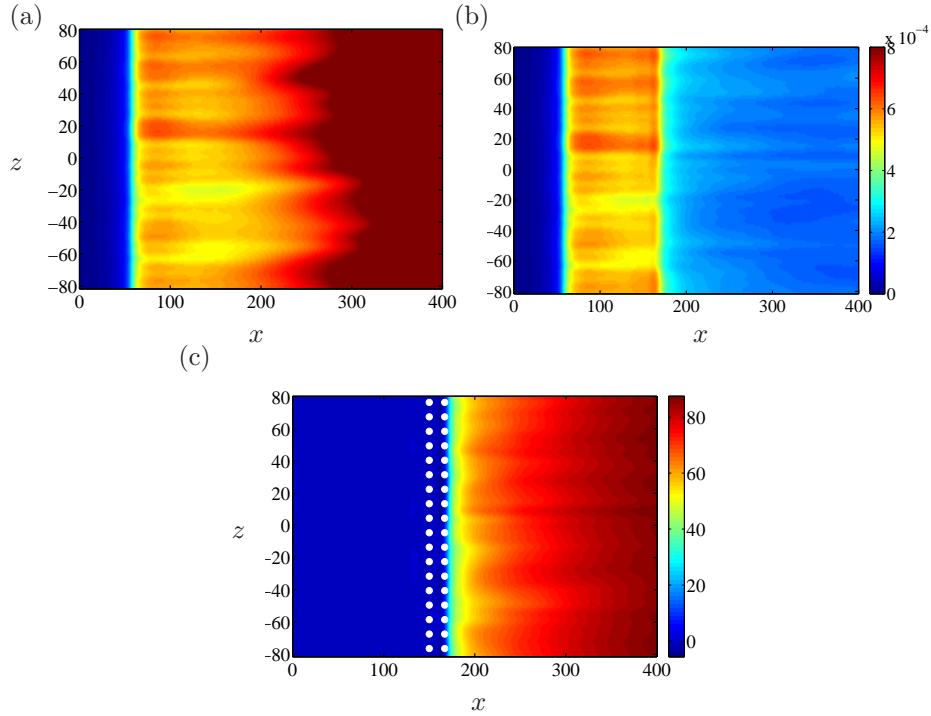


FIGURE 6. Streamwise root mean square velocity averaged along wall normal direction for the uncontrolled case N (a) and controlled case C (b) and the corresponding percentage of the reduction (c). The statistics are computed for the time interval $t \in [3000, 8000]$. The white dots indicate the location of estimation sensors C_2 and the actuators B_2 .

Case	Description	Control penalty	Order	Norm Reduction	Energy Reduction
k	—	l	r	$1 - \frac{\ G_k\ _2^2}{\ G_N\ _2^2}$	\bar{E}_k
D	18/5 – 3 – 3 – 9/1	20	155	4.6%	0.109
E	18/5 – 1 – 3 – 9/1	20	155	2.2%	0.044
F	18/3 – 3 – 3 – 9/1	20	119	3.4%	0.087
G	18/5 – 3 – 3 – 3/1	10	87	8.4%	0.083

TABLE 3. In each case only one control unit is employed. The noise autocovariance for all the cases are assumed as $\alpha^2 = 10^{-6}$ and the norms are computed for time $t > 2000$.

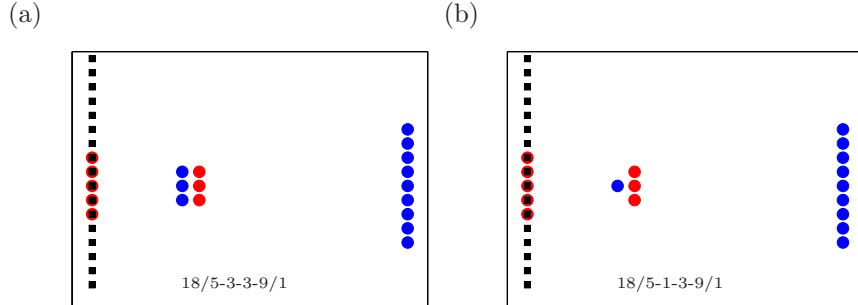


FIGURE 7. A schematic view of two control units. The controller shown in (a) is designed considering 5 upstream disturbances $B_{1,(6,7,\dots,10)}$, 3 estimation sensors $C_{2,(7,8,9)}$, 3 actuators $B_{2,(7,8,9)}$ and 9 outputs $C_{1,(4,5,\dots,12)}$ as the objective function (circles). This control unit performs when 18 disturbances are evolving into the domain (squares). The layout and the number of sensors and actuators remain the same for the control unit depicted (b), but only one estimation sensor $C_{2,8}$ is used.

assessed when 18 disturbance sources are active (see sketch in Figure 7a). The description identifier of this control unit is $(18/5-3-3-9/1)$, where the different numbers are respectively; number of disturbances B1 / the design configuration of the system consists of $d - p - m - k$ (disturbances-estimation sensors-actuators-outputs) / number of control units.

2. The second one $(18/5-1-3-9/1)$ has only one estimation sensor, namely the center one ($C_{2,8}$) as shown in Figure 7b. The remaining parameters are the same the first control unit.

Figure 8 shows the control signal for the two lateral actuators $B_{2,7}$ and $B_{2,9}$ for both control unit one and two. It is obvious that the two actuators behave in the same manner for the second controller (case E in Table 3) while they are acting independently for the multiple sensor control unit (case D in Table 3). After designing the control units, their performances are monitored while 18 disturbances B_1 evolve and convect downstream $(18/5-3-3-9/1)$. Figure 8 depicts the control signal for the two lateral actuators $B_{2,7}$ and $B_{2,9}$ for both cases. It is obvious that the two actuators behave in the same manner for the symmetric controller (case E) while they are acting independently for the asymmetric one (case D).

Figure 9 shows the streamwise velocity cancellation at two different planes $z = -13.5$ and $y = 0.6$ for case D . The maximum rms reduction in this case is 48%. The same number of sensor and actuators (1 sensor - 3 actuators) are used in the experimental setup by Li & Gaster (2006). The maximum rms reduction in this case is similar to the one obtained in the experiment. In the

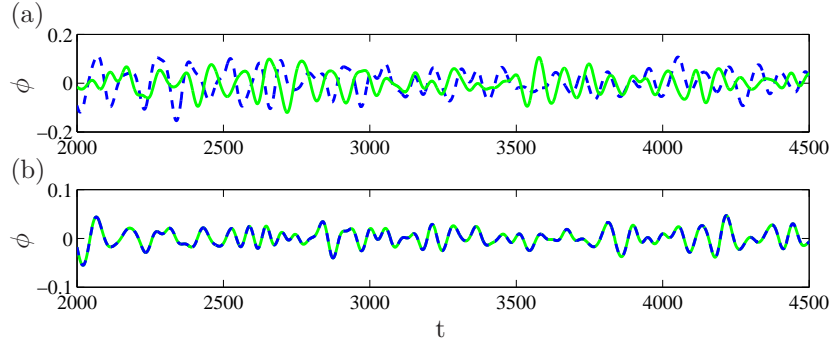


FIGURE 8. Control signal driving the actuators $B_{2,7}$ (solid line) and $B_{2,9}$ (dotted line) are shown in (a) for a three-estimation sensors-based control unit (case D in Table 3) and in (b) for single-estimation sensors-control unit (case E in Table 3).

experimental setup the data is extracted at a lower plane $y = 0.36$ but the maximum reduction in case D occurs at $y \approx 0.6$. The difference between the two cases may arise from the fact that the effect of the actuators are different in both cases. Moreover, in this case we use 18 sources of disturbance with a periodic boundary condition which numerically analogues to using an infinite number of actuators while in the experimental setup, they only used 15 sources of disturbance. Figure 10 shows the streamwise velocity cancellation averaged along wall normal direction. The white dots indicate the spatial configuration of the sensors and actuators for the two cases D and E . The Figs. 10a and 10b confirm that a level of cancellation up to 40% is achieved in the central area downstream of the actuators while it faded away as we move downstream. Controller based on only one upstream sensor can act on a limited region while the controller based on three sensors is able to influence a broader domain. The reason is that the latter controller can identify the discrepancy between the disturbances coming from lateral sides, i.e. the observability of the system is significantly larger. This controller can attenuate the energy of the system up to 10.9% (see Table 3 case D), while the single-sensor controller can only suppress the energy up to 4.4%. Furthermore, in terms of norms of the system, the corresponding reduction between the two controllers are 4.6% and 2.2%. In the following section we use the control unit, case F .

3.2.2. Effect of Crosstalk

As a localised disturbance propagates downstream, it will – after a short transient – develop into a wavepacket that grows in size and spreads along the spanwise direction. Each estimation sensor $C_{2,j}$ does not only receive a signal from the disturbance source directly upstream of it (w_j), but also the lateral

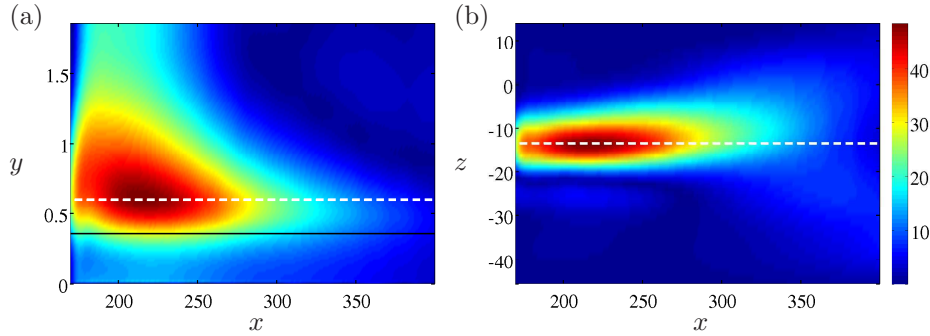


FIGURE 9. Percentage reduction in streamwise velocity cancellation (case E) at a) plane $z = -13.5$ and b) plane $y = 0.6$. White lines at $y = 0.6$ and $z = -13.5$ resemble the cross section of the two planes and solid black line at $y = 0.36$ is used by (Li & Gaster 2006) to extract the results.

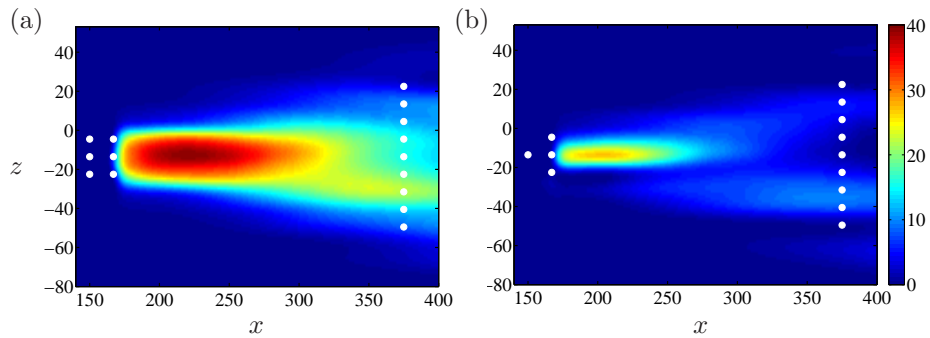


FIGURE 10. Percentage reduction in streamwise velocity cancellation averaged along wall normal direction for case D (a) and E (b) is shown. The white dots indicate the location of sensors C_1 , C_2 and actuators B_2 .

sources (w_h , for $h \neq j$) contribute to the total measured signal. The additional perturbations, originated from the lateral sources and detected by the estimation sensors C_2 , are referred to as *crossstalk* (see Figure 12).

Consider now the control unit, Case F , from the previous section (3 estimation sensors and 3 actuators). The energy of the signals received by 3 estimation sensors from different numbers of disturbance sources B_1 is shown in Figure 11a. As one can observe, around 70% of the total energy of the signals originate from 3 disturbance sources directly upstream of the estimation sensors. In order to capture 90% of the total energy of the signals, 5 disturbance sources are required in which, the additional 20% of the energy belongs to the two lateral disturbance sources.

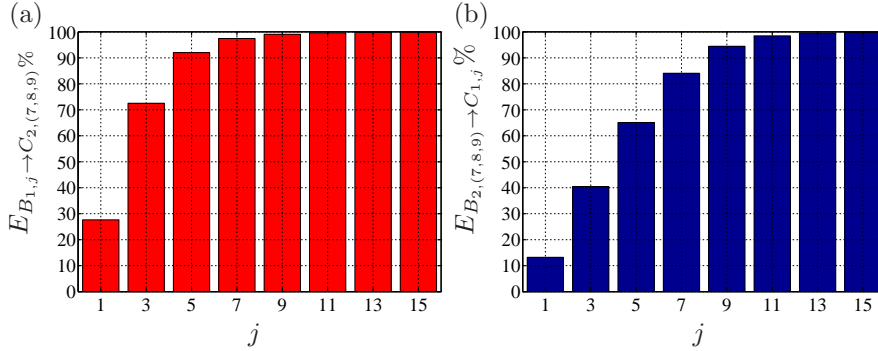


FIGURE 11. Energy captured by 3 estimation sensors $C_{2,(7,8,9)}$ originates from impulse response of different number of disturbances (a) and energy harvested by using different number of outputs C_1 from the impulse response of 3 actuator $B_{2,(7,8,9)}$ (b). The data is normalised by the maximum value when $j = 18$. The number of disturbances or outputs (elements) denotes as j . $j = 1$ corresponds to an element located at $z = -13.5$ ($i=7$). $j = 3$ corresponds to 3 elements $i \in (6, 7, 8)$. The numbering convention continues the same with the central element located at $i = 7$; for instance, $j = 5$ corresponds to 5 elements $i \in (5, 6, 7, 8, 9)$ and so on.

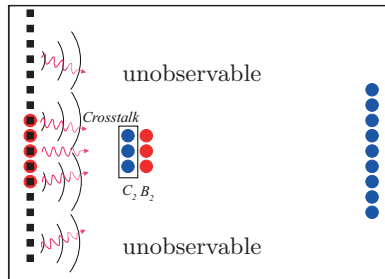


FIGURE 12. A schematic layout of the control unit. Two kind of perturbations, observed by 3 sensors $C_{2,(7,8,9)}$ are depicted; they include the perturbation coming from sources directly in front of the sensors and the lateral perturbations coming from sides which is referred to as *crosstalk*.

To investigate the effect of the crosstalk in the performance of the control unit, we compare two cases. The only difference between them is the number of disturbance sources B_1 considered in the design process. Just as before we consider 5 disturbance sources B_1 in case with crosstalk (case D) while we

reduce the effect of crosstalk and only design the controller for 3 disturbance sources B_1 ($18/3 - 3 - 3 - 9/1$ or case F in Table 3). Table 3 shows the performance of the two systems; the configuration that takes into account 90% of the total energy can attenuate the energy of the disturbances up to 10.9% while the configuration taking into account only 70% of the total energy can reduce the energy up to 8.7%. This indicates the number of disturbance sources in the control design process depends on the nature of the disturbance (e.g. how fast it spreads in the spanwise direction). Capturing only part of the spreading of a disturbance has a sizable effect on the control performance.

Next, we investigate the performance of the controllers when the control units are replicated along the spanwise direction. First, we consider 6 control units based on the configurations with high level crosstalk and with reduced-level of crosstalk. Table 4 reports the reduction in the energy of the system using these controllers. The performance of 6 control units considering the crosstalk effect (case H) is only 11% less than the centralised controller (case C in Table 2) where all the interconnections between the sensors and the actuators are taken into account. On the other hand, if we only capture part of the crosstalk effect (case J) we loose an additional 9% of performance.

3.2.3. Capturing the spread of the disturbances

Since the wavepackets spread along the spanwise direction while propagating downstream, we need to distribute a minimum number of objective sensors $C_{1,j}$ along the span to correctly capture the energy of the disturbances. On the other hand, we have to be able to control the disturbances detected by outputs C_1 using the actuators B_2 . In fact, the further away the outputs are from the centreline of an actuator, the less we can control the structures detected by that outputs. More specifically, we consider again control units which have 3 actuators ($B_{2,(7,8,9)}$). Figure 11b reports the energy of the signals captured by different number of outputs C_1 , which originate from the impulse responses of the 3 actuators. We can observe that over 90% of the total energy that originated from an impulse in the 3 actuators is captured by 9 outputs. According to this observation, we compare two controllers, whose differentiate only in the number of employed outputs in the control design. In the first configuration (case D in Table 3) we consider 9 outputs ($C_{1,i}, i = 4, \dots, 12$) while in the second configuration (case G in Table 3) we implement 3 outputs only ($C_{1,i}, i = 7, 8, 9$). As one can observe in Table 3, the reduction in the energy of the system \bar{E}_k in the case with 9 outputs is 10.9% while in the case with 3 outputs is 8.3%.

It is important to note that in both configurations, we take into account the crosstalk effect. If we compare the performance of the controller with 3 outputs (case G) to the controller that only partially accounts for the crosstalk from the previous study in sec 3.2.2 (case F), we can observe that the energy reduction in the second case is larger, 8.3% vs 8.7%. Finally, we compare on the performance of the 6 control units with 9 and 3 outputs in Table 4 (cases H

Case	Description	Norm Reduction	Energy Reduction
k	—	$1 - \frac{\ G_k\ _2^2}{\ G_n\ _2^2}$	\bar{E}_k
H	18/5 – 3 – 3 – 9/6	88.0%	0.69
J	18/3 – 3 – 3 – 9/6	85.5%	0.60
K	18/5 – 3 – 3 – 3/6	64.7%	0.48

TABLE 4. In each case 6 control unit are used. The control units distributed equidistantly along the span and does not have any overlap. The noise autocovariance for all the cases are assumed as $\alpha^2 = 10^{-6}$. In addition, the norms are computed for time $t > 2000$.

and K). In the former, the energy is attenuated up to 69% while in the latter, it is reduced up to 48%.

4. Conclusion

We have investigated and compared two different control strategies, namely a centralised and a decentralised. In the former approach where all the sensors and actuators are connected together, the complexity of the system (due to the number of interconnections) may be too high for implementation in experiments, in particular, as we aim to control over a wider span of the domain. We have presented an alternative decentralised strategy, where several small control units consisting of 3 pairs of actuators-sensors are assembled to cover the full spanwise length of the flat plate. The choice 3 actuators-sensors as well as the number of source disturbances and objective sensors included in the design of a single control unit needs to be chosen with a physical insight on the spatial and temporal scales of the perturbation inside the boundary layer. We have focused on TS wavepackets, streaky structures observed under different conditions inside the boundary layer, may need control units of different order.

As explained in Sec.3.2.3 our results reveal that the best performance is obtained for a control unit which (i) has “sufficient” number of output measurements and (ii) is designed to account for the perturbations which are coming from the lateral sides (crosstalk) of the estimation sensors. We may also conclude that the influence of crosstalk is not as essential as the spreading effect.

Acknowledgements

The authors wish to thank Ardeshir Hanifi and Onofrio Semeraro for fruitful discussions. Computer time was provided by the Center for Parallel Computers (PDC) at the Royal Institute of Technology (KTH) and the National Supercomputer Center (NSC) at Linköping University in Sweden.

References

- BAGHERI, S., AKERVIK, E., BRANDT, L. & HENNINGSON, D. S. 2009a Matrix-Free Methods for the Stability and Control of Boundary Layers. *AIAA J.* **47**, 1057–1068.
- BAGHERI, S., BRANDT, L. & HENNINGSON, D. S. 2009b Input–output analysis, model reduction and control of the flat-plate boundary layer. *J. Fluid Mech.* **620** (1), 263–298.
- BAGHERI, S. & HENNINGSON, D. S. 2011 Transition delay using control theory. *Philos. Trans. R. Soc.* **369**, 1365–1381.
- BAGHERI, S., HEPFFNER, J., SCHMID, P. J. & HENNINGSON, D. S. 2009c Input–Output Analysis and Control Design Applied to a Linear Model of Spatially Developing Flows. *Appl. Mech. Rev.* **62**.
- BARBAGALLO, A., SIPP, D. & SCHMID, P. J. 2009 Closed-loop control of an open cavity flow using reduced order models. *J. Fluid Mech.* **641**, 1–50.
- BEWLEY, T. R. 2001 Flow Control: New Challenges for a New Renaissance. *Progr. Aerospace Sci.* **37**, 21–58.
- CHEVALIER, M., SCHLATTER, P., LUNDBLADH, A. & HENNINGSON, D. S. 2007 A pseudo-spectral solver for incompressible boundary layer flows. *Tech. Rep. TRITA-MEK 2007:07*. KTH Mechanics, Stockholm, Sweden.
- CORTELEZZI, L., SPEYER, J. L., LEE, K. H. & KIM, J. 1998 Robust Reduced-Order Control of Turbulent Channel Flows via Distributed Sensors and Actuators. *IEEE 37th Conf. on Decision and Control* pp. 1906–1911.
- DADFAR, R., SEMERARO, O., HANIFI, A. & HENNINGSON, D. S. 2013 Output feedback control of blasius flow with leading edge using plasma actuator. *AIAA J.* **51** (9), 2192–2207.
- DOYLE, J. C., GLOVER, K., KHARGONEKAR, P. P. & FRANCIS, B. A. 1989 State-Space Solutions to Standard H_2 and H_∞ Control Problems. *IEEE Trans. Autom. Control* **34**, 831–847.
- GLAD, T. & LJUNG, L. 2000 *Control Theory*. London: Taylor & Francis.
- HAMMOND, E. P., BEWLEY, T. R. & MOIN, P. 1998 Observed Mechanisms for Turbulence Attenuation and Enhancement in Opposition-Controlled Wall-Bounded Flows. *Phys. Fluids* **10** (9), 2421–2423.
- HÖGBERG, M., BEWLEY, T. R. & HENNINGSON, D. S. 2003 Relaminarization of $Re_\tau = 100$ Turbulence Using Gain Scheduling and Linear State-feedback Control Flow. *Phys. Fluids* **15**, 3572–3575.
- JOSHI, S. S., SPEYER, J. L. & KIM, J. 1997 A Systems Theory Approach to the Feedback Stabilization of Infinitesimal and Finite-amplitude Disturbances in Plane Poiseuille Flow. *J. Fluid Mech.* **332**, 157–184.
- JUANG, J.-N. & PAPPA, R. S. 1985 An eigensystem realization algorithm for modal parameter identification and model reduction. *J. Guid., Con. Dyn.* **8** (5), 620–627.
- KIM, J. & BEWLEY, T. R. 2007 A Linear Systems Approach to Flow Control. *Ann. Rev. Fluid Mech.* **39**, 39–383.
- LEWIS, F. L. & SYRMOS, L. V. 1995 *Optimal Control*. John Wiley & Sons, New York.

124 *R. Dadfar, N. Fabbiane, S. Bagheri & D. S. Henningson*

- LI, Y. & GASTER, M. 2006 Active Control of Boundary-Layer Instabilities. *J. Fluid Mech.* **550**, 185–205.
- MA, Z., AHUJA, S. & ROWLEY, C. W. 2011 Reduced-order models for control of fluids using the eigensystem realization algorithm. *Theoretical and Computational Fluid Dynamics* **25** (1-4), 233–247.
- MOORE, B. 1981 Principal Component Analysis in Linear Systems: Controllability, Observability, and Model reduction. *IEEE Trans. Autom. Control* **26** (1), 17–32.
- NORDSTRÖM, J., NORDIN, N. & HENNINGSON, D. 1999 The fringe region technique and the Fourier method used in the direct numerical simulation of spatially evolving viscous flows. *SIAM J. Sci. Comp.* **20** (4), 1365–1393.
- ROWLEY, C. W. 2005 Model reduction for fluids, using balanced proper orthogonal decomposition. *Intl J. of Bifurcation and Chaos* **15** (03), 997–1013.
- SEMERARO, O., BAGHERI, S., BRANDT, L. & HENNINGSON, D. S. 2010 Linear Control of 3D Disturbances on a Flat-Plate. In *7th IUTAM Symposium on Laminar-Turbulent Transition* (ed. P. Schlatter & D. S. Henningson), , vol. 18. Springer.
- SEMERARO, O., BAGHERI, S., BRANDT, L. & HENNINGSON, D. S. 2011 Feedback control of three-dimensional optimal disturbances using reduced-order models. *J. Fluid Mech.* **677**, 63–102.
- SEMERARO, O., BAGHERI, S., BRANDT, L. & HENNINGSON, D. S. 2013 Transition delay in a boundary layer flow using active control. *J. Fluid Mech.* **731** (9), 288–311.
- STURZEBECKER, D. & NITSCHKE, W. 2003 Active cancellation of Tollmien–Schlichting instabilities on a wing using multi-channel sensor actuator systems . *Intl J. Heat and Fluid Flow* **24**, 572–583.
- THOMAS, A. S. W. 1984 Aircraft Drag Reduction Technology. *Tech. Rep.*. Lockheed-Georgia co Marietta Flight Sciences Division.
- WILLCOX, K. & PERAIRE, J. 2002 Balanced model reduction via the proper orthogonal decomposition. *AIAA J.* **40** (11), 2323–2330.
- ZHOU, K., DOYLE, J. C. & GLOVER, K. 2002 *Robust and Optimal Control*. Prentice Hall, New Jersey.